Leg 190 Preliminary Report

Deformation and Fluid Flow Processes in the Nankai Trough Accretionary Prism

Shipboard Scientific Party

Ocean Drilling Program
Texas A&M University
1000 Discovery Drive
College Station TX 77845-9547
USA

August 2000

This report was prepared from shipboard files by scientists who participated in the cruise. The report was assembled under time constraints and does not contain all works and findings that will appear in the *Initial Reports* of the ODP *Proceedings.* Reference to the whole or to part of this report should be made as follows:

Shipboard Scientific Party, 2000. Leg 190 Preliminary Report: Deformation and fluid flow processes in the Nankai Trough accretionary prism. *ODP Prelim. Rpt.,* 190 [Online]. Available from World Wide Web:
<http://www-odp.tamu.edu/publications/prelim/190_prel/190PREL.PDF>. [Cited YYYY-MM-DD]

Distribution

Electronic copies of this series may be obtained from the Ocean Drilling Program's World Wide Web site at http://www-odp.tamu.edu/publications.

DISCLAIMER

This publication was prepared by the Ocean Drilling Program, Texas A&M University, as an account of work performed under the international Ocean Drilling Program, which is managed by Joint Oceanographic Institutions, Inc., under contract with the National Science Foundation. Funding for the program is provided by the following agencies:

Australia/Canada/Chinese Taipei/Korea Consortium for Ocean Drilling
Deutsche Forschungsgemeinschaft (Federal Republic of Germany)
Institut National des Sciences de l'Univers-Centre National de la Recherche Scientifique (France)
Ocean Research Institute of the University of Tokyo (Japan)
National Science Foundation (United States)
Natural Environment Research Council (United Kingdom)
European Science Foundation Consortium for the Ocean Drilling Program (Belgium, Denmark, Finland, Iceland, Ireland, Italy, The Netherlands, Norway, Spain, Sweden, and Switzerland)
Marine High-Technology Bureau of the State Science and Technology Commission of the People's Republic of China

The following scientists were aboard *JOIDES Resolution* for Leg 190 of the Ocean Drilling Program:

Gregory F. Moore
Co-Chief
Department of Geology and Geophysics/SOEST
University of Hawaii at Manoa
1680 East-West Road, POST 813
Honolulu HI 96822
USA
Phone: (808) 956-6854
Fax: (808) 956-5154
Internet: gmoore@Hawaii.edu

Asahiko Taira
Co-Chief
Ocean Research Institute
University of Tokyo
1-15-1, Minamidai, Nakano-ku
Tokyo 164-8639
Japan
Phone: (81) 3-5351-6437
Fax: (81) 3-5351-6527
Internet: ataira@ori.u-tokyo.ac.jp

Adam Klaus
Staff Scientist
Ocean Drilling Program
Texas A&M University
1000 Discovery Drive
College Station TX 77845-9547
USA
Phone: (979) 845-3055
Fax: (979) 845-0876
Internet: aklaus@odpemail.tamu.edu

Keir Becker
Downhole Tools Specialist
Rosenstiel School of Marine and Atmospheric Science
University of Miami
Division of Marine Geology and Geophysics
4600 Rickenbacker Causeway
Miami FL 33149-1098
USA
Phone: (305) 361-4661
Fax: (305) 361-4632
Internet: kbecker@rsmas.miami.edu

Luann Becker
Organic Geochemist
Hawaii Institute of Geophysics and Planetology
University of Hawaii at Manoa
1680 East-West Road
Honolulu HI 96822
USA
Phone: (808) 956-5010
Fax: (808) 956-3188
Internet: lbecker@soest.hawaii.edu

Babette Boeckel
Paleontologist (nannofossils)
FB 5 Geowissenschaften
Universitaet Bremen
Klagenfurterstrasse
Postfach 330440
28334 Bremen
Federal Republic of Germany
Phone: (49) 421-218-9591
Fax: (49) 421-218-7431
Internet: bboeckel@uni-bremen.de

Barry A. Cragg
Microbiologist
Department of Earth Sciences
University of Bristol
Wills Memorial Building
Queens Road
Bristol BS8 1RJ
United Kingdom
Phone: (44) 117-954-5442
Fax: (44) 117-925-3385
Internet: b.cragg@bristol.ac.uk

P. Allison Dean
Paleomagnetist
Department of Geology
Western Washington University
526 High Street
Bellingham WA 98225
USA
Phone: (360) 650-3582
Fax: (360) 650-7302
Internet: allison@ancientseas.com

Christopher L. Fergusson
Sedimentologist
School of Geosciences
University of Wollongong
Wollongong, NSW 2522
Australia
Phone: (61) 2-4221-3860
Fax: (61) 2-4221-4250
Internet: chris_fergusson@uow.edu.au

Pierre Henry
Physical Properties Specialist
Département de Géologie
École Normale Supérieure
24 rue Lhomond
75231 Paris Cedex 05
France
Phone: (33) 1-44-32-22-53
Fax: (33) 1-44-32-20-00
Internet: henry@geologie.ens.fr

Satoshi Hirano
Sedimentologist
Frontier Research Program for Subduction Dynamics
Japan Marine Science and Technology Center
2-15 Natsushimacho
Yokosuka, Kanagawa 237-0061
Japan
Phone: (81) 468-67-3396
Fax: (81) 468-67-3409
Internet: hiranos@jamstec.go.jp

Toshio Hisamitsu
Paleomagnetist
Ocean Research Institute
University of Tokyo
1-15-1, Minamidai, Nakano-ku
Tokyo 164-8639
Japan
Phone: (81) 3-5351-6434
Fax: (81) 3-5351-6527
Internet: hisa@ori.u-tokyo.ac.jp

Sabine Hunze
Physical Properties Specialist
Geowissenschaftliche Gemeinschaftsaufgaben -GGA
Stilleweg 2
30631 Hannover
Federal Republic of Germany
Phone: (49) 511-643-3494
Fax: (49) 511-643-3665
Internet: s.hunze@gga-hannover.de

Miriam Kastner
Inorganic Geochemist
Scripps Institution of Oceanography
University of California, San Diego
Geoscience Research Division
9500 Gilman Drive
La Jolla CA 92093-0212
USA
Phone: (858) 534-2065
Fax: (858) 534-0784
Internet: mkastner@ucsd.edu

Alex J. Maltman
Structural Geologist
Institute of Geography and Earth Sciences
University of Wales, Aberystwyth
Aberystwyth SY23 3DB
United Kingdom
Phone: (44) 1970-622655
Fax: (44) 1970-622659
Internet: ajm@aber.ac.uk

Julia K. Morgan
Structural Geologist
Department of Geology and Geophysics
MS-126
Rice University
6100 S Main Street
Houston TX 77005-1892
USA
Phone: (713) 348-6330
Fax: (713) 348-5214
Internet: morganj@rice.edu

Yuki Murakami
Microbiologist
Graduate School of Biosphere Sciences
Hiroshima University
1-4-4 Kagamiyama
Higashi-Hiroshima 739-8528
Japan
Phone: 81-824-24-7986
Fax: 81-824-22-7059
Internet: yukinm@hiroshima-u.ac.jp

Demian M. Saffer
Physical Properties Specialist
Earth Sciences Department
University of California
1156 High Street
Santa Cruz CA 95064
USA
Phone: (831) 459-2762
Fax: (831) 459-3074
Internet: dsaffer@es.ucsc.edu

Mario Sánchez-Gómez
Structural Geologist
Departamento de Geología
Universidad de Jaén
Virgen de la Cabeza, 2
23071 Jaén
Spain
Phone: (34) 953-212408
Fax: (34) 953-212343
Internet: msgomez@ujaen.es

Elizabeth J. Screaton
Physical Properties Specialist
Department of Geology
University of Florida
PO Box 112120
241 Williamson
Gainesville FL 32611
USA
Phone: (352) 392-4612
Fax: (352) 392-9294
Internet: screaton@geology.ufl.edu

David C. Smith
Microbiologist
Graduate School of Oceanography
University of Rhode Island
South Ferry Road
Narragansett RI 02882-1197
USA
Phone: (401) 874-6172
Fax: (401) 874-6240
Internet: dcsmith@gso.uri.edu

Arthur J. Spivack
Inorganic Geochemist
Department of Earth Sciences
University of North Carolina at Wilmington
7205 Wrightsville Avenue
Wilmington NC 28403-3297
USA
Phone: (910) 256-3721, ext 225
Fax: (910) 256-8856
Internet: Spivack@uncwil.edu

Joan Steurer
Sedimentologist
Department of Geological Sciences
University of Missouri, Columbia
101 Geological Sciences Building
Columbia MO 65211
USA
Phone: (573) 882-0787
Fax: (573) 882-5458
Internet: rhianwen@pop.missouri.edu

Harold J. Tobin
Structural Geologist/Logging Staff Scientist
Department of Earth and Environmental Science
New Mexico Institute of Mining and Technology
801 Leroy Place
Socorro NM 87801
USA
Phone: (505) 835-5920
Fax: (505) 835-6436
Internet: tobin@nmt.edu

Kohtaro Ujiie
Structural Geologist
Department of Geology
National Science Museum
3-23-1 Hyakunin-cho, Shinjuku-ku
Tokyo 169-0073
Japan
Phone: (81) 3-5332-7164
Fax: (81) 3-3364-7104
Internet: k_ujiie@kahaku.go.jp

Michael B. Underwood
Sedimentologist
Department of Geological Sciences
University of Missouri, Columbia
101 Geology Building
Columbia MO 65211
USA
Phone: (573) 882-4685
Fax: (573) 882-5458
Internet: underwoodm@missouri.edu

Moyra Wilson
Sedimentologist
Department of Geological Sciences
University of Durham
South Road
Durham, DH1 4EL
United Kingdom
Phone: (44) 191 374-2501
Fax: (44) 191 374-2510
Internet: moyra.wilson@durham.ac.uk

SCIENTIFIC REPORT

ABSTRACT

Six sites along two transects across the Nankai Trough accretionary prism were successfully drilled during Leg 190, satisfying all leg objectives. Two reference sites at the seaward ends of the Muroto Transect (Site 1173) and the Ashizuri Transect (Site 1177) delineate the stratigraphic framework of the accreting/subducting Shikoku Basin sedimentary section. A thick section of Miocene turbidites and smectite-rich mudstones is present within the subducting section at the Ashizuri site. The turbidites and mudstones are absent in the correlative section at the Muroto site, probably contributing to the difference in prism wedge taper between the two transects, while possibly controlling the seismic character of this active plate boundary.

The décollement in both transects is localized along a stratigraphic unit (~5.9–7 Ma) within the lower Shikoku Basin. This horizon is correlative across both transects through its magnetic susceptibility.

The broad low-chloride zone in the lower Shikoku Basin unit, first identified at Site 808, progressively decreases across the Muroto Transect. This landward-freshening trend is due to both enhanced diagenetic reaction and fluid flow.

Our ideas of the tectonic evolution of the Muroto Transect have been dramatically changed. Accretion of a Miocene and Pliocene turbidite package forms the large thrust slice zone (LTSZ). This event is associated with a shift from a transverse sediment transport system that delivered coarse material from the arc to the trench to an axial transport system that delivers sediment down the trench axis from the east. Growth of the prism from the LTSZ to the toe of the slope (40 km) took place rapidly within the past 2 m.y.

INTRODUCTION

Earth scientists have long recognized the complex interplay of deformational, diagenetic, and hydrologic processes in developing mature mountain belts and have sought to understand the controls on and interactions among these fundamental processes. Accretionary prisms represent unique, accessible natural laboratories for exploring initial mountain building processes. The geometries and structures of accretionary prisms are relatively simple and have been well imaged seismically. Typically, the materials incorporated within prisms are only moderately altered from their original states, so competing active processes can often be isolated, quantified, and reproduced in the laboratory.

The Nankai Trough accretionary prism represents an “end-member” prism accreting a thick terrigenous sediment section in a setting with structural simplicity and unparalleled resolution by seismic and other geophysical techniques. It, thus, represents a superb setting to address ODP’s Long Range Plan objectives for accretionary prism coring, in situ monitoring, and refinement of

mechanical and hydrological models. Our approach for drilling at the Nankai margin includes sites for coring, in situ observation, and long-term monitoring to (1) constrain prism hydrology, mechanical properties, and deformational styles and (2) test existing models for prism evolution.

Leg 190 was the first of a two-leg program concentrating on coring and sampling a transect of sites across the prism within a three-dimensional (3-D) seismic survey. One additional site was drilled to the west to compare along-strike variations in accretionary processes. Leg 196, in 2001, will use logging-while-drilling technology to collect in situ physical properties data and will also install advanced circulation obviation retrofit kits (Davis et al., 1992) for long-term in situ monitoring of prism processes including pressure, temperature, fluid geochemistry, and strain.

BACKGROUND

Geological Setting

The Japanese Island arc system is surrounded by deep trenches, subduction boundaries of the Pacific and Philippine Sea plates (Fig. 1). The Nankai Trough is the subducting plate boundary between the Shikoku Basin and the southwest Japan arc (Eurasian plate). The Shikoku Basin is part of the Philippine Sea plate, which is subducting to the northwest under southwest Japan at a rate of 2–4 cm/yr (Karig and Angevine, 1986; Seno, 1977), slightly oblique to the plate margin. Active sediment accretion is presently taking place at the Nankai Trough.

The record of accretion extends landward to Shikoku Island, where older accretionary prism rocks are exposed (Figs. 2, 3). The Cretaceous and Tertiary Shimanto Belt is characterized by imbricated thrust slices of trench turbidites and melanges composed of ocean-floor basalt, pelagic limestone, radiolarian chert, and hemipelagic shale intermixed with highly sheared scaly shale (Taira et al., 1988). The youngest part of the Shimanto Belt is early Miocene in age. The Shimanto Belt is interpreted as a direct ancient analog of the Nankai accretionary prism (Ohmori et al., 1997).

Subducting oceanic lithosphere of the Shikoku Basin has a history related to the rifting of the proto–Izu-Bonin arc (Taylor, 1992). Rifting of the Izu-Bonin arc started in the Oligocene and culminated in Shikoku Basin seafloor spreading that lasted until ~15 Ma. Three phases of seafloor spreading (Okino et al., 1994) separated the remnant arc, the Kyushu-Palau Ridge, from the active Izu-Bonin arc creating the Shikoku Basin (Fig. 4).

By 15 Ma, most of the Japan Sea ocean floor had formed (Jolivet et al., 1994, Otofuji, 1996). In southwest Japan, widespread igneous activity took place at 17–13 Ma within the forearc, close to the trench (Kano et al., 1991) (Fig. 2). This episode, including high-Mg andesite emplacement, is generally interpreted as reflecting injection of hot asthenosphere and initial subduction of the young Shikoku Basin seafloor (Takahashi, 1999). From 15 to 10 Ma, the collision of the Izu-Bonin arc against Honshu was apparently not vigorous, but was persistent enough to maintain sediment supply to the collisional trough (Aoike, 1999).

From 8 to 6 Ma, a fold belt developed on the Japan Sea side of southwest Honshu (Ito and Nagasaki, 1997). Fold axis trends are predominantly northeast-southwest, indicating northwest-southeast compression. Widely distributed volcanic activity, starting ~8 Ma in southern Kyushu and by 6 Ma in southwest Japan, suggests the establishment of a volcanic front and a deeply penetrating subducting slab (Kamata and Kodama, 1994). In the Izu Collision Zone, the accretion of the Tanzawa massif (part of the volcanic front of the Izu-Bonin arc; Fig. 4) seems to have started at ~8 Ma, with the main phase of collision at ~6–5 Ma (Niitsuma, 1989). Subduction of the Shikoku Basin then at the Nankai Trough formed a frontal accretionary prism to the southwest Japan forearc (Nankai Trough accretionary prism; Taira et al., 1992, Le Pichon et al., 1987) as well as shaped the forearc basins (Okamura et al., 1987; Sugiyama, 1994)

Seismicity, Geodesy, and Thermal Structure

The Nankai Trough has historically generated earthquakes larger than magnitude (M) 8 at intervals of ~180 yr (Ando, 1975, 1991) (Fig. 5). The last one occurred in 1946 and ruptured offshore of Kii Peninsula and Shikoku. Sites 1175 and 1176 are located close to the seaward limit of the rupture zone of the 1946 Nankai earthquake estimated by Ando (1991). Prior to GPS data, Hyndman et al. (1995, 1997) inferred full coupling of prototthrust zone (PTZ) plate boundary based on leveling data. The nationwide permanent Global Positioning System (GPS) network of the Geographical Survey Institute of Japan revealed that the forearc region of Nankai Trough is moving to the west-northwest at 2–5 cm/yr, showing a full coupling of the plate boundary during the current interseismic period (Le Pichon et al., 1998; Mazzotti et al., 2000). GPS data was also analyzed to show the nature of interplate coseismic slip of the Nankai seismogenic zone (Sagiya and Thatcher, 1999).

Hyndman et al. (1995, 1997) found a correlation between the development of a seismogenic zone and the thermal regime, especially in the Nankai Trough subduction zone. The updip limit of the seismogenic zone was found to be in general agreement with the 150°C isotherm, and the downdip limit, with the 350°–450°C isotherm. They proposed that the updip limit coincides with the completion of the smectite-illite transition and the downdip limit with the initiation of ductile deformation of quartz or serpentinization of peridotite mantle.

Geological-Geophysical Database

The geological and geophysical database for the Nankai prism is exceptional. Existing data sets include high-quality industry and academic seismic reflection/refraction data (Aoki et al., 1982; Karig, 1986; Moore et al., 1990, 1991; Stoffa et al., 1992; Park et al., 1999; Park et al., 2000; Kodaira et al., 2000), complete swath bathymetry, and side-scan coverage (Le Pichon et al., 1987; Ashi and Taira, 1992; Taira and Ashi, 1993. Okino and Kato, 1995, Tokuyama et al., 1999), heat flow analyses (Kinoshita and Yamano, 1986; Ashi and Taira, 1993) and three Deep Sea Drilling Project (DSDP)/Ocean Drilling Program (ODP) legs (Legs 31, 87, and 131). Newly acquired 3-D seismic data (*Ewing* 9907/9908)(Bangs et al., 1999; Moore et al., 1999) were used to locate some of the proposed sites (Fig. 6).

The seismic data provide excellent images of the décollement, PTZ, and various structural domains landward of the frontal thrust that guided our choice of drilling targets, and the well-constrained seismic velocities provide the basis for models of dewatering. The swath bathymetry and side-scan data reveal surficial features that further constrained drill hole locations. One of the prominent topographic features in the vicinity of the Leg 190 sites is an embayment of the trench landward slope. Yamazaki and Okamura (1989) interpreted this embayment as an indentation caused by the collision of seamounts with the prism. Recent seismic reflection work and ocean-bottom seismometer experiments on crustal structure support this interpretation (Park et al., 1999; Kodaira, 2000).

Geological Context of Leg 190 Sites

The well-resolved seismic profiles demonstrate several characteristic structural subdivisions across the accretionary prism. Based on 3-D multichannel seismic data obtained by the *Ewing* 9907/9908 cruise (Fig. 6), the accretionary prism along the Muroto Transect can be divided into several tectonic domains from the trench landward (Fig. 7): Nankai Trough axis zone, PTZ, imbricate thrust zone (ITZ), frontal out-of-sequence thrust (OOST) zone, large thrust slice zone (LTSZ), and landward-dipping reflector zone (LDRZ).

Nankai Trough Axis Zone

Results from Legs 87 (Site 582) and 131 (Site 808) indicate that the stratigraphy of the trench floor is composed of the following lithologic units in descending order: trench turbidites (Holocene–Pleistocene), turbidite–hemipelagite transition (Pleistocene), hemipelagite with tephra layers (lower Pleistocene–upper Pliocene), massive hemipelagite (mid-Pliocene to middle Miocene), acidic volcaniclastics (15 Ma), and pillow basalts (16 Ma) (Fig. 8). The trench turbidite unit, supplied mostly through an axial transport system from the source region situated in the Izu collision zone mountain ranges, shows a mixture of volcanic, sedimentary, and metamorphic provenance (Taira and Niitsuma, 1986; Underwood et al., 1993). The lower part of the turbidite unit exhibits a finer grained outer trench turbidite facies in which paleocurrent directions indicate deflected turbidity currents with a transport direction from the outer trench to inner trench (Pickering et al., 1993). The basal acidic volcaniclastic deposit was interpreted as extraordinarily large felsic igneous activity of the outer zone of southwest Japan during the middle Miocene (Taira, Hill, Firth, et al., 1991).

Site 1173 (ENT-01A) is a reference site drilled to basement seaward of the trench axis to provide baseline physical properties and fluid flow measurements (Fig. 9). An additional unit is recognized within the surrounding Shikoku Basin sequence that is not present in the local trench stratigraphy near Site 1173. This unit is stratigraphically below the drilled Shikoku Basin hemipelagic units and is characterized by a well-stratified sequence ~0.7 s thick. This section may correlate with the Miocene turbidite unit identified along the Ashizuri Transect and recovered at Site 1177 within the lower Shikoku Basin facies (hereafter called the Pliocene–Miocene Turbidite Unit) (Figs. 8, 10).

Protothrust Zone

This area represents a zone of incipient deformation and initial development of the décollement within the massive hemipelagic unit. Above the décollement, the sediment thickness increases landward, probably because of tectonic deformation with the development of small faults and ductile strain as documented by Morgan and Karig (1995a, 1995b).

Site 1174 (ENT-03A) is located in the PTZ and sampled a zone of incipient deformation and fluid flow (Fig. 9). This site penetrated into the subducting sediment section all the way to basement. A high priority was to sample pore fluids in great detail across the protothrust, décollement, and the underthrust sediments.

Imbricate Thrust Zone

Landward of the PTZ, a zone of well-developed seaward-vergent imbricate thrusts can be recognized. The thrusts are sigmoidal in cross section with a mean angle of ~30° and a typical thrust spacing of 0.5 km. The frontal thrust forms the seaward edge of the ITZ. At Sites 583 and 808 we cored the frontal part of the imbricated thrust zone.

Site 583 is situated on the hanging wall of the frontal thrust. Although drilling failed to penetrate the décollement zone, good quality physical properties measurements were obtained from all of the holes, providing evidence that sediments dewater under tectonic stresses as they are accreted (Bray and Karig, 1988). The pore-water concentration depth profiles from these sites are far from being detailed enough to provide insight into the nature of fluid flow at this segment of the Nankai Trough (Kastner et al., 1993). The significant geochemical findings were that organic-fueled diagenesis is intense and that at ~600 mbsf methane concentrations and the C_1/C_2 ratios abruptly decrease. Interestingly, similar abrupt decreases were observed at the décollement zone at Site 808. Fluid flow from a deep-seated source could explain these observations.

Site 808 (Figs. 8, 9), which penetrated the whole prism and reached oceanic basement at 1290 mbsf, was particularly successful in terms of physical properties and structural geology measurements because of relatively high core recovery and also because the sediments yielded consistently high-quality paleomagnetic data (Taira et al., 1991; 1992). These data allowed individual core sections and, in some cases, individual structural samples to be oriented relative to the present geographic coordinates. Physical properties generally varied smoothly downhole, except for sharp discontinuities across the frontal thrust and décollement zones. Discrete structures showed distinct concentrations in the vicinity of the fault zones as well as at several horizons above the décollement zone.

Pore waters were recovered throughout the section at Site 808, including the frontal thrust, décollement zone, and underthrust package. Depth profiles for chemical concentrations and isotopic ratios (particularly D, O, Sr, and He) do not support active fluid flow along the décollement, despite its distinct reverse polarity seismic reflection, or along the frontal thrust. They do, however, support lateral fluid flow (1) below the décollement at the approximate depth of the minimum in Cl concentration (~1100 mbsf) and (2) above the décollement along a

horizon marking the lithologic boundary between the volcanic-rich and -poor members of the Shikoku Basin sediments (~820 mbsf). In contrast, detailed 2-D numerical models of fluid flow and solute transport, which incorporate fluid sources from compaction and smectite dehydration, show that episodic, focused fluid flow is necessary to match measured fluid expulsion rates at the seafloor and observed downhole chlorinity values at Site 808 (Saffer and Bekins, 1998). Cores recovered from Site 808 also revealed that fractures within the décollement zone have not been mineralized; the overpressured décollement appears to form a leaky dynamic seal preventing significant lateral or vertical fluid flow. This contrasts with the situations at Barbados and Peru where the major tectonic structures have been mineralized, perhaps implying continuous confined fluid flow.

Frontal Out-of-Sequence Thrust Zone

About 20 km landward from the deformation front, the imbricate thrust packages are overthrust by a younger generation fault system. Because this fault system cuts the preexisting sequence of imbricate thrusts, it is called an OOST. Important and significant deformation also appears within the underthrust Shikoku Basin hemipelagite. The hemipelagic unit seems to be tectonically thickened, probably as a result of duplexing.

Large Thrust Slice Zone

Landward of the frontal OOST is a zone characterized by the development of at least four distinctive out-of-sequence thrusts that separate tectonic slices of either previously imbricated packages or relatively coherent sedimentary sequences. The coherent slices are composed of ~0.7-s-thick (maximum) stratified layers that closely resemble the Pliocene–Miocene Turbidite Unit recognized in depressions in the Shikoku Basin. Underneath these thrust slices, there are packages of strong reflectors that may be composed of thickly underplated Shikoku Basin hemipelagic units. Slope sediment in this zone shows landward tilting suggesting recent active uplift. Bottom-simulating reflectors (BSRs) are weakly developed in this zone and are patchy.

Site 1176 (ENT-06A) drilled through the LTSZ and OOST to sample and investigate the nature of lithology, deformation, physical properties gradient, and fluid flow path that may act as a conduit for deeply sourced fluids from the seismogenic portion of the décollement (Fig. 11).

Site 1175 (ENT-07A) penetrated the slope sediments that cover the LTSZ. Investigation of the age and lithologic characteristics provided information on the history of accretion and deformation of the prism (Fig. 11).

Landward-Dipping Reflectors Zone

Landward-dipping, semicontinuous strong reflectors characterize this zone. Relatively coherent slope sediments cover the sediments exhibiting landward-dipping reflectors (LDRs). This zone appears to be divided into several discrete packages by thrust faults. A BSR is well developed throughout this zone and diminishes abruptly at the boundary between this zone and

the LTSZ. Site 1178 penetrated the slope sediments and the sediments characterized by the LDRs (Fig. 11).

Along-Strike Variation

The structural domains described above show variation along the strike of the prism. Along two parallel transects, separated by ~100 km, sharp differences in prism architecture and structure are evident. The Ashizuri Transect, which includes Leg 87 sites (Figs. 6, 8, 10), displays a well-developed PTZ, containing a series of subparallel dipping discontinuities of unknown origin. These features are not evident within the Muroto Transect PTZ (Fig. 9). Differences in prism taper and seismic character of the décollement along the two transects suggest that the mechanical behavior of the prism differs along strike and that this variability may result from significant differences in pore pressures and fluid flow regimes at the two locations.

Site 1177 is a seaward reference site in the Ashizuri Transect and was designed to establish a baseline of stratigraphic, geochemical, and physical properties for comparison to sites previously drilled during Legs 31 and 87 (Sites 297, 298, 582, and 583).

LEG 190 SCIENTIFIC OBJECTIVES

Spatial Distribution and Temporal Progression of Deformation

Although core recovery at Site 808 was exceptional and physical properties and structural observations complete, the results yield only a one-dimensional view of the interior of the Nankai prism. We have almost no constraint on how various fabrics, structures, physical properties, or geochemistry vary along and across strike or how these variations translate over time. This lack of spatial and temporal control makes it nearly impossible to determine the relationships between deformation, diagenesis, and fluid flow. However, first-order predictions for the distribution of physical properties and structures in two dimensions and the role of fluid pressures in their evolution have been made based on high-quality seismic images, velocities, and dispersed core data. The results of these studies provide models to test and guided the selection of Leg 190 Nankai Trough drill sites, as well as the associated sampling and analyses. To test this distribution of structures and the role of diagenesis and fluid pressure in its development and to obtain better constraints on physical properties from which these models are derived, a transect of sites was drilled during Leg 190 across strike of the prism. Site 1174 (ENT-03A) represents a less-deformed analog to Site 808 and penetrates the incipient thrust fault in the PTZ as well as the vertically thickened sediments in the footwall. Drilling at Sites 1175 (ENT-07A), 1176 (ENT-06A), and 1178 (ENT-09A) penetrated a highly deformed and evolved portion of the prism.

Structural and Hydrologic Evolution of the Décollement Zone

The nature of the décollement zone along the transect remains a big puzzle. Seismic profiles across the transect represent the décollement as a reverse polarity reflection that extends well in front of the deformation front; this has been interpreted to indicate (1) the presence of fluids along a high-porosity fault zone and (2) probably the presence of high pore pressures (Moore and Shipley, 1993). At Site 808, the décollement is a 20-m-thick zone of intensely fractured sediment, with evidence for shear-induced brecciation, pore collapse, and local phyllosilicate reorientation (Byrne et al., 1993). Sediments from within the décollement have much lower porosities than samples from above and below.

A subtle mottled texture in some samples led Maltman et al. (1993) to infer localized zones of elevated fluid pressure within the zone. The normal polarity seismic reflection marking the décollement beneath the prism toe along the Ashizuri Transect was sampled at Site 1177. We sampled the décollement zone at critical points beneath the Nankai prism (Site 808) and PTZ (Site 1174) to document the spatial variations in structure and fluid pressure to test these hypotheses of décollement formation and evolution.

Chemical Gradients and Fluid Flow Paths

The origin of the Cl concentration depth profile is of great importance to the understanding of the hydrogeochemistry of the Nankai Trough Muroto region. Site 808 is characterized by a broad region of Cl concentrations that are lower than seawater (~20% less than seawater) within the Shikoku Basin hemipelagic section (~560–1240 mbsf), with a minimum concentration in the underthrust section at ~1100 mbsf (Kastner et al., 1993). Some of the shipboard scientists believe the preliminary one-dimensional modeling of this profile excludes the possibility of in situ production of water, hence requiring its introduction from elsewhere. In addition, 2-D models of smectite dehydration and fluid flow show that meither in situ dehydration nor steady state fluid flow can produce the observed freshening (Saffer and Bekins, 1998). It is important to note that these calculations are strongly dependent on porosity and mineralogical data from Site 808 and may change significantly with revised porosity values or additional information about smectite content. The chemical and isotopic signatures of the pore fluids suggest a deep-seated, elevated temperature (>150°C) source. It seems that a combination of active or episodic lateral fluid flow along one or more sediment horizons and fluid advection may be responsible for this striking Cl zone. The sites along the Muroto Transect are aimed at understanding the lateral variability of fluid flow.

Contrasting Stratigraphic and Deformational Framework along Strike

Seismic profiles of the Ashizuri and Muroto Transects across the prism indicate significant differences in prism architecture, structure, and physical properties in the two locations. These are assumed to reflect variances in fluid flow regimes, but, to date, the mechanisms responsible for such variability are unknown. Structural differences between the Ashizuri and Muroto regions suggest that there may be significant variation in how deformation is accommodated

along the two transects; this contrast in behavior may also shed some light on the hydrologic differences. The taper of the prism toe along the Ashizuri Transect (8°–10°) is greater than that of the Muroto toe (4°–5°), a situation that may arise from relatively stronger décollement to the west or lower internal sediment strength. A strong décollement might arise from a lack of pressurized fluids within the fault zone, consistent with the normal polarity reflection. Alternatively, this difference in strength might be due to a variation in clay mineralogy in the décollement zone. Site 1177 drilled through the upper 300 m of the section previously cored at Site 582 and cored the subducting sediment section to document its clay mineralogy.

SITE SUMMARIES

Site 1173 Summary

We completed drilling at Site 1173 in the trench outer margin (Fig. 9) in order to provide a reference for the predeformation status of geological and geochemical characteristics of the incoming sedimentary section. We recognized five lithostratigraphic units (Figs. 8, 12): Unit I (0 to 102 mbsf) is Quaternary in age and composed of sandy to muddy turbidites of the outer Nankai trench–wedge facies; Unit II (102 to 344 mbsf) is Quaternary to Pliocene in age and made up of hemipelagic mud with abundant interbeds of volcanic that were ash probably derived from the Kyushu and/or Honshu volcanic arcs (upper Shikoku Basin facies; Fig. 13); Unit III (344 to 688 mbsf) consists of Pliocene to middle Miocene bioturbated silty claystone (lower Shikoku Basin facies); Unit IV (688 to 725 mbsf) is probably middle Miocene in age and composed of variegated siliceous claystone and silty claystone (volcaniclastic facies); Unit V (725 mbsf) is middle Miocene basalt. The boundary between Units II and III is controlled, in part, by diagenesis. There is an abrupt loss of unequivocal ash beds and replacement by siliceous claystone (Fig. 14).

Biostratigraphic age control provided by calcareous nannofossils identified a total of 23 biostratigraphic events. The continuous sedimentary section spans the time interval from the Pleistocene (Subzone NN21b) through the middle Miocene (Zone NN5). Magnetostratigraphy clearly identified the Bruhnes/Matuyama boundary (0.78 Ma), Matuyama/Gauss boundary (2.581 Ma), the Gauss/Gilbert boundary (3.58 Ma), and the termination of the Gilbert Chron (5.894 Ma). Paleomagnetic and biostratigraphic ages indicate high sedimentation rates (450–650 m/m.y.) for the turbidite deposits, decreasing rates for the upper Shikoku Basin section (72–77 m/m.y.), and lowest rates for the lower Shikoku Basin (27–37 m/m.y.).

Deformation structures in Hole 1173A are sparse oceanward of the prism, as expected from a reference site. The section above 375 mbsf is characterized by horizontal bedding with occasional microfaults between 250 and 275 mbsf. Bedding dips reaching 20°, perhaps due to lateral extension associated with normal faulting, occur abruptly at 375 mbsf and continue down to 550 mbsf and sporadically to the bottom of the hole. A 30-cm zone of foliated breccia indicates somewhat greater deformation around 440 mbsf. Lower cores contain rare mineralized

veins; a few possible dewatering structures such as thin, sediment-filled veins reflect early compaction processes.

Variations in physical properties correlate well with the lithostratigraphic units. High variability characterizes the turbidites of the outer Nankai Trench wedge, and porosities decrease with depth. Porosity increases at the boundary between the outer Nankai Trench wedge and the upper Shikoku Basin facies and continues to increase slightly with depth. These elevated porosities deviate from a typical compaction profile. An increase in *P*-wave velocities within this interval of increasing porosity suggests that there may be slight cementation. At the boundary between the upper and lower Shikoku Basin facies (~340 mbsf), grain densities increase slightly and porosities decrease sharply. This porosity decrease is accompanied by increasing thermal conductivity, *P*-wave velocity, and resistivity. A gas-probe permeameter showed that ash bands in the upper Shikoku Basin sediments are significantly more permeable than the hemipelagites, although the contrast disappears in the lower Shikoku Basin section.

Seven reliable determinations of downhole temperatures were made at depths of 35 to 284 mbsf in Hole 1173A, using the advanced hydraulic piston corer (APC) temperature tool, water-sampling temperature probe (WSTP), and Davis-Villinger temperature probe (DVTP). The measured temperatures closely define a linear gradient of 0.183°C/m in the upper 300 m, where the average measured thermal conductivity is ~1.0 W/(m·K); this yields a conductive heat flow of ~180 mW/m^2 at Site 1173. Deeper than 300 m, thermal conductivities increase by 30%–50%, so the gradient should decrease proportionally, and in situ temperatures of ~110°C are estimated for the bottom of the hole— similar to the basement temperature estimated for Site 808. The heat flow value is somewhat higher than prior determinations of high heat flow near the site and greater than the predicted heat transfer for the 15-m.y. crustal age.

A high-resolution pore fluid concentration-depth profile shows that the pore fluid chemistry has been extensively modified from seawater by both microbially mediated reactions and by abiological, inorganic fluid-rock reactions. The chemical modifications from the microbially mediated reactions provide crucial independent information on the depth range, intensity, and nature of microbial activity in the deep subsurface. Each inorganically controlled dissolved species analyzed (i.e., Cl, Ca, Mg, SiO_2, K, and Na, shows a distinct to sharp discontinuity at 340 mbsf, which corresponds to the lithologic boundary between Units II and III. Furthermore, minima in Cl and Na concentrations and significant inflections in the Mg and Ca profiles occur at ~380–390 mbsf. These features suggest that this horizon may be hydrologically active. A broad ~350-m-thick low-Cl zone within Unit III, with ~9% dilution relative to seawater, requires a source of low-Cl fluid. The similarities between this low-Cl zone and that at ODP Site 808 are striking, except that at Site 808 the dilution relative to seawater is more than twice that observed at this site.

Total organic carbon values are low (average = 0.35 wt%) and decrease with depth (0.85 to 0.20 wt%). The C/N ratios indicate the presence of marine organic matter throughout the hole and show a slight increase in the lower ~200 m. The low sulfate and high methane concentrations in the upper section below the sulfate reduction zone are consistent with a

bacterial origin. The increase in sulfate concentrations from ~400 to 700 mbsf coupled with the low concentrations of methane may indicate that sulfate is inhibiting production of hydrocarbons that were more abundant at Site 808. The presence of low concentrations of light hydrocarbons (ethane and propane) below 300 m to total depth may be due to some in situ thermal maturation of kerogen in the sediments. The low concentrations of methane at depth and the lack of evidence for any migration of hydrocarbons from above the facies transition (347.3 mbsf) support these conclusions. The microbes observed (~480 m) at temperatures above 90°C in the presence of elevated sulfate concentrations suggest that methanogenesis due to microbial activity is not completely inhibited, although at these temperatures, thermogenic hydrocarbons are likely being produced.

Samples taken for bacterial enumeration show that bacteria are present in all samples to 500 mbsf and thereafter are absent (the detection limit is 4.75×10^5). The population profile generally follows the average line obtained from other ODP sites for the upper 250 m of the hole with a rapid decrease in population size in the upper few meters as the sulfate was depleted. Between 43 and 80 mbsf, there is a significant (sevenfold) increase in bacterial numbers coincident with elevated methane concentrations. At 250 mbsf there is both a temperature boundary for bacteria (45°–50°C, the change from mesophilic to thermophilic populations) and significant differences in interstitial water (IW) chemistry, which complicates interpretation. Further changes occur in IW chemistry at a lithologic boundary at 343 mbsf. Between 250 and 460 mbsf, bacterial numbers are lower than average. Another microbiological temperature boundary (thermophilic to hyperthermophilic populations) occurs at 460 mbsf as temperatures exceed 80°C. One positive enumeration was made in this zone at 500 mbsf and ~85°C, where populations increase by a factor of 13. At this depth there were relatively high concentrations of organic carbon plus increasing concentrations of sulfate, methane, and hydrogen that could support a deep hyperthermophilic population of sulfate-reducing bacteria.

Tracer tests were successfully carried out on two APC cores and two extended core barrel (XCB) cores with both perfluorocarbon tracer (PFT) and fluorescent microspheres. PFT was detected in the center and midway between the center and the outside in some APC core sections; however, PFT was absent from the center of the XCB core sections. In contrast, microspheres were generally absent in samples taken midway between the center and the outside of the core in both APC cores and one of the XCB cores and were only present in the centers of some of the XCB core sections. These results suggest that intrusion of microspheres into the center of the cores was a result of postrecovery handling and not diffusion of drilling fluid during coring. This is the first time fluorescent microsphere tracers have been used during the collection of cores with the XCB.

Hole 1173A was logged with both the triple combination logging string (spectral gamma ray, dual-induction resistivity, lithodensity, and neutron porosity tools) and the Formation MicroScanner and dipole sonic imager (FMS-sonic) tools. The interval from 65 to 373 mbsf was logged in two passes, and high-quality compressional and shear travel time data and FMS images were acquired. During the second pass, a new low-frequency (<1 kHz) dipole source was

used on the DSI and produced excellent shear waveforms despite the very low formation velocity. Logging results are generally consistent with the homogeneous hemipelagic core lithology, with few identifiable lithologic boundaries in the logged interval. Density is low from 97 to 336 mbsf, with a slight gradual decrease with depth, then sharply higher in the 358–440 mbsf interval. Compressional and shear wave velocities are nearly constant with depth to 225 mbsf, then increase with depth. Velocities decrease sharply in the short logged interval below 348 mbsf, corresponding to the Unit II/III boundary. Numerous ash layers and other sedimentologic and diagenetic features observed in the cores were well imaged by both FMS passes, which should permit high-resolution core-log integration.

Site 1174 Summary

Site 1174 (ENT-03A) is located in the protothrust zone of the Nankai accretionary prism (Fig. 9) and is designed to sample a zone of incipient deformation. When combined with our reference Site 1173 (~11 km seaward) and Site 808 (~2 km landward at the frontal thrust), Site 1174 will provide a transect of structural, physical properties, and geochemical gradients across the deformation front of the accretionary prism.

We recognized five lithostratigraphic units and three subunits at Site 1174 (Figs. 8, 15). Unit I (slope-apron facies) is Quaternary in age and extends from the seafloor to a sub-bottom depth of 4.00 mbsf. This facies is composed mostly of mud that was deposited on the lowermost trench slope by hemipelagic settling. Unit II (trench-wedge facies) is Quaternary in age and includes three subunits. Subunit IIA (axial trench–wedge facies) extends from 4.00 to 314.55 mbsf and is characterized by thick sand turbidites, silt turbidites, and hemipelagic mud (Fig. 16). The lithologies of Subunit IIB (314.55–431.55 mbsf) are limited to silt turbidites and hemipelagic mud, whereas Subunit IIC (431.55–483.23 mbsf) is composed of hemipelagic mud, volcanic ash, and silt turbidites. The gradual transformation in facies character downsection is consistent with a change in depositional environment from the outer trench wedge to abyssal floor. Unit III (upper Shikoku Basin facies) is Quaternary to Pliocene in age and extends from 483.23 to 660.99 mbsf. Lithologies within this unit include hemipelagic mudstone and volcanic ash; the lower unit boundary coincides with the deepest identifiable bed of vitric tuff. In contrast, Unit IV (lower Shikoku Basin facies) contains mostly bioturbated mudstone with sporadic interbeds and nodules of carbonate-cemented claystone and siliceous claystone. Replacement of glass shards by smectite and zeolites (clinoptilolite or heulandite) increases gradually with depth and is more extreme in finer grained deposits. As a consequence, both ash to bentonite diagenesis and temporal changes in pyroclastic influx govern the lithologic distinction between the Upper and lower Shikoku Basin facies. The unit boundary shifts upsection as Shikoku Basin deposits migrate toward the Nankai deformation front and become increasingly affected by rapid burial and heating beneath the trench wedge. The lowermost stratigraphic unit at Site 1174, Unit V, begins at a depth of 1102.45 mbsf. We drilled only 8.86 m of variegated claystone in this middle Miocene volcaniclastic facies.

Deformation bands are well developed between 218 and 306 mbsf (Fig. 17) and are concentrated in two oppositely inclined sets striking at 033° with the acute bisectrix inclined 10°NW from vertical (Fig. 18). They occur immediately above a narrow but abruptly sheared interval which, with indications of reverse movement and a paleomagnetically restored southeast dip, seems to be a backthrust. Between 470 and 506 mbsf, fractured and markedly steepened bedding may represent a thrust; no significant deformation was seen in the cores equivalent to the thrust apparent on the seismic profile at 550 mbsf. Narrow, widely spaced zones of fractures and brecciation characterize the interval between 688 and 807 mbsf. Between 807.6 and 840.20 mbsf an irregular downward increase in intensity of inclined fractures and fineness of brecciation defines the basal décollement, thicker and more heterogeneous than at Site 808 but more thoroughly comminuted in its lower part (Figs. 19, 20). The underthrust sediments show little tectonic deformation apart from bed steepening between 950 and 1000 mbsf and, together with shearing, around 1020 mbsf.

Nannofossil assemblages are indicative of the Pleistocene (Subzone NN21b) to middle Miocene (Zone NN6) ages. Fifteen biostratigraphic events are recognized. Nannofossils are common and generally moderately preserved in the Pleistocene, whereas Pliocene and Miocene nannofossils are rare and mostly poorly preserved. Sedimentation rates based on biostratigraphy are 630–770 m/m.y. for the late Quaternary and are significantly lower (11–125 m/m.y.) for deposits >0.8 m.y.

Paleomagnetic results indicate that the Brunhes Chron (0–0.78 Ma) ranges from 0 to 543.15 mbsf and extends through the trench-wedge turbidites. The Matuyama Chron occurs from 543.15 to 685.95 mbsf, the Gauss Chron from 685.95 to 727.85 mbsf, and the Gilbert Chron from 727.85 to 802.07 mbsf. High magnetic intensities occur from 0 to ~550 mbsf, below which they drop to low values to the bottom of the hole.

The main characteristics of the interstitial water concentration-depth profiles at Site 1174 are similar to those at Site 808. There is an intense, and therefore a very shallow, sulfate reduction zone, alkalinity and ammonium concentrations peak in the uppermost 200 m of the section, and the solutes that are controlled by fluid-rock reactions, such as Cl, Na, and Si, have sharp changes in their gradients at a depth that corresponds to the boundary between the trench wedge and Shikoku Basin facies (lithostratigraphic Units II/III boundary). The chemical changes across the prime tectonic feature, the décollement, are subtler. At the depth that corresponds to the thrust intersection (~470 ± 5 mbsf), there are significant transient features, most distinctly exhibited in the Cl and Si concentrations, that may indicate active hydrologic activity. A high-resolution record of pore fluid chemistry was recovered across and within the Nankai Trough décollement for the first time. A low-Cl zone in the 200-m interval below the décollement, with minimum concentrations that are ~17% diluted relative to seawater, occurs at an almost identical distance below the décollement at Site 808. The dilution, however, is ~21% at Site 808, ~17% at Site 1174, and considerably less (~9%) at reference Site 1173. In the lowermost ~100 m of the underthrust section, Cl concentrations increase, approaching seawater concentration at 1110

mbsf. Hydration reactions in the lower volcaniclastic or an underlying upper basement fluid flow system may be responsible for the increase in the Cl concentrations.

A local Cl maximum of 496 mM within the décollement has smoothly diffused ~50 m above the décollement, whereas there is a very sharp decrease (~10 mM) in the 10 m below the décollement. The cause of the Cl maximum in the décollement is as yet unclear.

Dissolved silica concentrations appear to be controlled by biogenic silica dissolution in the trench-wedge sediments, by volcanic ash diagenesis in the upper Shikoku unit, and by the low-Cl source plus in situ silicate reactions at >70° to ~130° in the Lower Shikoku unit. Dissolved sulfate increases below the sulfate reduction zone, 1–2 mM below the upper and lower Shikoku Basin boundary sediments, at ~660 mbsf, reaching 8–10 mM below the depth interval of the Cl minimum and remaining constant to the bottom of the section. At Site 1173 the first sulfate increase below the sulfate reduction zone is observed at a much shallower burial depth, ~400 m shallower than at Site 1174. The sulfate distributions at these sites may reflect a dynamic relationship among sedimentation rates, temperature, and microbial sulfate reduction rates.

Organic matter decreases with depth and low total organic carbon (TOC) values are low (0.90 to 0.11 w%; average = ~0.38 wt%) in the core. The C/N ratios indicate the presence of marine organic matter with only a slight increase in the upper trench–wedge facies (~200 mbsf) and in the lower Shikoku Basin facies below the décollement (~1000 mbsf). Discrete intervals of elevated methane concentrations are present between 225 and 700 mbsf. Minor amounts of ethane (C_2; 200–800 mbsf) and propane (C_3; 400–650 and 950–1110 mbsf) are likely because of some in situ thermal maturation of organic matter. There appears to be restricted flow of both C_2 and C_3 across the décollement, suggesting that the presence of higher hydrocarbons above the décollement may be due to migration.

Microorganisms were enumerated in 40 samples collected from the surface to 1100 mbsf at Site 1174. With the exception of two samples with low abundances (~1.8×10^6 cells/cm^3) in the sandy layers at 26 and 66 mbsf, abundances from the surface to 400 mbsf were close to values predicted based on data from previous ODP sites. Abundances were lower than predicted below 400 mbsf. The decrease may relate to the relatively high temperature gradient at Site 1174. Cell counts dropped below the detection limit at 528 mbsf and remained so until just above the décollement. Abundances at 778 and 789 mbsf were 4.8 and 4.2×10^6 cells/cm^3, respectively; no cells were detected below these depths. Nineteen whole-round samples were used to inoculate anaerobic growth media and were maintained at the estimated in situ temperature. Samples were chosen from the surface through the known hypothermophilic region (113°C), and subsamples at five depths were targeted for incubation at in situ pressure and temperature.

Porosities within the axial and outer trench–wedge facies (Subunits IIA and IIB) are characterized by high variability and decrease with depth. Porosity decreases at the top of the trench to basin transition facies (Subunit IIC). Within the transitional facies, porosities are less scattered and decrease slightly with depth. The upper Shikoku Basin facies (Unit III) is characterized by nearly constant porosities, which is a deviation from normal compaction trends. Surprisingly, a high velocity interval between 510 and 520 mbsf is associated with an interval of

elevated porosity. At the top of the lower Shikoku basin (Unit IV; ~660 mbsf) another high-velocity interval occurs. Porosities within the lower Shikoku Basin facies resume a compaction trend of decreasing porosity with depth. Porosities increase sharply by 2%–4% at the top of the underthrust sequence. This porosity increase is accompanied by a decrease in velocity and increase of electrical conductivity. However, the anisotropy of electrical conductivity is higher in the underthrust sediments than above the décollement zone. Porosities and velocities increase with depth within the underthrust sediments, whereas electrical conductivities decrease.

Uncalibrated gas permeameter measurements were made throughout the section. Shallower than 600 mbsf, silt-rich and ash horizons showed higher values than the silty clays. The axial trench–wedge sands gave the highest values and the lowermost silty clays recovered gave the lowest.

In situ temperature measurements to a depth of 65.5 mbsf and laboratory thermal conductivity measurements indicate a heat flow of 180 mW/m^2. If heat flow is purely conductive and steady state, a temperature of 140°C is projected for the bottom of the hole.

Site 1175 Summary

Site 1175 (ENT-07A) was designed to penetrate the slope sediments that cover the large thrust slice zone just landward of a major out-of-sequence thrust (OOST; Fig. 11). Investigation of the age and lithologic characteristics would provide information on (1) the history of accretion, uplift, and deformation of the prism, and (2) sedimentation within a trench-slope basin.

We cored three lithostratigraphic units at Site 1175 (Figs. 8B, 21). Unit I (upper slope–basin facies) begins at the seafloor and ends at a subbottom depth of 224.75 mbsf. Lithologies include nannofossil-rich hemipelagic mud, volcanic ash, and thin turbidites that range in texture from sand to silty sand, clayey sand, and silt. The most characteristic feature of Unit I is the common occurrence of contorted stratification (Fig. 22). There are eight discrete zones of soft-sediment deformation. Typical manifestations include variably inclined bedding, small-scale folding, and, in extreme cases, stratal fragmentation. The disruption probably was caused by submarine slumps and debris flows. Unit II (middle slope–basin facies) extends from 224.75 to 301.64 mbsf. Lithologies include hemipelagic mud, poorly sorted muddy sand to sandy mud, sporadic interbeds of volcanic ash, and rare occurrences of thin sand or silt turbidites. The unusual lithology of muddy sand is diagnostic of Unit II and probably was transported downslope by sandy debris flows or mudflows. Unit III (slope to prism transition) begins at 301.64 mbsf and ends at 435.40 mbsf. This unit is typified by hemipelagic mud with numerous interbeds of silt and silty sand turbidites. The most striking lithology, however, is gravel to pebbly mudstone (Fig. 23). Its characteristics include disorganized and poorly sorted clast fabric, lack of internal stratification, partial to complete support of clasts by a matrix of clayey silt, and subrounded to rounded clasts up to 5.5 cm in size. A polymictic clast population was transported downslope by debris flows. The boundary between the lowermost slope sediment and the top of the

accretionary prism cannot be defined with certainty using lithologic criteria, but it probably occurs within the upper 25–30 m of Unit III.

Site 1175 exhibits little evidence for tectonic deformation. However, the upper 205 m shows intervals of recumbent, isoclinal slump folding and disaggregated sediment, interlayered with subhorizontal intact bedding. Fold orientations suggest the slumping was northward directed. Below 220 mbsf, bedding is subhorizontal, except for localized chaotic zones between 350 and 388 mbsf and dips up to 21° at 400 mbsf. Core-scale faults, probably compaction related, occur from 298 to 302 mbsf and sporadically from 340 to 435 mbsf. Possible web structure occurs in sands at 406.9 and 425.8 mbsf; near the bottom of the hole, an indurated sand contains several low-angle small faults.

Biostratigraphic age control was provided by calcareous nannofossils that are well preserved and abundant throughout the section. A total of nine biostratigraphic events were identified within the nannofossil assemblages. The continuous sedimentary record spans the time interval from the Pliocene (Zone NN18) through the Pleistocene (Subzone NN21b). Based on the biostratigraphic age model, sedimentation rates for the upper sedimentary units show high sedimentation rates (0.52 m/k.y.) for the upper to middle slope–basin deposits, with decreasing rates for the slope to prism transition (0.13 m/k.y.).

Hole 1175A inclination data after alternating field (AF) demagnetization at 30 mT allowed interpretation of geomagnetic polarity changes from late Pliocene to Pleistocene. The 0.78 Ma Brunhes/Matuyama boundary is interpreted to occur at 298.80 mbsf (interval 32X-5, 80 cm). Seven short reversal events were observed in the Brunhes Chron and may represent geomagnetic excursions.

In Hole 1175A, pore fluids are less intensively modified from seawater than the pore fluids in Holes 1173A and 1174A. The main characteristics of the pore fluid concentration-depth profiles indicate that the intense microbially mediated reactions occur in the top <200 mbsf of the section. Microbial sulfate reduction is complete at ~15 mbsf. The alkalinity maximum also occurs at this depth. Only relatively small changes in the chemical gradients occur throughout the section and across the major lithologic boundaries in the abiogenic components. Diatom dissolution controls the Si concentrations in the pore fluids. Because of the rather low geothermal gradient of 54°/km, volcanic ash alteration is as yet insignificant. Instead of ash alteration, as indicated by the Ca, Mg, and alkalinity concentration-depth profiles, carbonate, particularly dolomite, diagenesis is the dominant diagenetic reaction. Dolomite forms both by direct precipitation of authigenic dolomite and by replacement of precursor biogenic calcite, which is abundant in this section. Carbonate diagenesis should influence some of the index physical properties such as porosity and density. An as yet unidentified silicate reaction at greater depth below the section drilled controls the concentration profiles of K, Na, Si, and alkalinity below ~300 mbsf, corresponding to lithostratigraphic Unit III. The clearly observed diffusion of lower chlorinity interglacial water into the pore fluids at Sites 1173 and 1174 is absent at this site. It must have been erased by the widespread slumping in Unit I of this section over the past ~10 k.y. Fluid flow does not play a role at this site.

The sediments at Site 1175 contain low inorganic carbon (~0.11–4.59 wt%), and carbonate contents range up to 40 wt%, resulting in very immature organic matter and low hydrocarbon abundances. The low sulfate and high methane concentrations in sediments below the sulfate reduction zone and throughout Hole 1175A are consistent with a bacterial origin.

Bacterial abundance was enumerated in 18 samples obtained at Site 1175. The abundance near the surface is 6.97×10^7 cells/cm^3 and declines rapidly, which is consistent with the decrease in sulfate concentrations. Abundances increase below14.6 mbsf consistent with increases in methane concentrations. The sample at 50.8 mbsf is notable in that it contains 7.28×10^7 cells/cm^3 (i.e., slightly more bacteria than the near-surface sample). This is followed immediately with almost the lowest population enumerated of 3.71×10^5 cells/cm^3 at 59 mbsf. The deepest sample is 400 mbsf with 3.59 × 105 cells/cm^3, equivalent to 0.5% of the near-surface population. Estimates of drilling fluid intrusion into the interior of the cores examined at this site range from below detection to 0.02 ：L/g. In addition to the onboard assays, 17 whole-round cores were taken for shipboard enrichment cultures, cell viability, and shore-based microbiological analysis to measure potential bacterial activities, culture microorganisms, characterize nucleic acids, and investigate fatty acid biomarkers.

Porosities within the upper slope–basin facies (Unit I) are characterized by high variability and decrease slightly with depth from values of 62%–70% at the mudline to 61%–68% at ~100 mbsf. Porosities decrease abruptly at ~100 mbsf to values of 57%–61% and then decrease gradually to the transition between the upper and middle slope–basin facies (220 mbsf). Below 220 mbsf (within the middle and lower slope–basin facies), porosity decreases more rapidly with depth than in the upper slope–basin facies, reaching values of 38%–47% at 400 mbsf. The rapid decrease in porosity below 220 mbsf coincides with increasing *P*-wave velocity. There is no clear change in porosity, bulk density, or grain density at the depth of the middle slope–basin/lower slope–basin facies boundary (301 mbsf; Units II and III). A spike of high velocity and impedance 20 m above this transition may correspond to a seismic reflector. The depth of this spike coincides with the depth of the upper unconformity on the depth converted seismic profile. Four successful in situ temperature measurements at Site 1175 indicated a thermal gradient of 0.054°C/km.

Gas-probe permeameter measurements illustrate the huge influence of lithology. Overall results for the hemipelagic clays that dominate the section are uniformly lower than those in a coarse, friable black ash at 23 mbsf and turbiditic sands between 60 and 90 mbsf, which yield an exceptionally high value exceed 8×10^{-12} m^2. Thin bands of white-gray ashes also give relatively high values, in line with shallow, unaltered ashes at the other sites.

This site revealed that the age of accretion of the large thrust slice zone is very young (<2 Ma). The young age of the accretion indicates rapid growth of the frontal part of the Nankai accretionary prism, ~40 km oceanward growth in 2 m.y. This rate of growth provides a first order constraint for kinematic, structural, and hydrogeologic modeling of the prism.

Site 1176 Summary

The objective of Site 1176 was to determine the nature of accreted sediments of the large thrust slice zone as well as deformation and fluid flow related to a major out-of-sequence thrust (Fig. 11).

We recognized three lithostratigraphic units at Site 1176 (Figs. 8B, 24). Unit I (upper slope–basin facies) extends from the seafloor to 195.79 mbsf. Its lithologies include nannofossil-rich mud, volcanic ash, and sand to silt turbidites. The principal processes of sedimentation for Unit I were hemipelagic settling and turbidity currents, with occasional volcanic ash falls and remobilization by slumping. Unit II (middle slope–basin facies) extends from 195.97 to 223.54 mbsf. In addition to typical hemipelagic mud, Unit II contains sandy mudstone and rare beds of volcanic ash. Deposition of this facies occurred via muddy debris flows, routine settling of suspended sediment, and occasional ash falls. Unit III was cored to a depth of 440.36 mbsf and contains abundant interbeds of sand to silt turbidites, hemipelagic mudstone, pebbly mudstone, gravel (Fig. 25), and rare volcanic ash. The primary depositional environment for this unit was probably a trench-fan system fed by a transverse submarine canyon. The petrographic compositions of sands and gravels, rich in sedimentary lithic fragments and quartz, show that their provenance is the Outer Zone of southwest Japan as typically represented by the Shimanto Belt. The unconformity between the lowermost slope sediment and the top of the accretionary prism probably coincides with the boundary between Units II and III.

Site 1176 can be divided into two structural domains: slope basin and accretionary prism. Deformation of the slope-basin sediments (0–224 mbsf) is characterized by inclined bedding intervals in which slump folds together with contorted and chaotically mixed bedding are locally developed. These features are interpreted to record the effects of active tilting and uplifting of the slope basin. Small faults are thought to result from extensional response to this tilting and uplift of the basin and/or burial compactional strains. In contrast, deformation structures are almost absent in the accreted sediments (below 224 mbsf), although core recovery was very poor. However, the apparently consistently horizontal bedding may reflect the flat part of a hanging-wall anticline formed in association with an underlying thrust.

Biostratigraphic age control was provided by calcareous nannofossils. Nannofossil assemblages are of Pliocene (Zone NN16) to Pleistocene age (Subzone NN21b) according to nine recognized biostratigraphic events. Although nannofossils are common and generally moderately preserved in the upper Pleistocene, nannofossils from sediments older than 1 Ma are rare and poorly preserved. Age models based on biostratigraphy indicate sedimentation rates of ~0.07–0.26 m/k.y.

Inclination data of Hole 1176A after AF demagnetization at 30 mT provided useful information for interpretation of geomagnetic polarity changes from the late Pliocene to the Pleistocene. The Brunhes/Matuyama boundary (0.78 Ma) is interpreted to occur at 199.55 mbsf. Seven short reversal events were observed in the Brunhes Chron and may represent geomagnetic excursions in this chron.

The most intense microbially mediated reactions occur in the top <100 mbsf of the section. Microbial sulfate reduction is complete at ~20 mbsf. In the top half of this zone the sulfate reduction rate decreases linearly with depth, whereas in the lower half maximum sulfate reduction occurs at the base of the zone; the alkalinity produced is involved in carbonate reactions, and the ammonium produced is involved in clay ion exchange reactions.

The alkalinity maximum and Ca and Mg minima coincide with the depth of the base of the sulfate reduction zone; thus, this depth interval is also characterized by intense carbonate diagenesis. The Ca and Mg concentration profiles indicate that in the sulfate reduction zone both authigenic dolomite precipitation and replacement of a precursor biogenic calcite occur. Deeper, however, through the upper and middle slope–basin section, replacement of a precursor calcite is the only dolomitization reaction.

Because of the low geothermal gradient of 56°C/km, volcanic ash or other silicate diagenetic reactions are minimal. Diatom dissolution may control the pore fluid silica concentration. At the base of the section, a residual pore fluid exists, having close to seawater composition as indicated by the return to seawater concentrations of all abiogenic components, except for K. The Cl concentration profile indicates Cl diffusion to a low-Cl zone that may be associated with the out-of-sequence thrust. The low-Cl fluid is enriched in Ca and depleted in Na, K, and Mg. A chemically similar deep-seated fluid was identified at Site 1174.

Diffusion of low-chlorinity interglacial seawater into the sediment section is not observed at this site because the top ~50 mbsf of the section was deposited in the past <10 k.y., during the interglacial; therefore, concentrations are constant. At greater depths, the residual signal from the glacial ocean seawater has been erased by diffusion.

The total carbon content for the sediments examined between 200 and 401.6 mbsf at Site 1176 ranged from 0.05 to 2.25 wt%. The highest carbon value (2.25 wt% at 340 m) was dominated by a terrestrial component likely derived from fan debris flow to the trench sediments. The sulfur content showed a similar trend to TOC with the highest values of sulfur (1.05 and 2.07 wt%) coincident with the highest TOC values (0.86 and 2.25 wt%). The inorganic carbon (~0.05–2.6 wt%) and high carbonate content (up to ~35 wt%) are similar to values observed at Site 1175. Methane concentrations in sediments below the sulfate reduction zone (~9.5 m) are consistent with a bacterial origin. Methane dominates the composition of the hydrocarbons measured throughout Hole 1176A.

Bacterial abundance was enumerated in 18 samples obtained at Site 1176. Abundance at the surface was 6.67×10^8 cells/cm^3. The deepest sample is 363.49 mbsf with 1.71×10^6 cells/cm^3, representing 0.25% of the surface population. Bacterial populations decline rapidly from the surface, consistent with the decrease in sulfate concentrations to near zero at 14.6 mbsf. The decline in bacterial abundance with depth follows the predicted depth/population size relationship very closely. In addition to the onboard assays, 11 whole-round cores were taken for shipboard enrichment cultures, cell viability, and shore-based microbiological analysis to measure potential bacterial activities, culture microorganisms, characterize nucleic acids, and investigate fatty acid biomarkers.

Porosities decrease gradually with depth in the upper slope–basin facies (Unit I), from values of ~65%–73% at the mudline to 55%–60% at 200 mbsf. Within the upper slope–basin facies, there is considerable scatter in porosity, with values ranging from 51% to 73%. This scatter may be related to the inferred deposition of this unit by slope failure processes. No clear changes in index properties occur at the boundary between the upper and middle slope–basin facies (Units I and II). Within the middle slope–basin facies (Unit II), porosity continues to decrease gradually with depth, following the same trend as observed for the upper slope–basin facies. Changes in index properties correlate with the boundary between the middle slope–basin and accretionary prism facies (Units II and III) at 225 mbsf. Porosity decreases from 53%–57% to 48%–54% across this boundary. Velocity and formation factor also increase at the top of Unit III. Within Unit III, porosities decrease with depth, reaching ~40%–47% by ~310 mbsf. From this depth to 405 mbsf, porosities remain constant, with values ranging from ~40%–47%.

Five successful in situ temperature measurements indicate a thermal gradient of 0.056°C/m.

Results from the gas permeameter at Site 1176 are slightly different from those from other sites in that the range is even greater and there is no general decrease with depth. Throughout the hole the hemipelagic clays show greater scatter than elsewhere and in the upper half of the section (above 200 mbsf), sands, gravels, and especially ashes gave much higher values. In the lower half of the hole sands and gravels give high values, even at the bottom of the hole.

This site provided information regarding the nature of accreted sediments that compose the large thrust slice zone including the slope-basin transition. Coarse clastic sediments of Outer Zone origin, perhaps transported through a transverse canyon, are the dominant lithology of the accreted sediments. The accreted section of this zone is, thus, very different from the axially transported , volcaniclastic-rich trench sediments at Sites 1173, 1174, and 808. The age of the prism is probably younger than 2 Ma, and slope-basin development initiated <1 Ma, suggesting extraordinarily rapid growth of the prism. Although inconclusive because of the unconsolidated and coarse-grained nature of the sediments, the Cl anomaly encountered may indicate a deep fluid source.

Site 1177 Summary

The science objective of Site 1177 is to study the stratigraphic, geochemical, and physical properties framework of a reference site along the Ashizuri Transect (Fig. 10). This transect includes Sites 297, 298, 582, and 583.

We recognized five lithostratigraphic units at Site 1177 (Figs. 8A, 26). Unit I (upper Shikoku Basin facies) is Pliocene in age (300.20 to 401.76 mbsf) and consists mainly of weakly indurated hemipelagic mud interbedded with fresh volcanic ash. Unit II (lower Shikoku hemipelagic facies) is late Miocene in age (401.76 to 449.30 mbsf) and is composed almost entirely of a more strongly indurated hemipelagic mudstone. Unit III (lower Shikoku turbidite facies) is early to late Miocene in age (449.30 to 748.35 mbsf) and consists of turbidite sand, silty sand, gravel, mudstone-clast conglomerate, and hemipelagic mudstone, plus a few thin layers of carbonate-cemented claystone and siliceous claystone. There are four sand-rich packets within this facies,

and most of the siliciclastic sands contain abundant woody plant fragments (Fig. 27). Sediment dispersal evidently occurred through a broad system of coalescing submarine fans. Unit IV (volcaniclastic-rich facies) is early Miocene in age (748.35 to 831.08 mbsf). This unit consists of variegated mudstone to claystone, volcanic ash (Fig. 28), and silt turbidites with both volcaniclastic and siliciclastic compositions. Unit V is basaltic basement (831.08 to 832.13 mbsf) and is probably early Miocene in age. The basalt contains one pillow structure, and an intrusive contact with overlying sediment is highly altered(Fig. 29).

Deformation structures at this site, oceanward of the prism, are very sparse, more so than the reference sites at the Muroto Transect. This near absence at Site 1177 of structures and bedding dips >10° may result from slower rates of sedimentation, slight differences in lithology, or differences in topography of the substrate. Early soft-sedimentary structures are present between 748 and 831 mbsf; the main tectonic structure is a faulted and diagenetically altered interval between 579.45 and 581.10 mbsf. The basalt at the bottom of Hole 1177A, at 831 mbsf, exhibits glassy rinds at its contact with the overlying sediment and networks of veins bearing calcite and/or chlorite in complex interrelationships.

Biostratigraphic age control was provided by calcareous nannofossils, although their abundance and states of preservation were generally poor throughout the sequence; major intervals are barren of nannofossils. A total of 11 biostratigraphic events were identified. The continuous sedimentary section spans the time interval from the Pliocene (Zone NN18) through the early Miocene (Zone NN2). The biostratigraphic age estimates indicate an average sedimentation rate for the late Pliocene of 87 m/m.y. and a lower sedimentation rate of 28.7 m/m.y. for the lower Miocene to Pliocene sediments.

Magnetic inclination data of Hole 1177A after AF demagnetization at 30 mT were useful for interpretation of geomagnetic polarity changes from early the Miocene to Pleistocene. The Brunhes/Matuyama boundary is expected to occur above the initial coring depth of 300 mbsf. The Reunion Event (2.14 Ma) during the Matuyama Chron is interpreted to occur at 301.85 mbsf. The Matuyama/Gauss (2.581 Ma) and Gauss/Gilbert (3.58 Ma) boundaries are interpreted to occur at 328.55 and 384.25 mbsf, respectively. The beginning of Chron C3A (5.894 Ma) is identified to occur at 427.45 mbsf.

Sharp chemical discontinuities between and within lithostratigraphic units, particularly intense in the Cl, Na, K, sulfate, and alkalinity concentrations, and a high-sulfate turbidite unit in the middle half of the section are outstanding characteristics of Site 1177 pore fluid concentration-depth profiles. Discontinuities within lithostratigraphic units are unique for this site and were not observed at Sites 1173, 1174, or 808.The chemical discontinuities correspond with discontinuity boundaries in physical properties, suggesting that specific sediment intervals are and have remained for some time closed systems with respect to vertical diffusion. The chemistry within individual intervals reflects the concentrations at the time of “trapping” plus the in situ fluid-rock reactions since. The most conspicuous “sealed-off” interval was identified close to the bottom of the sediment section (775–805 mbsf) by its distinctly higher porosities, ~60%, relative to the sediments above and below having only ~40% porosity. The sharpest

discontinuity occurs at ~410 mbsf, the depth of the incipient décollement, at the boundary between lithostratigraphic Units I and II. As yet it is unclear what sediment type is acting as a cap rock. Preliminary observations based on local Cl anomalies at the boundaries of the deep, high porosity suggest that thin clay-rich horizons, probably smectite rich and having high horizontal/vertical anisotropy and extremely low permeability, may be responsible for sealing off sediment packets. The concentration-depth profiles are therefore only continuous in Units I and II but show unusual variance in Units III and IV.

Within Unit III there is a general decrease in Cl concentration; the minimum value is ~7% fresher than modern seawater concentration. This freshening, probably not caused by fluid flow, is most plausibly produced by smectite dehydration enhanced by Cl uptake by an authigenic hydrous silicate. To a lesser extent Na and K profiles show similar trends. Sulfate reduction is complete in Units I and IV, driven by microbial activity. But in between, in Unit III, sulfate concentration is high, ~86% of the modern seawater value, indicating that since burial little microbial activity has occurred. This is probably the result of the very low content of nonwoody, labile organic matter available for microbial activity in the turbidites. Most of the labile organic matter was microbially oxidized when the turbidites were at or close to the seafloor and sulfate diffused into this low sedimentation rate section.

The important diagenetic reactions are ash alteration, particularly reflected in the Ca, Na, and K profiles; carbonate formation as reflected in the Ca and alkalinity profiles; and opal-A dissolution as reflected in the Si profile.

The total organic carbon contents ranged from 0.03 to 1.62 wt%, with an average value of 0.45 wt%. The highest carbon values were measured in the Shikoku turbidite facies sediments (Unit III), which contained a terrestrial component characterized by plant detritus and pieces of wood. The sulfur content ranged from 0 to 0.81 wt%, with the highest concentrations occurring between 400–520 mbsf and 650–770 mbsf. The C/N ratios indicated that a mixture of both marine and terrigenous sources were contributing to the overall sediment composition. Unlike Sites 1175 and 1176, the inorganic carbon (~0.78 wt%) and carbonate contents (~2.7 wt%) were low with the exception of some thin-bedded carbonate-cemented layers (up to 65 wt%) in the Shikoku turbidite facies (Unit III).

Methane concentrations in sediments below the sulfate reduction zone (~4.5 m down to 734 mbsf) are consistent with a bacterial origin. The $C_1/(C_1+C_2)$ ratio for hydrocarbons in sediments below 750 mbsf plot within the mixing zone, suggesting that more than one source of hydrocarbons may be present.

Microorganisms were enumerated in 23 samples collected from 300 to 830 mbsf. Bacteria are present in all but two samples (687 and 830 mbsf) at abundances that are generally lower than expected based on results from previous ODP sites. A small, but statistically significant increase in bacterial populations occurs from 380 to ~740 mbsf that correlates with elevated sulfate concentrations in the interstitial water between these depths. The continued presence of sulfate is unexpected when bacteria are present at ~10^6 cells/cm^3, and this may be related to very low organic carbon concentrations in the sediment preventing significant amounts of bacterial

sulfate reduction. A total of 21 whole-round cores were taken for shipboard enrichment cultures, cell viability, and shore-based microbiological analysis to measure potential bacterial activities, culture microorganisms, characterize nucleic acids, and investigate fatty acid biomarkers.

Variations in physical properties at Site 1177 correlate well with the lithostratigraphic units. Units I and II are both characterized by low scatter in porosity. Unit I maintains a nearly constant porosity of 60%–65%. At the top of Unit II (402 mbsf), porosities begin to decrease rapidly with depth, decreasing to 45%–53% by 450 mbsf. Unit III is characterized by a gradual decrease in porosity with depth and by increased scatter that may be due to lithologic variations in this turbidite-rich sequence. Unit IV exhibits significant scatter and shows no clear trend with depth. An excursion to lower porosity (~40%) at 475–510 mbsf within Unit III occurs in a sandy section. Anomalously high porosity (~8%–15% higher than in surrounding sediments) within Unit IV occurs in a 30-m-thick zone between 765 and 795 mbsf. Low vertical *P*-wave velocities and formation factors also characterize this zone.

Most gas permeameter determinations at Site 1177 range around the values given by the background hemipelagites. Carbonate-cemented claystones at 540 and 591 mbsf give slightly higher values, as do the altered ashes of Unit IV, but the increase is small. The upper sands in Unit III account for all the high measurements at the site. Numerous wood-bearing silty sands were measured in the lower part of Unit III, but most give identical results to the background hemipelagites, suggesting blockage of the pore connections, perhaps by smectite.

In addition to serving as the reference site for the Ashizuri Transect, Site 1177 provides a comparison to the Muroto reference site (Site 1173). Comparison of the two sites will aid our understanding of the evolution of the Nankai Trough accretionary prism in two different geologic settings characterized by differing angles of prism taper.

Site 1178 Summary

The science objective of Site 1178 includes sampling of slope sediments and underlying LDRZ (Fig. 11) in order to clarify the structural evolution of the prism.

We recognized two fundamental lithostratigraphic units at Site 1178 (Figs. 8B, 30). Both are divided into three subunits. Interpretations of the lithostratigraphy are hampered by uncertainties regarding stratigraphic ages. Subunit IA (upper slope–apron facies) is Quaternary to Pliocene(?) in age and extends from the seafloor to a depth of 94.40 mbsf. Lithologies consist of hemipelagic mud, sandy mud, and volcanic ash. Subunit IB is Pliocene(?) in age and extends from 94.40 mbsf to 127.00. In addition to the normal hemipelagic mud, this subunit also contains abundant silt-sand turbidites, and minor mud-supported gravel. Subunit IC is early Pliocene(?) in age and extends from 127.00 mbsf to 199.20 mbsf. Lithologies in Subunit IC consist of hemipelagic mud with variable amounts of intermixed sand, rare volcanic ash beds, and rare mixed volcanic lapilli and gravel-sized mud clasts. Strata within Unit I have been subjected to significant amounts of displacement along a submarine slide surface. Below the dislocation surface, more highly deformed strata of Unit II are late Miocene to early Pliocene in age and almost certainly part of the Nankai accretionary prism. Subunit IIA (411.00–199.20

mbsf) contains abundant sand and silt turbidites. Similarities are striking between their lithofacies associations and those of the axial trench–wedge environment. Subunit IIB (411.00–563.95 mbsf) contains sporadic silt to sandy silt turbidites and a greater proportion of mudstone, similar in all respects to the outer trench–wedge facies at Sites 1173 and 1174. The axial trench–wedge facies is repeated below 563.95 mbsf (Subunit IIc) and extends to the bottom of Hole 1178B. This repetition of facies confirms the occurrence of one of the imbricate thrust faults within the accretionary prism.

Structurally, Site 1178 consists of four domains. Domain I, 0 to 200 mbsf, comprises the slope sediments, with discrete slump-folded packages and east-west-striking bedding. Domain II, from 200 to 400 mbsf, consists of accreted sediments but with only small-scale deformation features and gentle to moderate bedding dips. Domain III, in contrast, extends from 400 to 506 mbsf and is characterized by marked deformation throughout (Figs. 31, 32, 33). The deformation has four chief elements: bedding dips ranging up to 55°; bedding-oblique foliation; bedding-parallel fissility (Fig. 31); and fracture sets that brecciate the sediment into roughly trapezoidal fragments and postdate the foliation/fissility. Toward the base of this 106-m zone of shearing, scaly surfaces with downdip slickenlines probably indicate a major prism thrust fault. Domain IV, from 506 to the base of the hole, is characterized by generally weaker deformation, although moderate bedding dips are common. Steeper dips and increased deformation around 550 mbsf and between 633 and 645 mbsf presumably represent additional minor thrust faults. Thus Domain IV contains two minor thrusts and three thrust slices, each internally deformed much less than the sheet overlying the major thrust at the base of Domain III.

Biostratigraphic age control was provided by calcareous nannofossils although their abundance and states of preservation varied throughout the sequence. The interval from 199.05 to 673.17 mbsf yields assemblages especially poor in preservation and low in abundance, making zonal identification problematic. Deformation of the sediments leads to a repetition of biostratigraphic events and this to a disturbed biostratigraphic secession. The sedimentary section spans the time interval from the late Miocene (Subzone NN11a) through the Pleistocene.

Paleomagnetic measurements of magnetic inclination and intensity in Holes 1178A and 1178B show the existence of four age gaps from the top of Hole 1178A to the bottom of Hole 1178B. Based on the results of biostratigraphy, inclination changes from the top to the bottom of Holes 1178A and 1178B are identified as four different geomagnetic polarity periods. Normal polarity is identified from 0 to 8.5 mbsf in Hole 1178A within the Brunhes Chron (0–0.78 Ma). Inclination changes from 8.5 to 209.75 mbsf are considered to be geomagnetic polarity changes from late Pliocene to Miocene, including the Gauss (2.581–3.580 Ma), Gilbert (3.580–5.894 Ma), and C3A (5.894–6.935 Ma) Chrons. The polarity changes from 209.75 to ~400 mbsf are also identified as the same geomagnetic polarity changes from late Miocene–Pliocene. Continuous steep inclinations below 400 mbsf may be considered to be a repeat of the C4r Subchron (8.072–8.699 Ma).

The Cl concentration-depth profile exhibits a steep, continuous trend of freshening of up to 3%–4% relative to seawater Cl concentration. Superimposed on this background dilution profile

are numerous smaller Cl minima. The largest one is at ~200 mbsf, corresponding to >6% dilution and above the BSR at ~400 mbsf, which corresponds to ~7% dilution. Based on measured core temperatures on the catwalk, –0.5°C at the 200 m minimum, the associated elevated methane concentration, and the observation that other dissolved components, such as Si and Ca, have similar dilution minima, disseminated methane hydrate is widespread at this site, increasing in abundance from ~90 mbsf to the depth of the BSR. Hydrate is not evenly distributed within the sediment and seems more abundant in coarser grained horizons. Some indications of a paleo-BSR situated at ~100 m below the present BSR are observed.

The Ca, Mg, alkalinity, and sulfate concentration profiles are intimately coupled in the top 35 mbsf, with primary dolomite formation and dolomitization of biogenic calcite the most active reactions. The inverse relation between Ca and Mg below this depth suggests that they are involved in distinct reactions—Mg in silicate reactions below the depth drilled, and Ca in ash dissolution and alteration plus probably carbonate reactions linked or associated with microbially mediated reactions at the BSR

Similar to the deep-water Sites 1173 and 1174 but unlike the shallow water Sites 1175 and 1176, an increase in Cl concentration with depth in the top 35 mbsf is a trend consistent with diffusion of lower chlorinity interglacial water into the sediment.

The TOC content for the sediment samples examined at Site 1178 ranges from 0.57 to 1.03 wt% over the first 383.6 mbsf, with an average value of 0.73 wt%, the highest TOC values measured for Nankai sediments during Leg 190. Sulfur concentrations track the TOC values in this interval and range from 0.24 to 1.45, wt% with the highest values occurring at 200 and 350 mbsf coincident with the highest TOC values. The moderate to low concentrations of methane throughout Holes 1178A and 1178B are attributed to the high concentrations of light hydrocarbons from ethane (C_2) to hexane (C_6), indicative of older, more mature organic matter within the sediments (diagenesis) or migration (thermogenesis) of hydrocarbons from deeper depths. Overall, the concentrations of light hydrocarbon ethane to hexane reflect the thermal evolution and maturity of the sedimentary organic matter at Site 1178. The Bernard ($C_1/[C_2+C_3]$) ratio for the hydrocarbons at Site 1178 also indicate that some contribution of the lighter hydrocarbons (ethane to hexane) in these sediments were produced from more mature organic matter present in situ mixed with thermogenic hydrocarbons that have migrated in from a more mature source at depth. Significant faulting has occurred over the lower 300 m of Hole 1178B that would facilitate fluid migration of more mature hydrocarbons buried at deeper depths to shallower sediments.

Microorganisms were enumerated in 30 samples collected from the surface to 633 mbsf at Site 1178. Bacteria are present in near-surface sediments at low, but close to expected abundances. This was probably related to high IW sulfate concentrations to at least 18.3 mbsf. However, bacterial populations decline rapidly to barely detectable at 272 mbsf. This is a much greater rate of decrease than was observed at other sites during this leg. A small but statistically significant decrease from the general trend that is associated with the presence of a small amount of gas hydrate occurs at 210 mbsf. Below 272 mbsf, population sizes generally

vary between not detectable and barely detectable, except for a zone between 374 and 497 mbsf, where populations increased up to a maximum of 6×10^5 cells/cm^3. These were not only locally statistically significant but were larger populations than were encountered at some of the more shallow depths at this site. No relationship was observed between bacterial populations and either the IW sulfate concentration or the methane concentration; therefore, the reasons for such a rapid rate of decrease in numbers remains unclear. Seventeen whole-round cores were taken for shipboard enrichment cultures, cell viability, and shore-based microbiological analysis to measure potential bacterial activities, culture microorganisms, characterize nucleic acids, and investigate fatty acid biomarkers.

There are no obvious differences in physical properties between the slope-apron deposits of Unit I and the underlying accreted sediments of Unit II. In general, porosities at Site 1178 decrease with depth, following a typical compaction profile. Deviations from the compaction trend occur at 70–100 mbsf, 140–160 mbsf, and ~200 mbsf. In addition, porosity values within lithostratigraphic Subunits IB and IC are more scattered than in Subunit IA and Unit II, and they probably reflect lithologic variation in this sandier part of the stratigraphic section or deposition by slope-failure processes. Velocities and formation factors increase with depth and are highly variable.

Two in situ temperature measurements indicate a thermal gradient of 0.046°C/m.
Site 1178 drilling revealed that the LDRZ is composed of steeply dipping, pervasively foliated, and partly brecciated upper Miocene accreted sediments. This result will contribute significantly to our understanding of tectonic evolution of the Nankai accretionary prism.

SUMMARY OF SCIENTIFIC RESULTS

Stratigraphic Framework of Incoming Sediments

Results from Leg 190 help define several important spatial and temporal differences in the stratigraphy of the Shikoku Basin. These stratigraphic variations in turn influence patterns of deformation within the Nankai Subduction System. Beginning at the stratigraphic base, a volcaniclastic-rich facies overlies basalt basement at Site 1177 (Ashizuri Transect; Figs. 8A, 10). This facies differs from basal strata at Sites 808 and 1173 (Muroto Transect) in two important ways. First, the oldest strata at Site 1177 are early Miocene in age, rather than middle Miocene, and second, they contain considerable amounts of siliciclastic silt and sand in addition to volcanic sand and ash. The lower Miocene siliciclastic and volcaniclastic beds probably were eroded from the Japan Island arc and the Kyushu-Palau remnant arc. The age variation in basal sediment from west to east can be explained by proximity to the axis of the spreading ridge of Shikoku Basin. The ridge was active between 26 and 15 Ma, and seamount eruptions along the Kinan chain may have continued to 13–12 Ma. Temporal correlation of the Miocene ash beds remains uncertain. Given the existing biostratigraphic resolution, volcaniclastic beds along the

Ashizuri Transect appear to be older than the thick rhyolitic tuff deposits that were cored at Site 808, so they may have been erupted from a different source.

Cores from Site 1177 include a package of lower(?) to upper Miocene siliciclastic turbidites with abundant woody organic matter. Deposition of correlative turbidites at DSDP Site 297 also began during the Miocene but continued into the Pliocene. The Miocene turbidites at Site 1177 were derived from a relatively large land mass, most likely southern Japan, and the dispersal system spread terrigenous sediment over a broad area of Shikoku Basin. During that same time interval, the seaward part of the Muroto Transect area sat above the basement high formed by the Kinan Seamounts. Higher seafloor relief evidently prevented the upslope deposition of turbidites.

Fine-grained hemipelagic deposits of Shikoku Basin display an unexpected characteristic of unusually high magnetic susceptibility. Magnetic susceptibility increases even within mudstone intervals between the Miocene turbidite packets at Site 1177. The mineralogic cause of this magnetic response in Shikoku Basin strata remains unknown.

A facies change from the lower to upper Shikoku Basin is defined at all sites by the absence to presence of ash beds containing recognizable volcanic glass shards. Most of the Pliocene volcanic ash beds probably were derived from the Honshu-Kyushu arc. Particle size, chemical composition, temperature, depth of burial, and time affect ash alteration and preservation. Thus, this unit boundary is time transgressive and sensitive to regional and temporal changes in the margin's thermal structure.

Shikoku Basin strata experienced diachronous burial during the Pliocene and Quaternary beneath an upward-coarsening and upward-thickening wedge of trench turbidites. The Nankai Trench wedge is thinner in the Muroto Transect area (above the basement high), but individual turbidites tend to be thinner and finer grained toward the southwest (DSDP Site 582). Quaternary sedimentation rates at Sites 1173 and 1174 were 600 and 760 m/m.y., respectively, more than one order of magnitude higher than the rate for Miocene turbidites at Site 1177 (35.5 m/m.y.). The main reasons for the higher rates of trench sedimentation include erosion from rapidly uplifting volcanic and metasedimentary terranes in the Honshu-Izu collision zone of central Japan and confinement of most sediment gravity flows to an axial dispersal system.

Evolution of the Accretionary Prism

Sites 1175, 1176 and 1178 are among a handful of DSDP and ODP sites to have penetrated completely through slope sediments into an underlying accretionary prism (Figs. 8B, 11). They are, therefore, important for refining models of trench-slope evolution. The upper facies unit at all three sites fits into conceptual models of a trench-slope basin or slope apron, at least for cases where there is isolation from influx of coarse terrigenous sediment. Resedimentation of muddy material by submarine slumps and mudflows, perhaps triggered by seismogenic activity, contributed to high rates of sedimentation (200–3000 m/m.y.).

One of the unexpected discoveries of Leg 190 is the lack of change in sediment composition or lithofacies across the interpreted contact between trench-slope basin and accretionary prism,

as deduced from seismic reflection data. Strata throughout the slope to prism transition at Sites 1175 and 1176 include abundant sand turbidites and muddy gravel. One way to explain this paradox would be through frontal offscraping of a trench fan that had been fed by a transverse sediment conduit (e.g., throughgoing submarine canyon). Evidently, coarse siliciclastic material was diverted away from the slope basin relatively early in its development, as canyons were rerouted upslope by uplift and tilting of the prism. This change in the sediment-dispersal network resulted in an overall upward-thinning and upward-fining megasequence within the slope basin. Regardless of the ambiguity in the exact position of its basal unconformity, the slope basin at Sites 1175 and 1176 must have developed within the last 2 m.y. This time constraint means that a phenomenal 40-km-wide accretionary prism has been added to the Nankai margin over that same time period.

Interpretations of results from Site 1178 are even more problematic because of inconclusive biostratigraphic control. One option is to place the fundamental lithotectonic boundary between a mud-dominated slope apron and sandy accretionary prism at a major facies break (~200 mbsf). If this interpretation is correct, then the contact is probably a slump surface. The underlying prism strata probably were accreted during the late Miocene to early Pliocene, prior to the frontal accretion at Sites 1175 and 1176. Even though the timing of accretion remains uncertain, it is clear that strata below 200 mbsf display many effects of intense deformation (e.g., fractures, incipient cleavage, and steeply dipping beds). Their facies character also matches that of the axial trench wedge and outer trench wedge, and there is good sedimentologic evidence for thrust repetition of the axial trench–wedge facies with slices at 199–411 mbsf and below 564 mbsf. These distinguishing features of both sedimentology and structural geology have important implications for interpretation of kindred rock units in such ancient subduction complexes as the Shimanto Belt of southwest Japan.

Chronostratigraphic Synthesis

Detailed bio- and magnetostratigraphic records were obtained at all sites facilitating correlation among sites. Paleomagnetic results for Site 1173 and 1174 show clear geomagnetic changes from the middle Miocene to Pleistocene (Fig. 34) and can be correlated to the polarity changes at Site 808. The basal age of the trench-wedge turbidites including the transition zone to the upper Shikoku Basin facies is estimated to be ~0.8 Ma. The boundary between the Upper and lower Shikoku Basin at Sites 1173 and 1174 is interpreted to be 3–5 Ma. The age of the décollement zone at Site 1174 is estimated to be from 5.894 Ma (beginning of C3A Chron) to 6.935 Ma (termination of C3B Chron, which corresponds with the age of décollement zone at Site 808). At Site 1177 located in the Ashizuri Transect, the lower Shikoku Basin facies extends from the Pliocene Miocene, although it is difficult to identify the geomagnetic records because of poor core recovery (Fig. 34). Because Site 1177 was drilled without coring to 300.2 mbsf, correlationscould not be made between Site 1177 and Site 582.

Pleistocene to Pliocene paleomagnetic data are similar at Sites 1175 and 1176 and document a few geomagnetic excursions within the Brunhes Chron.

At Sites 1173, 1174, 1177, and 808, the trench-wedge turbidites and the Shikoku Basin show contrasting sedimentation rates in the age-depth plots (Fig. 35). The sedimentation rates of the trench turbidites within the transition zone of each site shows high values with the highest at Site 808 (204 m/m.y. at Site 1173; 698 m/m.y. at Site 1174; and 842 m/m.y. at Site 808). In contrast, sedimentation rates are slower in the upper and lower Shikoku Basin facies. Rates for the upper Shikoku Basin facies are 77.82 m/m.y. at Site 1173, 78.46 m/m.y. at Site 1174, and 81.62 m/m.y. at Site 808. The sedimentation rate of the upper Shikoku Basin facies at Site 1177, however, is lower (40.37 m/m.y.). Sedimentation rates for the lower Shikoku Basin facies are lower than those of the upper Shikoku Basin facies. The lower Shikoku Basin facies rates are 27.40 m/m.y. at Site 1173, 35.22 m/m.y. at Site 1174, 28.27 m/m.y. at Site 1177, and 31.67 m/m.y. at Site 808.

Magnetic susceptibilities proved a valuable tool for correlation among sites (Fig. 8A) and help constrain the correlation of the décollement and incipient décollement horizons at Sites 1173, 1174, 808, and 1177.

Development of the Décollement Zone, Muroto Transect

Leg 190 completed a transect of the basal décollement of the Nankai accretionary prism from an undeformed state at Site 1173 to the well-developed detachment fault landward of the deformation front documented at Sites 1174 and 808 (Fig. 36).

At Site 1173, there is little structural or physical properties evidence for a proto-décollement zone, i.e., incipient deformation indicative of a detachment fault. The stratigraphic equivalent to the Site 1174 décollement interval indicated in Figure 36 is based on correlation of core magnetic susceptibility (Fig. 8). This interval is part of a thicker domain of elevated bedding dip, but shows no localized increase in observed deformation. However, a marked downhole decrease in *P*-wave velocity and a slight porosity increase at the top of the interval (~389 mbsf) suggest that a subtle mechanical strength discontinuity could contribute to the localization of the décollement in this interval. Pore fluid chlorinity also shows a small low-chloride excursion above this interval and an abrupt transition to higher values at ~390 mbsf; however, there is not a clearly corresponding feature in the Sites 1174 or 808 chlorinity data. It is unknown, of course, whether in the future the décollement actually will propagate along this particular stratigraphic horizon to the position of Site 1173.

The hallmark of the décollement zone at Sites 808 and 1174 is intense brittle deformation, manifested as finely spaced fracturing that breaks the mudstone into millimeter- to centimeter-scale fragments (Fig. 19). The fragments have polished and slickenlined surfaces, showing complex and heterogeneous slip directions, but they do not exhibit obvious internal deformational structures at the core scale. At Site 1174, the upper limit of the décollement zone is marked by a sharp increase in the intensity of brecciation, although the lowermost prism section above exhibits distributed fracturing as well. Within the décollement zone, there is a

downward increase in intensity of the brecciation, peaking in a 7-m-thick zone of fine comminution of the mudstone just above the very sharp base of the décollement zone (Fig. 20). Within the fault zone, there are several intervals, up to tens of centimeters thick, of unbroken mudstone, which are interpreted as intact blocks in a multistranded shear zone.

It is remarkable that the décollement zone at Site 1174 appears to be at least equally well developed as it is at Site 808. It is thicker at Site 1174 than it is at Site 808 (32.6 vs. 19.2 m thick, respectively). It is also brecciated to a finer scale, despite the more landward—thus presumably more structurally evolved—position of Site 808. Differences in the observed structures could be explained by differences in core recovery; however, the greater thickness at Site 1174 could not. Notable at both sites is the complete absence of veins, alteration zones, or other evidence of past fluid-rock interaction specific to the décollement.

The development of the décollement and the strain discontinuity across it are clearly exhibited in the core physical properties data. At Site 1174, there is a sharp porosity increase and *P*-wave velocity decrease right at the base of the structurally defined décollement. These same features are even more pronounced at Site 808, and both Sites 808 and 1174 exhibit evidence of a porosity minimum within the décollement. At both sites, however, the most prominent feature is the discontinuity across the base of the zone crossing into the underthrust section. This discontinuity is likely due to a combination of undercompaction of the rapidly loaded underthrust section (e.g., Saffer et al., 2000) and enhanced tectonic compaction of the prism and décollement caused by the imposition of lateral tectonic stress (Morgan and Karig, 1995).

In summary, the décollement beneath the toe of the Nankai accretionary prism develops from an unremarkable and homogeneous interval of hemipelagic mudstone into a 20- to 32-m-thick zone of strong brittle deformation, the base of which marks a boundary between the distinct physical/mechanical regimes of the prism and the underthrust section. The two drilling penetrations of the fault zone suggest an anastomosing system of discrete brittle shears, reminiscent of faults observed in mudrocks on land. Despite a major effort to detect fault-channeled fluid flow, there is no evidence that a chemically distinct fluid is being channeled in the décollement zone along the transect defined by these three sites.

Correlation of the décollement horizon between Muroto and Ashizuri Transects imposes an intriguing question on the localization of the décollement in the lower Shikoku Basin mudstone. Although DSDP/ODP drilling has not penetrated the décollement at the Ashizuri Transect, a clear and continuous seismic reflector allows us to correlate the décollement horizon at the toe region to Site 1177 (Fig. 37). At Site 1177 this reflector is at 420 mbsf and coincides with the identical horizon of the décollement of the Muroto Transect based on chronological and magnetic susceptibility correlations. It raises an important question as to why the décollement stays at the same stratigraphic horizon despite the fact that there is a major difference in the thickness of turbidites and the lithology and diagenesis of the Shikoku Basin sediments between the two transects. This question should be challenged by further shore-based study.

Geochemical Gradients, Muroto Transect

The shipboard geochemical data provide insight on the origin of fluids and the depth intervals and paths of recent flow. Sediment composition, physical properties, and both fluid chemistry and flow are associated. In addition, abiogenic and microbially mediated diagenetic reactions that have modified fluid composition have been characterized and quantified.

The most interesting and pronounced feature of the pore fluid concentration-depth profiles in the Muroto Transect from Site 1173 through Site 1174 to Site 808 is the ~350-m-broad low-Cl zone situated in the lower Shikoku Basin unit (Fig. 38). It has a clear concentration minimum ~140 m below the décollement. At Sites 1173 and 1174, this low-Cl zone decreases in intensity gradually upsection to the sediments overlying the upper Shikoku Basin facies. If the profile is considered a one-dimensional diffusive profile, its length suggests that this prominent feature has developed within the first ~250 k.y. after burial of the Shikoku Basin sediment by the trench-wedge sediment. Additionally, the extent of Cl dilution relative to seawater Cl concentration systematically differs among the sites; it has evolved from 8%–9% at reference Site 1173 to 16%–17% at intermediate Site 1174 to 20%–21% at adjacent (<2 km) Site 808. Based on the very low smectite content of this sediment section, most of the freshening may not be due to local smectite dehydration but may result from horizontal transport. Note, however, that the original smectite concentration is not known. Some of the low-Cl concentrations most likely reflect the uptake of Cl by deep-seated hydrous silicate reactions; for example, serpentine, chlorite, talc, or amphibole incorporate considerable amounts of Cl in their structure. These reactions occur at temperatures of >250° or 300° to ~450°C, typical of the modeled temperatures at downdips of seismogenic zones (~350°C at Western Nankai). Thus, the broad low-Cl zone most probably carries a mixed signal of dilution via clay dehydration reactions plus Cl uptake by high-temperature reactions at the seismogenic zone. The relative contributions of these two processes can be resolved by shore-based Cl, Br, and F concentration and isotope analyses.

The slightly higher Cl concentration within the décollement zone, observed at Sites 1174 and 808, may simply result from subtle differences in physical properties within and outside the décollement.

Other potential fluid flow horizons characterized by sharp changes in downnhole geochemical profile are

1. At Sites 1173, 1174, and 808, the boundary between the trench-wedge and upper Shikoku Basin sediments. The rather sharp reversal of the Cl gradient at this boundary may be maintained by flow of a slightly more saline fluid than seawater or by in situ hydration reactions that are faster than diffusion.

2. Along the protothrust (~470 mbsf) at Site 1174, as particularly indicated by the Cl, Na, Ca, and K concentration profiles.

3. At Site 1176, the Cl, Na, Ca, and K concentration profiles suggest communication with a deep fluid source, most likely associated with the out-of-sequence thrust.

It is interesting to note that the chemical characteristics of the protothrust and the deep source associated with the out-of-sequence thrust fluids are similar to the characteristics of the fluid in the low-Cl zone centered below the décollement. The composition of the fluid along the trench wedge/Shikoku Basin boundary is, however, distinct.

Another distinct characteristic of the Muroto Nankai Transect, not observed at any of the other drilled DSDP and ODP subduction zone sites, is the elevated (up to 10 mM) dissolved sulfate zone found at depth. It is beneath the near surface sulfate reduction zone, and prevails from the boundary between the upper and lower Shikoku Basin facies to oceanic basement and probably deeper. The fact that microbial activity has not reduced it over the past 0.5 m.y. indicates that the amount of labile organic matter available for microbial activity (for sulfate reducers and/or methane oxidizers) above the proto-décollement and décollement zones, where temperatures do not limit bacterial activity, is extremely low. Thus, much of the dissolved sulfate may persist into the seismogenic zone; it can only get reduced inorganically at least at 250°–300°C. The presence of dissolved sulfate in an anaerobic environment effects the oxidation state of the system and should influence sediment magnetic properties as well as inorganic reactions with transition metals, such as Fe and Mn.

The dominant diagenetic processes are ash alteration to clays and zeolites and silicate (mostly clay) reactions at the deep water sites and carbonate reactions at the shallow water sites; carbonate diagenesis, however, also occurs at the deep water sites. Opal-A dissolution controls the Si concentration profiles at each of the sites in the top few hundreds of meters, and other silicate reactions control it deeper in the sections.

Gas Hydrates

Although no solid gas hydrate was recovered during Leg 190, their presence was documented indirectly. Both temperature measurements of cores on the catwalk and pore fluid Cl concentrations indicate the existence of gas hydrates at two slope sites, Site 1176 and Site 1178. Gas hydrate dissociates upon recovery because it is unstable at ambient temperature and pressure. Recovery of solid hydrate is unlikely unless it is extremely abundant.

Sites 1176 and 1178 are within the stability field of seawater-methane hydrate from the seafloor to the BSR. Because methane is the dominant gas in the sediments at these sites, if gas hydrate is present it should be primarily methane hydrate as it is at nonthermogenic oceanic sites. Formation of methane hydrate is a highly exothermic reaction; its decomposition consumes much heat and cools the cores. At Site 1176, colder than background temperatures, by 4°–5°, between ~220 and 240 mbsf, were measured in two cores (190-1176A-25X and 26X). Because of poor core recovery no data exist between 240 and 320 mbsf. Pore fluid Cl concentrations suggest minor dilution of Cl by ~1% beyond dilution by other processes.

At Site 1178, gas hydrate appears to be considerably more abundant. Based on pore fluid Cl concentrations, methane hydrate (inferred from gas composition) is present between ~120 and 400 mbsf, with the highest concentrations between 150 and 200 mbsf. At ~200 mbsf, in Core 190-1178A-23X, the lowest catwalk core temperature of –0.5°C was measured. Temperatures colder than background by 4°–6°C were measured in several cores, mostly between 150 and 200 mbsf.

At Site 1178, the Cl concentration-depth profile has a steep, continuous trend of freshening between 90 and 200 mbsf with two intense Cl minima. The first is between 170 and 185 mbsf. The second minimum with the lowest Cl value of 524 mM compared with that of bottom-water value of 557 mM was measured in Core 190-1178A-23X (the one with the –0.5°C catwalk temperature). This corresponds to >6% dilution by methane hydrate decomposition. The background dilution throughout the 150–200 mbsf interval is 3%. Between 200 and 400 mbsf, Cl concentrations continue to gradually decrease with depth from 545 mM to a minimum of 517 mM at the BSR depth (~420 mbsf), which corresponds with >7% dilution. Superimposed on the background Cl dilution profile are numerous smaller Cl minima. This suggests that throughout the section, from 90 to 400 mbsf, disseminated gas hydrate is present and is responsible for the background 3%–4% Cl dilution and that specific sediment horizons, probably the coarsest grained ones, have higher hydrate concentration, equivalent to 6%–7% Cl dilution.

Cl concentrations sharply decrease below the BSR depth and reach a minimum of 470 mM, almost a 6% dilution, centered around 500 mbsf. The origin of this low-Cl zone is as yet unclear. It may represent a more hydrate-rich young paleo-BSR, which has not had enough time to dissipate the dilution signal caused by dissociation of the hydrate. Consistent with this scenario, higher concentrations of methane are found at this depth. Sedimentation and/or tectonics could have caused such an upward migration of the BSR.

Changes in Physical Properties

Trench-Wedge Facies

The trench-wedge facies thickens substantially from the basin to the trench. This rapid sedimentation may affect the pore pressures and the state of compaction in the underlying sediment. Within the trench-wedge facies, porosities exhibit high scatter, probably because of lithologic variability. In general, porosities decrease with depth within this section at Sites 1173 and 1174 but show no distinct trend at Site 808. Some of the difference in the porosity trend may be attributed to offset along the frontal thrust at Site 808, which would disturb the pre-existing porosity profile.

Upper Shikoku Basin Facies

At Site 1177, the lowermost ~100 m of the upper Shikoku Basin facies exhibits nearly constant porosities of 60%–65%, whereas the velocities increase slightly with depth (Fig. 39). At Site 1173, porosities increase slightly with depth from 57%–65% at ~102 mbsf to 62%–69% at ~340 mbsf. These values are surprisingly high for a burial depth of 300–400 m, and the porosity

within the upper Shikoku Basin facies at both reference sites deviates significantly from normal compaction trends for silty clays. Velocities at Site 1173 remain relatively constant to ~240 mbsf and increase below this, despite the increasing porosity. This behavior suggests cementation. At Sites 808 and 1174, a slight porosity increase with depth is observed but is less distinct than at Site 1173. Porosities within the upper Shikoku Basin facies at Sites 1174 and 808 range from ~35% to 45%. The difference in porosity values between the reference sites and those in the deformed wedge imply that either compaction, collapse, and dewatering of the sediments has occurred during accretion, or the sites within the accretionary wedge have a different diagenetic and cementation history than the current reference sites. High-velocity layers occur near the top and bottom of the upper Shikoku Basin facies, which otherwise appears to be gradually increasing with depth.

Lower Shikoku Basin Facies

Along the Muroto Transect (Sites 1173, 1174, and 808), porosities within the lower Shikoku Basin facies decrease with depth and follow a normal compaction trend. At Site 1173, porosities within this unit decrease from ~50% at the top to ~36% at its base. At Sites 1174 and 808, porosities decrease from 34%–40% to 30%–35%, with a sharp offset to greater porosity across the décollement. At Site 1177, the lower Shikoku Basin facies includes a thick turbidite sequence that does not correlate with the stratigraphy observed along the Muroto Transect. Porosities within the upper hemipelagic portion of the lower Shikoku Basin facies at Site 1177 (400–449 mbsf) decrease with depth from 60%–65% to 46%–54%. The porosity decrease within the lower Shikoku Basin sequence from Site 1173 to Sites 1174 and 808 may be explained by compaction and dewatering of these sediments with progressive burial. Alternatively, the lower Shikoku Basin sediments at Sites 1174 and 808 may have initially had lower porosities than Site 1173 because of factors such as greater overburden or lithologic differences.

At both Sites 808 and 1174, porosities increase sharply across the décollement zone, whereas velocities decrease. This probably reflects a combination of (1) rapid, partially undrained burial of the underthrust sequence resulting in excess pore pressures and (2) higher mean stress and tectonic compaction of the accreted sediments. At Site 1174, porosities directly below the décollement zone are slightly lower than at Site 808. This observation suggests that simple progressive compaction of underthrust sediments may not adequately explain the porosity-depth trends and that other factors (such as initial sediment thickness) are also important. At Site 1173 the stratigraphic equivalent interval of the décollement zone (~420 mbsf) corresponds to the base of an anomalous zone in which velocities decrease with depth. A similar, considerably smaller amplitude velocity excursion correlates with the stratigraphic equivalent of the décollement at Site 1177 (~430 mbsf).

In accordance with the steadily decreasing porosities below the décollement zone, velocities generally increase with depth at Sites 808 and 1174. Horizontal velocities (V_x and V_y) increase more rapidly with depth below the décollement than vertical velocities (V_z). Increasing velocity anisotropy with depth suggests vertical compaction of the sediments.

Mass Accumulation Rates

Comparison of the thickness of lithostratigraphic units between sites appeared problematic because of the apparent diachronism of the lithostratigraphic boundaries and of the lateral changes of porosity. To help tackle this problem, computations of solid thickness were performed and are presented here. The solid thickness is computed by integrating the solid volume fraction (1 porosity) from the base of the sedimentary column using the moisture and density data. The solid thickness thus represents the thickness of the sediment after vertical compaction to 0 porosity. The solid thickness is preserved during vertical compaction but is increased by horizontal tectonic shortening, regardless of whether it occurs by ductile strain or by thrusting. Figure 40 shows the biostratigraphic and paleomagnetic ages at Sites 808, 1174, 1173, and 1177 as a function of the solid thickness. The derivative of these curves represents the solid mass accumulation rate.

The diachronism of the lithostratigraphic boundaries appears clearly on Figure 40. The upper/lower Shikoku Basin facies boundary moves between ~2.25 Ma at Site 1174 and ~3 Ma at Site 1173 to >4 Ma at Site 1177. The base of the trench wedge is younger at Site 1173 than at Sites 808 and 1174.

The solid thickness the sequence below the stratigraphic level of the décollement displays some lateral variability, which could be attributed to lateral variations of the solid accumulation rates during sedimentation. This variability is most important in the part of the basin older than 11 Ma. Accumulation rates obtained by linear regression on all age data between 7 and 11 Ma are very similar at all sites: 14.9 m/m.y. at Site 1173, 16 m/m.y. at Site 1174, 13.7 m/m.y. at Site 808, and 16.3 m/m.y. at Site 1177. The same remark may be done for the accumulation rates between 1.8 Ma (Pliocene/Pleistocene boundary) and 4 Ma: 29.7 m/yr at Site 808, 29.9 m/yr at Site 1174, 28 m/yr at Site 1173, and 22 m/yr (based on paleomagnetism) at Site 1177. In contrast with these two sequences, which do not show evidence for tectonic thickening within the precision of the age determinations, the interval immediately surrounding the décollement varies considerably in thickness. The solid thickness of the 4- to 7-Ma interval increases from ~15 m at Site 1173 to ~30 m at Site 1174, and to 35 m at Site 808. Note that the décollement varies in stratigraphic age by ~1 m.y. between Site 808 and Site 1174 but stays within the lower part of this thickened interval. Note that the décollement on the Ashizuri Transect also lies within the same age interval. It also appears that the frontal thrust throw (150 m of vertical throw, corresponding to 80 m of solid thickness where it was drilled) accounts well for the change of thickness of the trench wedge between Site 808 and Site 1174.

Organic Geochemistry and Hydrocarbon Sources

Multiple sources (biogenic, thermogenic, and catagenic) and production mechanisms for the hydrocarbons encountered during Leg 190 were identified by plotting the methane (C_1), Bernard ratios (C_1/C_2+C_3) and sulfate profiles for each Site (Fig. 41). At Reference Site 1173, the hydrocarbon profile is dominated by biogenic methane down to 260 mbsf, followed by a shift to a mixture of thermally produced methane and lighter hydrocarbons around 300 mbsf that

dominates the composition of gases down to 724 mbsf. The marked shift in hydrocarbon type is likely due to an increase in sulfate concentration below ~400 mbsf that inhibits biogenic production of methane. The hydrocarbons detected in sediments at Site 1174 are indicative of a biogenic source coupled with a thermogenic component down to the décollement (~807.6 mbsf), increasing in concentration with temperature and depth. Like Site 1173, as sulfate increases with depth, methane production decreases (low parts per million). The hydrocarbons below 807.6 mbsf are the products of both rapid thermal maturation of immature organic matter present in the sediments (thermogenic) and the thermal cracking of more mature organic matter or "kerogen" (catagenic).

Site 1175 is characterized by very young sediments and immature organic matter as observed by the production of biogenic methane throughout the hole. As at Site 1175, biogenic methane dominates the first 300 mbsf of Hole 1176A; however, over the last 100 m there is an abrupt shift into the thermogenic zone. Interestingly, the $C_1/(C_2+C_3)$ ratio indicates that no mixing has occurred; therefore, the hydrocarbons detected below 300 mbsf are a separate component. The very low thermal gradient at Site 1176 (~25°C at total depth; 401.6 mbsf), coupled with high sulfate concentrations and the predominance of C_2 over C_1 indicate that thermogenic hydrocarbons migrated into the lower 100 m of Hole 1177 from a deeper source rather than forming in situ (diagenesis) at low temperature. The hydrocarbon profile for Site 1177, drilled on the Ashizuri Transect, differs significantly from those sites drilled on the Muroto Transect, with low concentrations of methane between 304 and 363 mbsf followed by an abrupt drop in methane concentration (a few parts per million) over the next 270 m of hole. The low abundance of methane below 400 mbsf is the result of an unusually high sulfate content that is controlling methanogenesis or microbial mediation of methane production. The relatively low concentrations of organic matter available in these sediments may be preventing sulfate reducers from consuming the excess sulfate keeping concentrations at high levels. A sharp increase from the low parts per million level to ~1600 ppm was measured in the last 90 m to total depth at 830.3 m, coincident with the transition from the Shikoku turbidite facies (Unit III) to the volcaniclastic facies (Unit IV). As at Site 1176, there is an abrupt shift of the $C_1/(C_2+C_3)$ ratio to the mixing zone with both ethane (C_2) and biogenic methane occurring between 750 and 830 mbsf. The temperatures within the mixing zone at Site 1177 are in the range of thermogenic in situ production of the C_2 lighter hydrocarbons.

Microbial Activity and Biogeochemistry

Bacteria are responsible for shaping many of the chemical profiles within deep marine sediments through their metabolic activity. The distribution of the microbial community was characterized and their impact on deep marine sediments was investigated in cores from the Nankai Trough (Fig. 42). The apparent environmental controls on bacterial distribution varied among sites from physical (temperature) to geochemical. Overall, the total numbers of bacteria at these sites was either at the low end, or below the range predicted by a general model constructed from bacterial distributions in deep marine sediments at previous ODP sites (Parkes

et al. 1994). This is consistent with observations made at a previous accretionary prism site—Cascadia margin.

The abundance of bacteria at Site 1173 appears to be primarily controlled by a steep thermal gradient. The profile agrees with the model for the upper 250 m, with a significant increase in numbers between 43 and 80 mbsf associated with high concentrations of methane and total organic carbon. At 250 and 460 mbsf the temperature boundaries for mesophiles/thermophiles and thermophiles/hyperthermophiles, respectively, were crossed. At the upper boundary populations decreased overall, and at the second boundary there was a single significant increase at ~85°C. Bacteria were not observed in the five deeper, and warmer, samples at this site (536–673 mbsf). Overprinting this temperature control is a significant correlation between bacterial numbers and in situ methane concentration between the near surface below the sulfate reduction zone and ~400 mbsf. At 400 mbsf (~76°C), rising concentrations of both methane and sulfate suggest that bacteria are no longer controlling sediment geochemistry and that temperature effects dominate.

Bacterial abundance at Site 1174 falls within predicted values from the surface to ~370 mbsf, apart from two significant excursions in the upper layers associated with sandy cores. This site is also characterized by a steep temperature gradient, and at 370 mbsf estimated temperature is ~50°C. From this depth, bacterial populations rapidly decline to not detectable at 575 mbsf. Bacteria were not observed in the 15 samples collected from 623 to 1091 mbsf with the exception of two samples (779 and 796 mbsf) located just above the décollement zone. At these depths, with an estimated temperature of 90°C, bacterial abundance reappears within the envelope predicted by the model. Bacterial populations were not correlated with any of the in situ chemistry investigated and appear to be regulated solely by temperature at this site.

At Site 1177 bacterial abundance appears to be determined by sulfate. Coring began at 300 mbsf, where bacterial abundance was relatively low and remained so until 380 mbsf. Abundance in deeper samples (380–675 mbsf) steadily increased and was within predicted values from below 400 mbsf. This increase in bacterial numbers strongly correlated with increases in IW sulfate concentration that were unexpectedly present, at near-seawater concentrations, between 400 and 700 mbsf. Bacteria were also present at lower and decreasing concentrations between 725 and 811 mbsf despite methane concentrations increasing significantly below 740 mbsf. Overall low bacterial populations and high sulfate concentrations are probably attributable to very low total organic carbon concentrations restricting bacterial sulfate reduction. Why populations do not react to increasing concentrations of methane below 740 mbsf remains unclear as the temperature gradient at this site was shallow with the hole estimated at <40°C throughout.

CONCLUSIONS

During Leg 190, we successfully cored six sites, meeting most of the leg objectives and also revealing some surprising new findings. We demonstrated that there is a large contrast among the various properties, including the lithologic and geochemical (including microbial activity) character of the incoming sequences at the Muroto and Ashizuri Transects. In spite of such contrast, we found that the décollement at both transects stays at the level of an almost identical horizon (6–7 Ma). We also documented the accretionary history of the Nankai Trough prism for the first time and revealed a phenomenally rapid rate of growth of the prism during the Pleistocene. Our results will provide a basic framework for further mechanical, hydrogeological, and geochemical studies of this accretionary prism.

Leg 190 results will also be useful for understanding the tectonics of accretionary prism evolution providing a link between prism-toe processes and highly deformed accretionary complexes, which are the dominant components of orogenic belts.

REFERENCES

Aoike, K., 1999. Tectonic evolution of the Izu collision zone. *Res. Report of Kanagawa Prefectural Museum of Natural History*, 9:113–151 (in Japanese).

Aoki, Y., Tamano, T., and Kato, S., 1982. Detailed structure of the Nankai Trough from migrated seismic sections. *In* Watkins, J.S., and Drake, C.L. (Eds.), *Studies in Continental Margin Geology.* AAPG Mem., 34:309–322.

Ando, M., 1975. Source mechanisms and tectonic significance of historical earthquakes along the Nankai Trough, Japan. *Tectonophysics,* 27:119–140.

Ando, M., 1991. A fault model of the 1946 Nankaido earthquake derived from tsunami data. *Phys. Earth Planet. Inter.,* 28:320–336.

Ashi, J., and Taira, A., 1993. Thermal structure of the Nankai accretionary prism as inferred from the distribution of gas hydrate BSRs. *In* Underwood, M.B. (Ed.), *Thermal evolution of the Tertiary Shimanto Belt, Southwest Japan: an example of ridge-trench interaction.* Spec. Paper.– Geol. Soc. Am., 273:137–149.

Ashi, J., and Taira, A., 1992. Structure of the Nankai accretionary prism as revealed from IZANAGI sidescan imagery and multichannel seismic reflection profiling. *Isl. Arc,* 1:104–115.

Bangs, N.L., Taira, A., Kuramoto, S., Shipley, T.H., Moore, G.F., Mochizuki, K., Gulick, S.S., Zhao, Z., Nakamura, Y., Park, J.-O., Taylor, B.L., Morita, S., Ito, S., Hills, D.J., Leslie, S.C., Alex, C.M., McCutcheon, A.J., Ike, T., Yagi, H., and Toyama, G., 1999. U.S.-Japan Collaborative 3-D seismic investigation of the Nankai Trough plate-boundary interface and shallowmost seismogenic zone. *Eos,* 80:F569.

Bray, C.J., and Karig, D.E., 1988. Porosity of sediments in accretionary prisms and some implications for dewatering processes. *J. Geophys. Res.,* 90:768–778.

Byrne, T., Maltman, A., Stephenson, E., Soh, W., and Knipe, R., 1993. Deformation structures and fluid flow in the toe region of the Nankai accretionary prism. *In* Hill, I.A., Taira. A., Firth, J.V., et al., *Proc. ODP, Sci. Results,* 131: College Station, TX (Ocean Drilling Program), 83–101.

Cande, S.C., and Kent, D.V., 1995. Revised calibration of the geomagnetic polarity timescale for the Late Cretaceous and Cenozoic. *J. Geophys. Res.* 100:6093–6095.

Davis, E.E., Becker, K., Pettigrew, T., Carson, B., and MacDonald, R., 1992. CORK: a hydrologic seal and downhole observatory for deep-ocean boreholes. In Davis, E.E., Mottl, M.J., Fisher, A.T., et al., *Proc. ODP, Init. Repts.,* 139: College Station, TX (Ocean Drilling Program), 43–53.

Hyndman, R.D., Yamano, M., and Oleskevich, D.A., 1997. The seismogenic zone of subduction thrust faults. *Isl. Arc,* 6:244–260.

Hyndman, R.D., Wang, K. and Yamano, M., 1995 Thermal constraints on the seismogenic portion of the southwestern Japan subduction thrust. *J. Geophys. Res.,* 100:15373–15392.

Ito,Y., and Nagasaki, Y., 1997. Crustal shortening of southwest Japan in the late Miocene. *Isl. Arc.*, 5:337–353.

Jolivet, L.K., Tamaki, K., and Frounier, M., 1994. Japan Sea, opening history and mechanism: a synthesis. *Jour. Geophys. Res.,* 99:22237–22259.

Kamata, H., and Kodama, K., 1994. Tectonics of an arc-arc junction: an example from Kyushu Island at the junction of the southwest Japan Arc and Ryukyu Arc. *J. Geophys. Res.*, 233:69–81.

Kano, K., Kato, H., Yanagisawa, Y., and Yoshida, F., 1991. Stratigraphy and geologic history of the Cenozoic of Japan. *Geological Survey of Japan,* 274:114.

Karig, D.E., 1986. The framework of deformation in the Nankai Trough. *In* Kagami, H., Karig, D.E., and Coulbourn, W.T., et al., *Init Repts. DSDP,* 87: Washington (U.S. Govt. Printing Office), 927–940.

Karig, D.E., and Angevine, C.L., 1986. Geologic constraints on subduction rates in the Nankai Trough. *In* Kagami, H., Karig, D.E., and Coulbourn, W.T., et al., *Init Repts. DSDP,* 87: Washington (U.S. Govt. Printing Office), 789–796.

Kastner, M., Elderfield, H., Jenkins, W.J., Gieskes, J.M., and Gamo, T., 1993. Geochemical and isotopic evidence for fluid flow in the western Nankai subduction zone, Japan. *In* Hill, I.A., Taira. A., Firth, J.V., et al., *Proc. ODP, Sci. Results,* 131: College Station, TX (Ocean Drilling Program), 397–413.

Kinoshita, H., and Yamano, M., 1986. The heat flow anomaly in the Nankai Trough area. *In* Kagami, H., Karig, D.E., and Coulbourn, W.T., et al., *Init Repts. DSDP,* 87: Washington (U.S. Govt. Printing Office), 737–743.

Kodaira, S., Takahashi, N., Park, J., Mochizuki, K., Shinohara, M., and Kimura, S., 2000. Western Nankai Trough seismogenic zone: results from a wide-angle ocean bottom seismic survey. *J. Geophys. Res.,* 105:5887–5905.

Kodaira, S., 2000. High resolution imaging of seismogenic plate boundary. *Annual Report of Frontier Research Program for Subduction Dynamics,* Jamstec, 39–44.

Le Pichon, X., Iiyama, T., Chamley, H., Charvet, J., Faure, M., Fujimoto, H., Furuta, T., Ida, Y., Kagami, H., Lallemant, S., Leggett, J., Murata, A., Okada, H., Rangin, C., Renard, V., Taira, A., and Tokuyama, H., 1987. Nankai Trough and the fossil Shikoku Ridge: results of Box 6 Kaiko survey. *Earth Planet. Sci. Lett.,* 83:186–198.

Le Pichon, X., Mazzotti, M., Henry, P., and Hashimoto, M., 1998. Deformation of the Japanese Islands and seismic coupling: an interpretation based on GSI permanent GPS observations. *Geophys. J. Int.,* 134:501–514.

Maltman, A.J., Byrne, T., Karig, D.E., Lallemant, S., Knipe, R., and Prior, D., 1993. Deformation structures at Site 808, Nankai accretionary prism, Japan. *In* Hill, I.A., Taira, A., Firth, J.V., et al., *Proc. ODP, Sci. Results,* 131: College Station, TX (Ocean Drilling Program), 123–133.

Mazzotti, S., LePichon, X., Henry, P., and Miyazaki, S., 2000. Full Interseismic locking of the Nankai and Japan-West Kuril Subduction Zones: an analysis of uniform elastic strain accumulation in Japan constrained by permanent GPS. *J. Geophys. Res.,* 105:13159–13177.

Morgan, J K., and Karig, D.E., 1995. Décollement processes at the Nankai accretionary margin, Southeast Japan: Propagation, deformation, and dewatering, *J. of Geophys. Res.,* 100:15221–15231.

Moore, G.F., Shipley, T.H., 1993. Character of the décollement in the Leg 131 area, Nankai Trough. *In* Hill, I.A., Taira. A., Firth, J.V., et al., *Proc. ODP, Sci. Results,* 131: College Station, TX (Ocean Drilling Program), 73–82.

Moore, G.F., Shipley, T.H., Stoffa, P.L., Karig, D.E., Taira, A., Kuramoto, S., Tokuyama, H., and Suyehiro, K., 1990. Structure of the Nankai Trough accretionary zone from multichannel seismic reflection data. *J. Geophys. Res.,* 95:8753–8765.

Moore, G.F., Karig, D.E., Shipley, T.H., Taira, A., Stoffa, P.L., and Wood, W.T., 1991. Structural framework of the ODP Leg 131 area, Nankai Trough. *In* Taira, A., Hill, I.A.,

Firth, J.V., et al., *Proc. ODP, Init. Repts,* 131: College Station, TX (Ocean Drilling Program), 15–20.

Moore, G.F., Taira, A., Kuramoto, S., Shipley, T.H., and Bangs, N.L., 1999. Structural setting of the 1999 U.S.-Japan Nankai Trough 3-D seismic reflection survey. *Eos,* 80:F569.

Morgan, J.K., and Karig, D.E., 1995a. Kinematics and a balanced and restored cross-section across the toe of the eastern Nankai accretionary prism. *J. Struc. Geol.,* 17:31–45.

Morgan,. J.K., and Karig, D.E., 1995b. Décollement processes at the Nankai accretionary margin, Southeast Japan. *J. Geophys. Res.,* 100:15221–15231.

Niitsuma, N., 1989. Collision tectonics in the southern Fossa Magna, central Japan. *Mod. Geol.,* 14:3–18.

Ohmori, K., Taira, A., Tokuyama, H., Sagaguch, A., Okamura, M., and Aihara., A., 1997. Paleothermal structure of the Shimanto accretionary prism, Shikoku, Japan: Role of an out-of-sequence thrust. *Geology,* 25, 327–330.

Okamura, Y., Kisimoto, K., Murakami, F., and Joshima, M., 1987. Geological map of Tosa Bay. *Geol. Surv. Jpn., Mar. Geol. Map Ser.,* 29 (scale 1:200,000).

Okino, K., and Kato, Y., 1995. Geomorphological study on a clastic accretionary prism: the Nankai Trough. *Isl. Arc.,* 4:182–198.

Okino, K., Shimakawa, Y., and Nagaoka, S., 1994. Evolution of the Shikoku basin. *J. Geomagn. Geoelectr.,* 46:463–479.

Otofuji, Y., 1996. Large tectonic movement of the Japan Arc in late Cenozoic times inferred from paleomagnetism: review and synthesis. *Isl. Arc,* 5:229–249.

Park, J-O., Tsuru, T., Kaneda, Y., Kono, Y., Kodaira, S., Takahashi, N., and H. Kinoshita. 1999. A subducting seamount beneath the Nankai accretionary prism off Shikoku, southwestern Japan. *Geophys. Res. Lett.,* 26:931–934.

Park, J-O., Tsuru, T., Kodaira, S., Nakanisi, A., Miura, S., Kaneda, Y., and Kono, Y., 2000. Out-of-sequence thrust faults developed in the coseismic slip zone of the 1946 Nankai earthquake (Mw = 8.2) off Shikoku, southwest Japan. *Geophys. Res. Lett.,* 27:1033–1036.

Parkes, R.J., Cragg, B.A., Bale, S.J., Getliff, J.M., Goodman, K., Rochelle, P.A., Fry, J.C., Weightman, A.J., and Harvey, S.M. 1994. A deep bacterial biosphere in Pacific Ocean sediments. *Nature,* 371:410–413.

Pickering, K.T., Underwood, M., and Taira, A., 1993. Open-ocean to trench turbidity-current flow in the Nankai Trough: flow collapses and flow reflection. *In* Hill, I.A., Taira, A., Firth, J.V., et al., *Proc. ODP, Sci. Results,* 131: College Station, TX (Ocean Drilling Program), 35–43.

Saffer, D.M., and Bekins, B.A., 1998. Episodic fluid flow in the Nankai Accretionary Complex: timescale, geochemistry, flow rates, and fluid budget. J. Geophys. Res., 103:30351–30371.

Saffer, D. M., Silver, E. A., Fisher, A. T., Tobin, H., and Moran, K., 2000, Inferred pore pressures at the Costa Rica subduction zone: Implication for dewatering processes, *Earth Planet. Sci Lett.,* 177:193–207.

Sagiya, T. and Thactcher W. 1999. Coseismic slip resolution along a plate boundary megathrust: the Nankai Trough, southwest Japan. *J. Geophys. Res.,* 104:1111–1129.

Seno, T., 1977. The instantaneous rotation vector of the Philippine Sea Plate relative to the Eurasian Plate. *Tectonophysics,* 42:209–226.

Shipboard Scientific Party, 1973. Site 297. *In* Karig, D.E., Ingle, J.C, Jr., et al., *Init. Repts. DSDP*, 31: Washington (U.S. Govt. Printing Office), 275–316.

Shipboard Scientific Party, 1986. Site 582. *In* Kagami,H., Karig, D.E., Coulbourn, W.T., et al., *Init. Repts. DSDP*, 87: Washington (U.S. Govt. Printing Office), 35–122

Shipboard Scientific Party, 1991. Site 808. *In* Taira, A., Hill, I., Firth, J.V., et al., Proc. ODP, *Init. Repts.*, 131: College Station,TX (Ocean Drilling Program), 71–269.

Stoffa, P.L., Wood, W.T., Shipley, T.H., Moore, G.F., Nishyama, E., Bothelo, M.A.B., Taira, A., Tokuyama, H., and Suyehiro, K., 1992. Deepwater high-resolution expanding spread and split spread marine seismic profiles in the Nankai Trough. *J. Geophys. Res.*, 97:1687–1713.

Sugiyama, Y. 1994. Neotectonics of Southwest Japan due to the right oblique subduction of the Philippine sea plate. *Geofisica Internacional,* 33:53–76.

Taira, A., and Niitsuma, N., 1986. Turbidite sedimentation in the Nankai Trough as interpreted from magnetic fabric, grain size, and detrital modal analyses. *In* Kagami, H., Karig, D.E.,

Coulbourn, W.T., et al., *Init. Repts. DSDP,* 87: Washington (U.S. Govt Printing Office), 611–632.

Taira, A., and Ashi, J., 1993. Sedimentary facies evolution of the Nankai forearc and its implications for the growth of the Shimanto accretionary prism. *In* Hill, I.A., Taira. A., Firth, J.V., et al., *Proc. ODP, Sci. Results,* 131: College Station, TX (Ocean Drilling Program), 331–341.

Taira, A., Hill, I., Firth, J.V., et al., 1991. *Proc. ODP, Init. Repts.,* 131: College Station, TX (Ocean Drilling Program).

Taira, A., Katto, J., Tashiro, M., Okamura, M., and Kodama, K., 1988. The Shimanto Belt in Shikoku, Japan–evolution of Cretaceous to Miocene accretionary prism. *Mod. Geol.,* 12:5–46.

Taira, A., Tokuyama, H., and Soh, W., 1989. Accretion tectonics and evolution of Japan. *In* Ben-Avraham, Z. (Ed.), *The Evolution of the Pacific Ocean Margins:* Oxford (Oxford Univ. Press), 100–123.

Taira, A., Hill, I., Firth, J., Berner, U., Brückmann, W., Byrne, T., Chabernaud, T., Fisher, A., Foucher, J.-P., Gamo, T., Gieskes, J., Hyndman, R., Karig, D., Kastner, M., Kato, Y., Lallement, S., Lu, R., Maltman, A., Moore, G., Moran, K., Olaffson, G., Owens, W., Pickering, K., Siena, F., Taylor, E., Underwood, M., Wilkinson, C., Yamano, M., and Zhang, J., 1992. Sediment deformation and hydrogeology of the Nankai Trough accretionary prism: synthesis of shipboard results of ODP Leg 131. *Earth Planet. Sci. Lett.,* 109:431–450.

Takahashi, M., 1999. Large felsic magmatism of the Miocene outerzone of southwest Japan. *Earth Monthly,* Special Volume 23, 160–168. (in Japanese)

Taylor, B., 1992. Rifting and the volcanic-tectonic evolution of the Izu-Bonin-Mariana Arc. *In* Taylor, B., Fujioka, K., et al., *Proc. ODP, Sci. Results,* 126. College Station, TX (Ocean Drilling Program), 627–651.

Tokuyama, H., Ashi, J., Soh, W., Kuramoto, S., and Ikeda, Y., 1999. *Submarine active faults off Tokai.* University of Tokyo Press. Tokyo. (in Japanese with English explanation on maps)

Underwood, M.B., Orr, R., Pickering, K. and Taira, A., 1993. Provenance and dispersal patterns of sediments in the turbidite wedge of Nankai Trough. *In* Hill, I.A., Taira. A., Firth, J.V., et al., *Proc. ODP, Sci. Results,* 131: College Station, TX (Ocean Drilling Program), 15–34.

Yamazaki, T. and Okamura, Y. 1989. Subducting seamounts and deformation of overriding forearc wedges around Japan. *Tectonophysics.* 160:207–229.

TABLE CAPTION

Table 1. Leg 190 site summary.

FIGURE CAPTIONS

Figure 1. Shaded relief map of the Nankai Trough produced from the Hydrographic Department of Japan's topographic data set (500-m grid interval). The inset shows a tectonic map of the Philippine Sea region that includes the Nankai Trough. The black box outlines the Leg 190 Nankai drilling area shown in Figure 6. The arrow shows the convergence direction of the Shikoku Basin beneath Japan.

Figure 2. Geologic map of the southwest Japan forearc region and the Leg 190 Muroto and Ashizuri drilling transects. The Shimanto accretionary prism provides a landward analog of the Nankai accretionary prism. Note the widespread 17- to 12-Ma igneous activity, probably due to the initial subduction of the young Shikoku Basin oceanic lithosphere. Previous ODP/DSDP drill sites are shown by open circles. The dashed line shows the location of the cross section shown in Figure 3.

Figure 3. Crustal cross section of the Nankai Trough forearc (modified after Kodaira et al., 2000). Crustal structure, crustal velocities, and subducting plate earthquakes are shown. Note that the updip limit of 1946 Nankaido earthquake rupture zone possibly reaches to the Nankai Trough accretionary prism. MTL = median tectonic line.

Figure 4. Paleogeographic reconstruction of the Shimanto Belt and Nankai forearc evolution. After Taira et al. (1989). Arrows show the direction of convergence.

Figure 5. Historical recurrence time interval of class M8 earthquakes along the Nankai Trough. Zones A to D represent rupture area segments.

Figure 6. ODP Leg 190 (solid circles) and previous ODP/DSDP drill sites (solid squares) in the Nankai Trough. The shaded outline shows the 3-D seismic survey of Bangs et al. (1999) and Moore et al. (1999). Contour interval = 100 m.

Figure 7. Schematic interpretation of seismic line 141-2D in the Muroto Transect showing tectonic domains and location of Leg 190 drill sites.

Figure 8. A. Correlation of facies units, magnetic susceptibility, and major time boundaries within stratigraphic successions of the reference and prism toe sites at the Muroto and Ashizuri

Transects at Nankai margin. Time boundaries are in red (solid line). Facies boundaries are in blue (Muroto Transect) and purple (Ashizuri Transect)(patterned lines). Data for DSDP Site 297 are from Shipboard Scientific Party (1973). Data for DSDP Site 582 are from Shipboard Scientific Party (1986). Data for ODP Site 808 are from Shipboard Scientific Party (1991). Note that the effects of facies imbrication along the frontal thrust of Site 808 have been removed and that the position of the Pliocene/Miocene boundary has been shifted in response to reinterpretation of paleomagnetic data. **B.** Correlation of facies units, magnetic susceptibility, and major time boundaries within stratigraphic successions cored at upslope sites of the Muroto Transect, Nankai margin. Time boundaries are in red (solid line). Facies boundaries are in blue (patterned line).

Figure 9. Seismic reflection profile through the Muroto Transect reference (Site 1173) and prism toe sites (Sites 1174 and 808). Correlation of sedimentary facies to the seismic data is shown on the right. Seismic data are from the 3-D seismic survey of Bangs et al. (1999) and Moore et al. (1999). Xline identifies the crossing line number in the 3-D seismic volume.

Figure 10. Seismic reflection profile (NT-2) through Ashizuri Transect reference site (Site 1177), trench site (Site 582), and prism toe site (Site 583).

Figure 11. Seismic reflection profile through the Muroto Transect slope Sites 1175, 1176, and 1178. Seismic data are from the 3-D seismic survey of Bangs et al. (1999) and Moore et al. (1999). Xline identifies the crossing line number in the 3-D seismic volume.

Figure 12. Summary of results at Site 1173.

Figure 13. Photograph of volcanic ash beds interbedded with silty clay from Unit II (interval 190-1173A-13H-6, 100–124 cm).

Figure 14. Photograph of bioturbated silty claystone and interbedded siliceous claystone from Unit III (interval 190-1173A-57X-4, 66–71 cm).

Figure 15. Summary of results at Site 1174.

Figure 16. Photograph of graded interval of medium- to fine-grained sand with some mudchips in the upper part of Subunit IIA (intervals 190-1174A-8H, 0–40 and 40–80 cm).

Figure 17. Photographs showing deformation bands. **A.** Note the varying width and the tendency of the bands to bifurcate (interval 190-1174B-17R-2, 103–112 cm). **B.** Note the variation in the width of the more shallowly inclined set (interval 190-1174B-15R-2, 19–24 cm).

Figure 18. Stereographic equal-area lower hemisphere projections of deformation bands, illustrating the effectiveness of paleomagnetic reorientation. **A.** Deformation bands in the core liner reference frame, before paleomagnetic reorientation. **B.** Data in A after paleomagnetic correction to real geographic coordinates (excluding some planes for which the paleomagnetic information was not available). Note the concentration into two oppositely dipping sets. **C.** Poles to the planes shown in B. **D.** Average of the two sets of deformation bands showing the dihedral angle and the inclination of the acute bisectrix from vertical.

Figure 19. **A.** Photograph of the upper part of décollement zone, showing breakage into angular blocks along inclined fractures (interval 190-1174B-71R-2, 48–79 cm). **B.** Photograph of the lower part of décollement zone, showing comminution of sediments (interval 190-1174B-73R-1, 96–118 cm).

Figure 20. Details of fracturing across the décollement zone. The density of fracturing is expressed by the nature and size of the brecciated fragments. Most of the fracture surfaces are slickensided and slickenlined. Note the trend of increasing fracturing downward through the zone, peaking a few meters above a sharply defined base.

Figure 21. Summary of results at Site 1175.

Figure 22. Photograph showing chaotic bedding of Unit I (interval 190-1175A-9H-1, 65–110 cm).

Figure 23. Photograph showing pebbly mudstone of Unit III (interval 190-1175A-37X-4, 70–110 cm).

Figure 24. Summary of results at Site 1176.

Figure 25. Photograph of pebbles and gravel of quartz and lithic clasts in muddy matrix from Unit III (interval 190-1176A-47X-CC, 0–28 cm).

Figure 26. Summary of results at Site 1177.

Figure 27. Photograph of a wood-rich sandy turbidite interbedded with silty claystone from Unit III (interval 190-1177A-43R-3, 0–25 cm).

Figure 28. Photograph of laminated and bioturbated volcanic ash of Unit IV (interval 190-1177A-49R-4, 77–101 cm).

Figure 29. Photograph showing contact between green basal mudstone (Unit IV) and basalt

(Unit V) (interval 190-1177A-56R-3, 0–12 cm).

Figure 30. Summary of results at Site 1178.

Figure 31. Bedding-oblique foliation typical of Domain III (interval 190-1178B-9R-5, 5–27 cm). Steeply dipping bedding can be observed over the intervals 5–10 and 22–27 cm, bounding an interval with lower angle foliation.

Figure 32. Incipient scaly and foliated clays with fine black seams crosscutting the fracture fabric (interval 190-1178B-29R-3, 35–53 cm).

Figure 33. Incipient web-like structure in fine sand (interval 190-1178B-27R-3, 27–41 cm).

Figure 34. Bio- and magnetostratigraphic correlation between Leg 190 reference and prism toe sites of the Ashizuri and Muroto Transects.

Figure 35. Age-depth plots based on biostratigraphic (solid squares) and paleomagnetic (open circles) data for prism toe sites of the Ashizuri and Muroto Transects.

Figure 36. Comparison of the structurally identified décollement interval and its physical properties and pore-water geochemistry across the Leg 131/190 transect. The décollement interval at Site 1174 has been projected to the reference Site 1173 based on correlation of patterns in magnetic susceptibility data (see Fig. 8A).

Figure 37. Structural and stratigraphic interpretation of seismic profile across the Ashizuri Transect based on drilling sites.

Figure 38. Chloride concentrations in interstitial water samples from the Muroto Transect reference (Site 1173) and prism toe sites (Sites 1174 and 808).

Figure 39. Porosities and velocities across the Muroto Transect (Sites 1173, 1174, and 808) and Ashizuri reference site (Site 1177). Lithologic units and major structural features are shown. The décollement location is shown by gray shading where it was observed and by a dashed line at the stratigraphically equivalent depth at the reference sites.

Figure 40. Biostratigraphic and paleomagnetic ages as a function of solid thickness (thickness of the sediment after vertical compaction to 0% porosity) for Sites 808, 1174, 1173, and 1177. Lithostratigraphic units and their correlation between holes are indicated in blue (solid and dashed). The décollement interval is indicated at Sites 808 and 1174 (green/shaded). The red lines (patterned) mark the 4- to 7-Ma age interval. This interval appears thicker at the

décollement Sites 808 and 1174 than at the reference Sites 1173 and 1177.

Figure 41. Multiple sources (biogenic, thermogenic, and catagenic) and production mechanisms for the hydrocarbons encountered during Leg 190 were identified by plotting the methane (C_1), Bernard ratios ($C_1/[C_2+C_3]$), and sulfate profiles for the individual sites drilled during Leg 190. Note that depth scale is different for each plot. Vertical lines represent zones for thermogenic, mixed, and bacterial regions for the hydrocarbon profiles.

Figure 42. Biogeochemical profiles in sediments from Nankai Trough sites (Leg 190). **A.** Total bacterial populations at Sites 1173, 1174, and 1177. The small dashed curve represents a general regression line of bacterial numbers vs. depth in deep-sea sediments (Parkes et al., 1994), with 95% upper and lower prediction limits shown by large dashed curves. **B–D.** Sulfate, methane, and total organic carbon depth profiles for Sites 1173, 1174, and 1177, respectively. **E.** C_1/C_2 ratios for Sites 1173, 1174, and 1177.

Table 1. Leg 190 site summary.

Hole	Latitude	Longitude	Seafloor (mbsl)	Number of cores	Length (m) Cored	Length (m) Recovered	Recovery (%)	Drilled (m)	Total penetration (m)	Time on hole (hr)	Time on hole (days)
Site 1173											
1173A	32°14.6634′N	135°01.5085′E	4790.7	77	734.3	658.10	89.6	0.0	734.3	232.72	9.70
			Total:	**77**	**734.3**	**658.10**	**89.6**	**0.0**	**734.3**	**232.72**	**9.70**
Site 1174											
1174A	32°20.5377′N	134°57.3876′E	4751.2	9	74.1	47.04	63.5	0.0	74.1	42.50	1.77
1174B	32°20.5404′N	134°57.3866′E	4751.2	102	976.1	577.57	59.2	143.7	1119.8	333.00	13.88
			Total:	**111**	**1050.2**	**624.61**	**59.5**	**143.7**	**1193.9**	**375.50**	**15.65**
Site 1175											
1175A	32°35.8855′N	134°38.6745′E	2997.6	47	439.2	327.01	74.5	5.8	445.0	79.75	3.32
			Total:	**47**	**439.2**	**327.01**	**74.5**	**5.8**	**445.0**	**79.75**	**3.32**
Site 1176											
1176A	32°34.6976′N	134°39.9419′E	3020.5	48	443.5	226.25	51.0	6.1	449.6	76.50	3.19
			Total:	**48**	**443.5**	**226.25**	**51.0**	**6.1**	**449.6**	**76.50**	3.19
Site 1177											
1177A	31°39.1510′N	134°0.7132′E	4844.3	56	533.7	282.74	53.0	300.2	833.9	135.13	5.63
			Total:	**56**	**533.7**	**282.74**	**53.0**	**300.2**	**833.9**	**135.13**	**5.63**
Site 1178											
1178A	32°43.8608′N	134°28.7684′E	1741.7	44	410.8	340.19	82.8	0.0	410.8	77.75	3.24
1178B	32°43.8600′N	134°28.7809′E	1741.7	30	284.2	165.96	58.4	395.0	679.2	94.33	3.93
			Total:	**74**	**695.0**	**506.15**	**72.8**	**395.0**	**1090.0**	**172.08**	**7.17**
		Leg 190 totals:		**413**	**3895.9**	**2624.9**	**67.4**	**850.8**	**4746.7**	**1071.7**	**44.7**

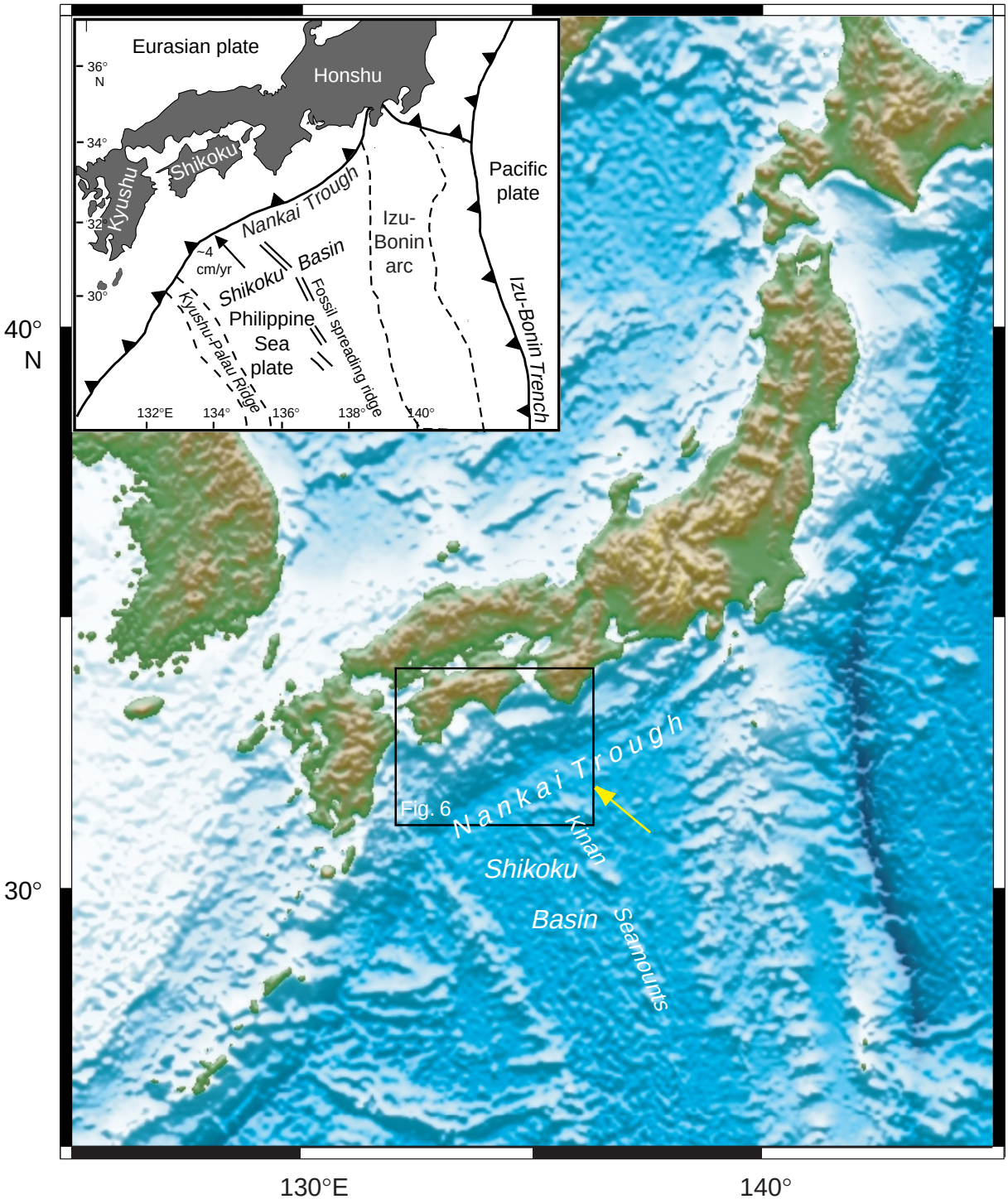
Eurasian plate
Honshu
Shikoku
Kyushu
Nankai Trough
~4 cm/yr
Shikoku Basin
Izu-Bonin arc
Pacific plate
Izu-Bonin Trench
Philippine Sea plate
Kyushu-Palau Ridge
Fossil spreading ridge
36° N
34°
32°
30°
132°E
134°
136°
138°
140°
40° N
30°
130°E
140°
Fig. 6
Nankai Trough
Kinan Seamounts
Shikoku Basin

Figure 1

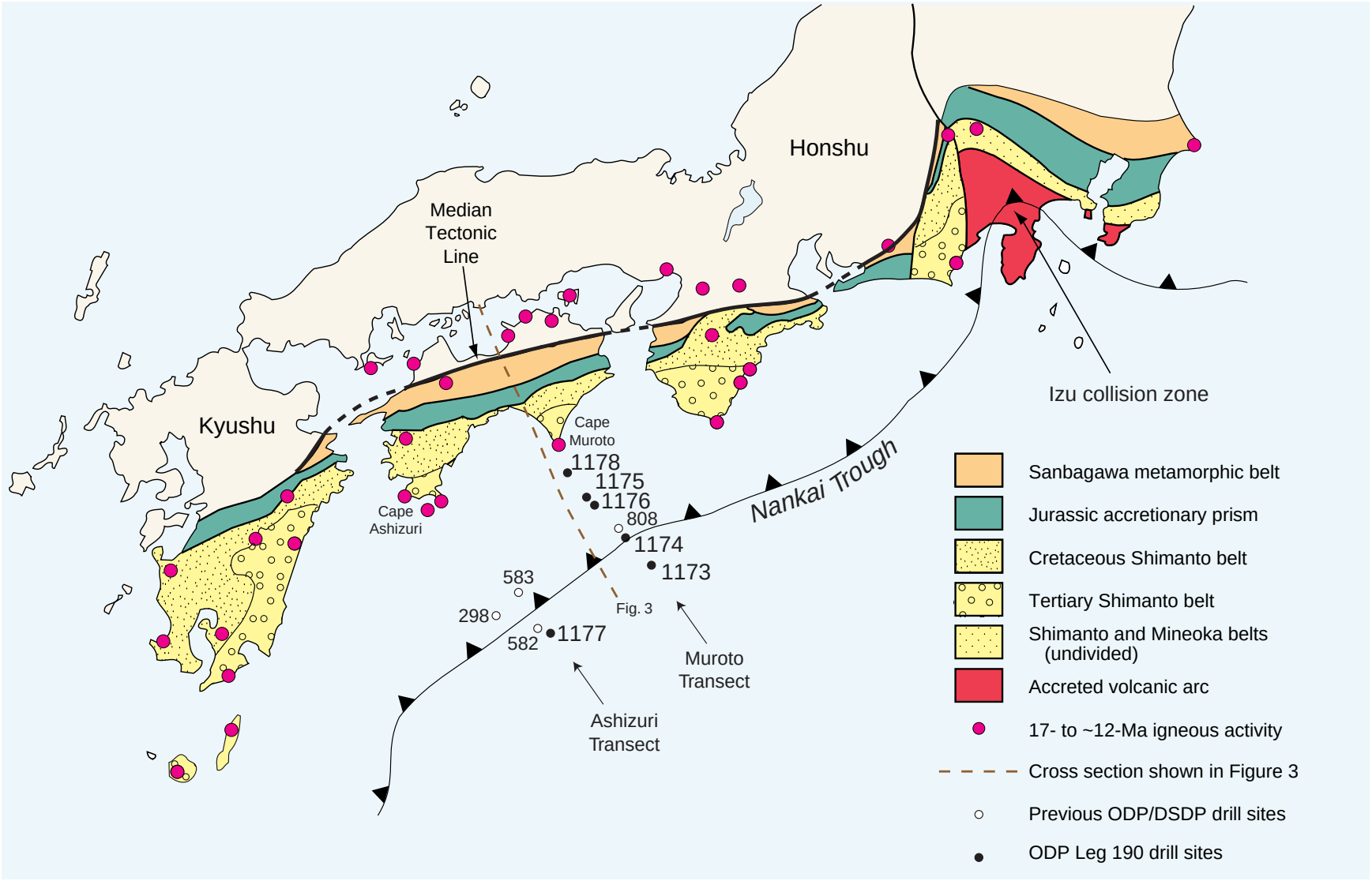
Honshu
Median
Tectonic
Line
Kyushu
Cape
Muroto
Cape
Ashizuri
1178
1175
1176
808
1174
1173
583
298
582
1177
Fig. 3
Nankai Trough
Izu collision zone
Muroto
Transect
Ashizuri
Transect
Sanbagawa metamorphic belt
Jurassic accretionary prism
Cretaceous Shimanto belt
Tertiary Shimanto belt
Shimanto and Mineoka belts
(undivided)
Accreted volcanic arc
17- to ~12-Ma igneous activity
Cross section shown in Figure 3
Previous ODP/DSDP drill sites
ODP Leg 190 drill sites

Figure 2

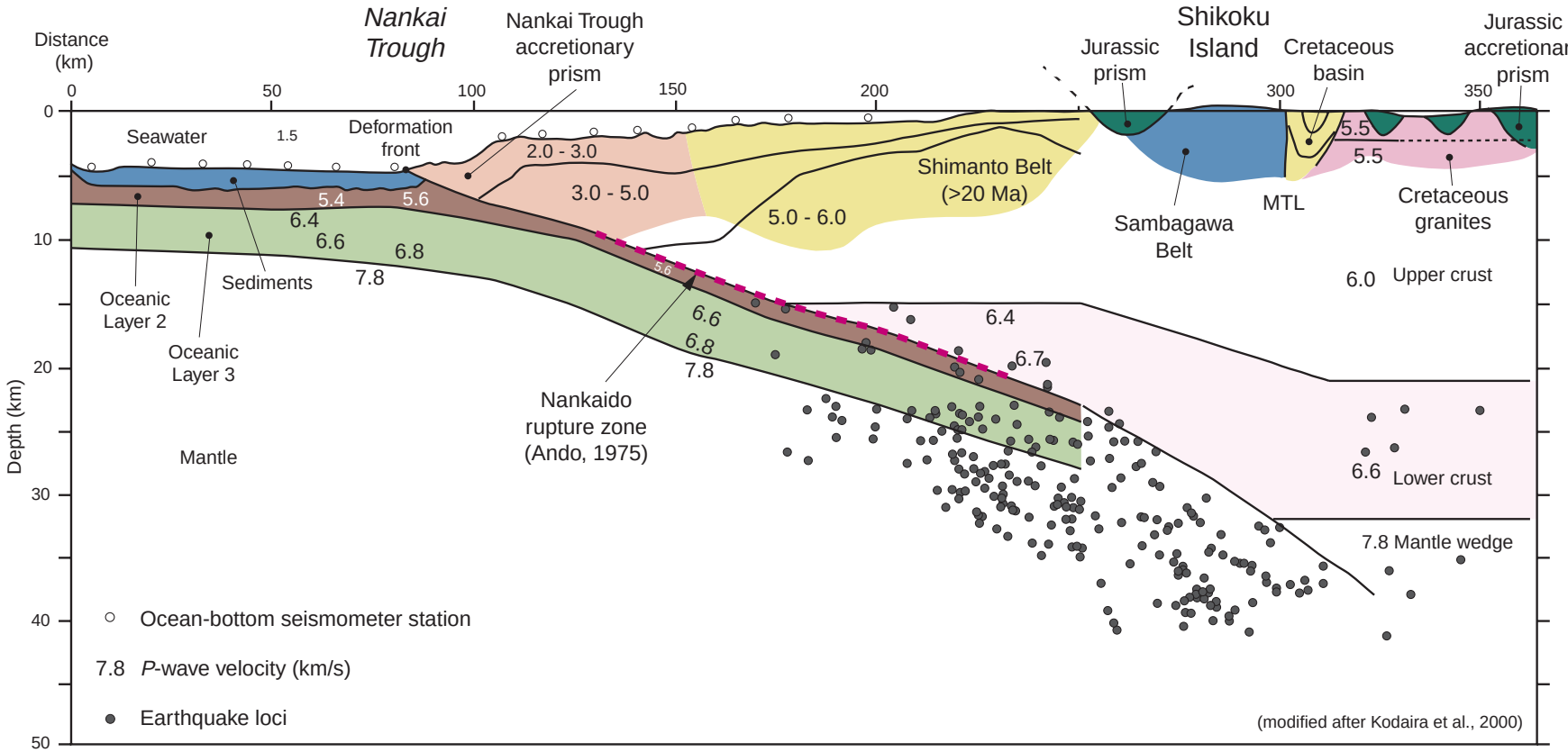
Distance (km)
Nankai Trough
Nankai Trough accretionary prism
Shikoku Island
Jurassic prism
Cretaceous basin
Jurassic accretionary prism
Seawater
1.5
Deformation front
2.0 - 3.0
3.0 - 5.0
5.0 - 6.0
Shimanto Belt (>20 Ma)
Sambagawa Belt
MTL
5.5
5.5
Cretaceous granites
5.4
5.6
6.4
6.6
6.8
7.8
Oceanic Layer 2
Sediments
Oceanic Layer 3
Mantle
Nankaido rupture zone (Ando, 1975)
6.0 Upper crust
6.4
6.7
6.6 Lower crust
7.8 Mantle wedge
Depth (km)
Ocean-bottom seismometer station
7.8 P-wave velocity (km/s)
Earthquake loci
(modified after Kodaira et al., 2000)

Figure 3

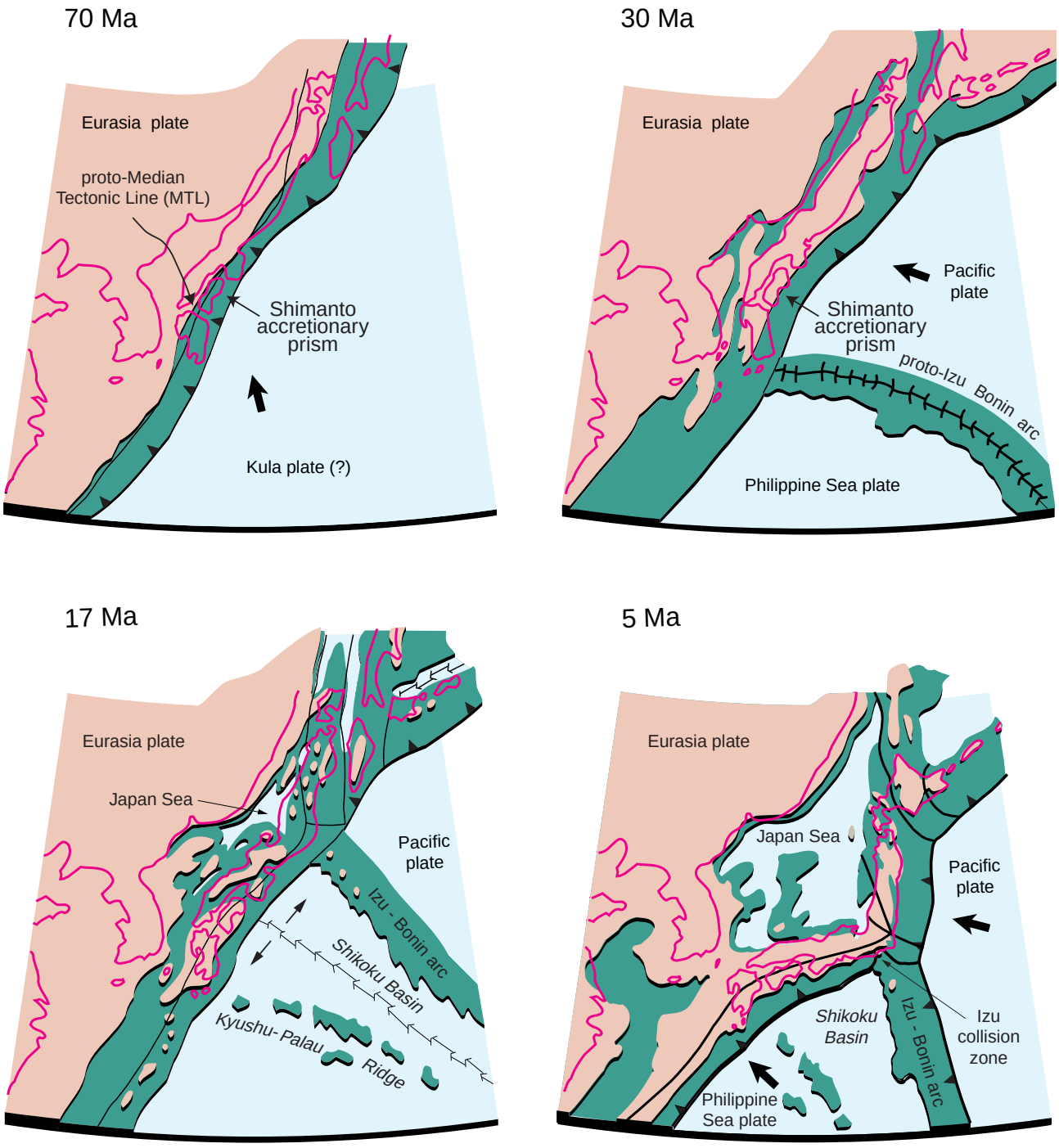
70 Ma
Eurasia plate
proto-Median
Tectonic Line (MTL)
Shimanto
accretionary
prism
Kula plate (?)
30 Ma
Eurasia plate
Pacific
plate
Shimanto
accretionary
prism
proto-Izu Bonin arc
Philippine Sea plate
17 Ma
Eurasia plate
Japan Sea
Pacific
plate
Izu - Bonin arc
Shikoku Basin
Kyushu- Palau Ridge
5 Ma
Eurasia plate
Japan Sea
Pacific
plate
Shikoku
Basin
Izu - Bonin arc
Izu
collision
zone
Philippine
Sea plate

Figure 4

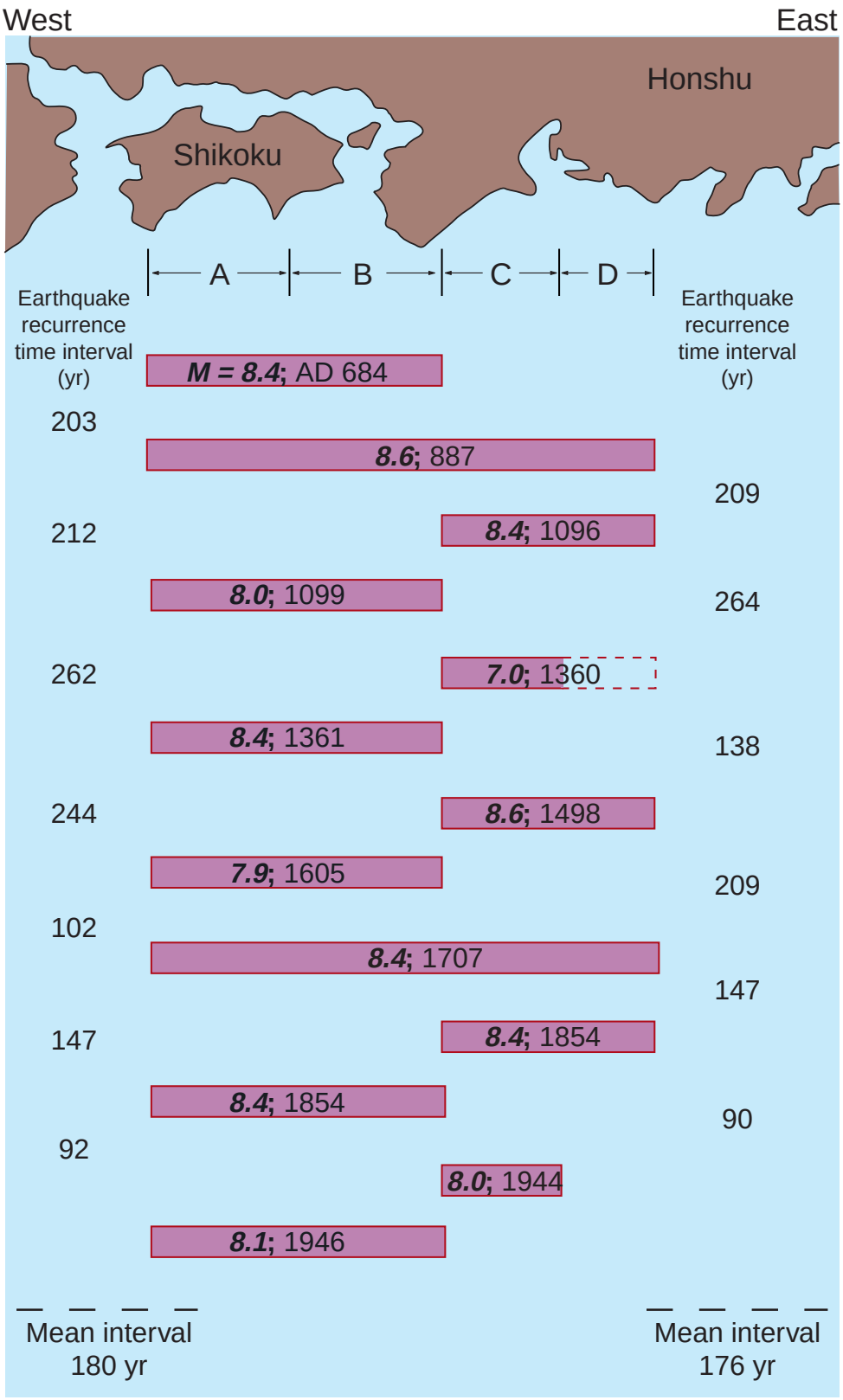
West
East
Honshu
Shikoku
A
B
C
D
Earthquake recurrence time interval (yr)
Earthquake recurrence time interval (yr)
M = 8.4; AD 684
203
8.6; 887
209
212
8.4; 1096
8.0; 1099
264
262
7.0; 1360
8.4; 1361
138
244
8.6; 1498
7.9; 1605
209
102
8.4; 1707
147
147
8.4; 1854
8.4; 1854
90
92
8.0; 1944
8.1; 1946
Mean interval 180 yr
Mean interval 176 yr

Figure 5

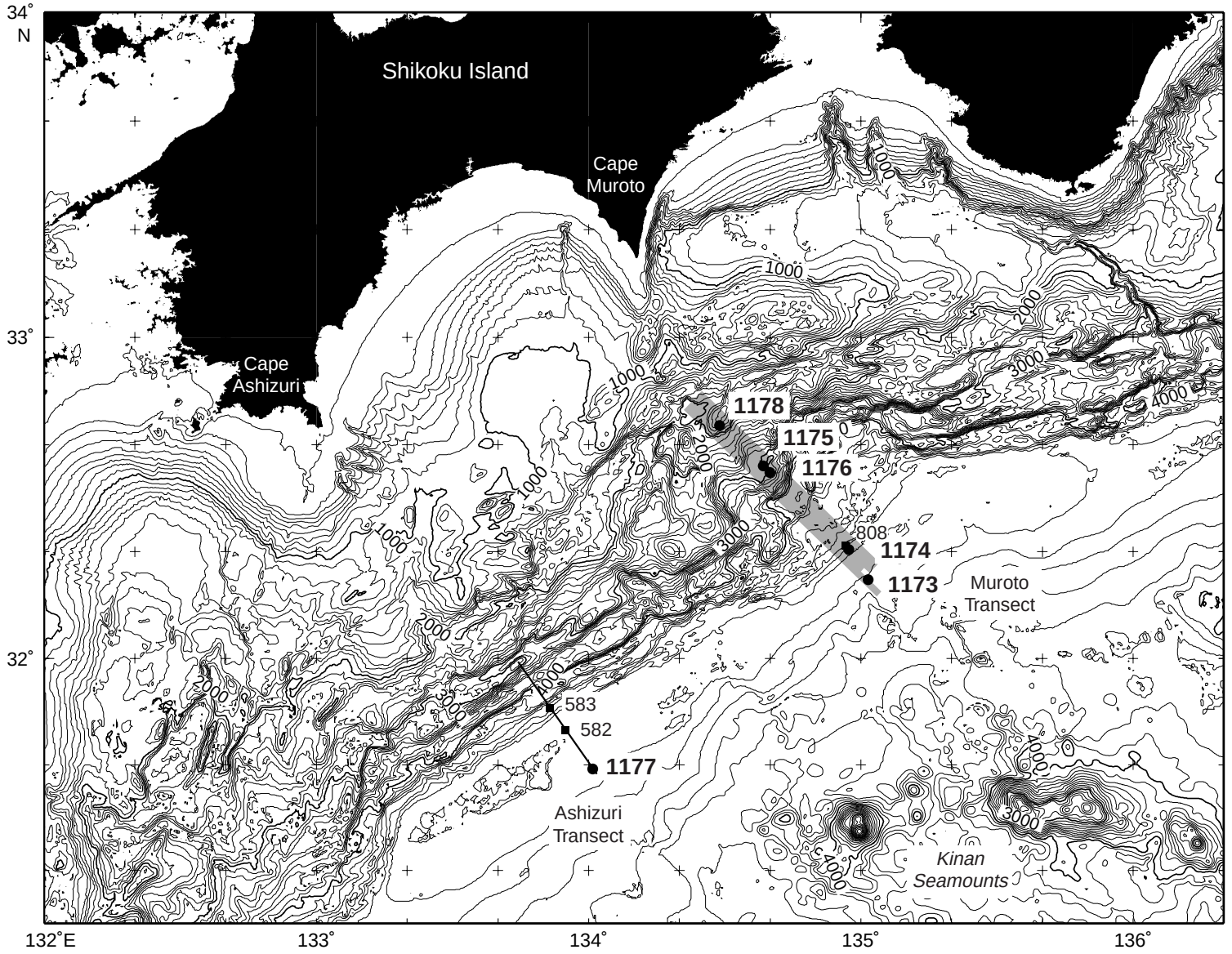
34˚
N
33˚
32˚
132˚E
133˚
134˚
135˚
136˚
Shikoku Island
Cape
Muroto
Cape
Ashizuri
1178
1175
1176
808
1174
1173
Muroto
Transect
583
582
1177
Ashizuri
Transect
Kinan
Seamounts
1000
2000
3000
4000

Figure 6

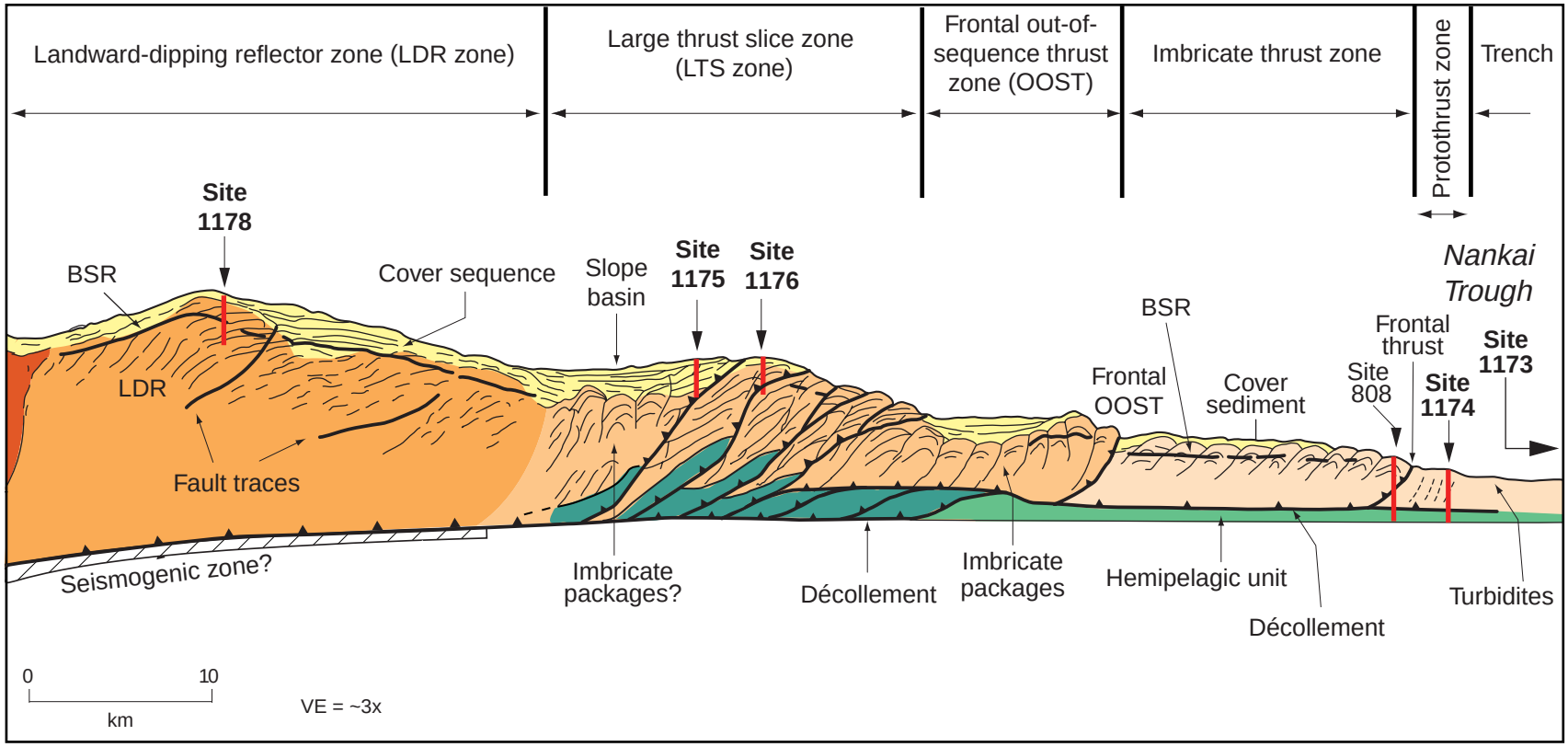
Landward-dipping reflector zone (LDR zone)
Large thrust slice zone (LTS zone)
Frontal out-of-sequence thrust zone (OOST)
Imbricate thrust zone
Protothrust zone
Trench
Site 1178
BSR
Cover sequence
Slope basin
Site 1175
Site 1176
Nankai Trough
BSR
Frontal thrust
Site 1173
Frontal OOST
Cover sediment
Site 808
Site 1174
LDR
Fault traces
Seismogenic zone?
Imbricate packages?
Décollement
Imbricate packages
Hemipelagic unit
Décollement
Turbidites
0
10
km
VE = ~3x

Figure 7

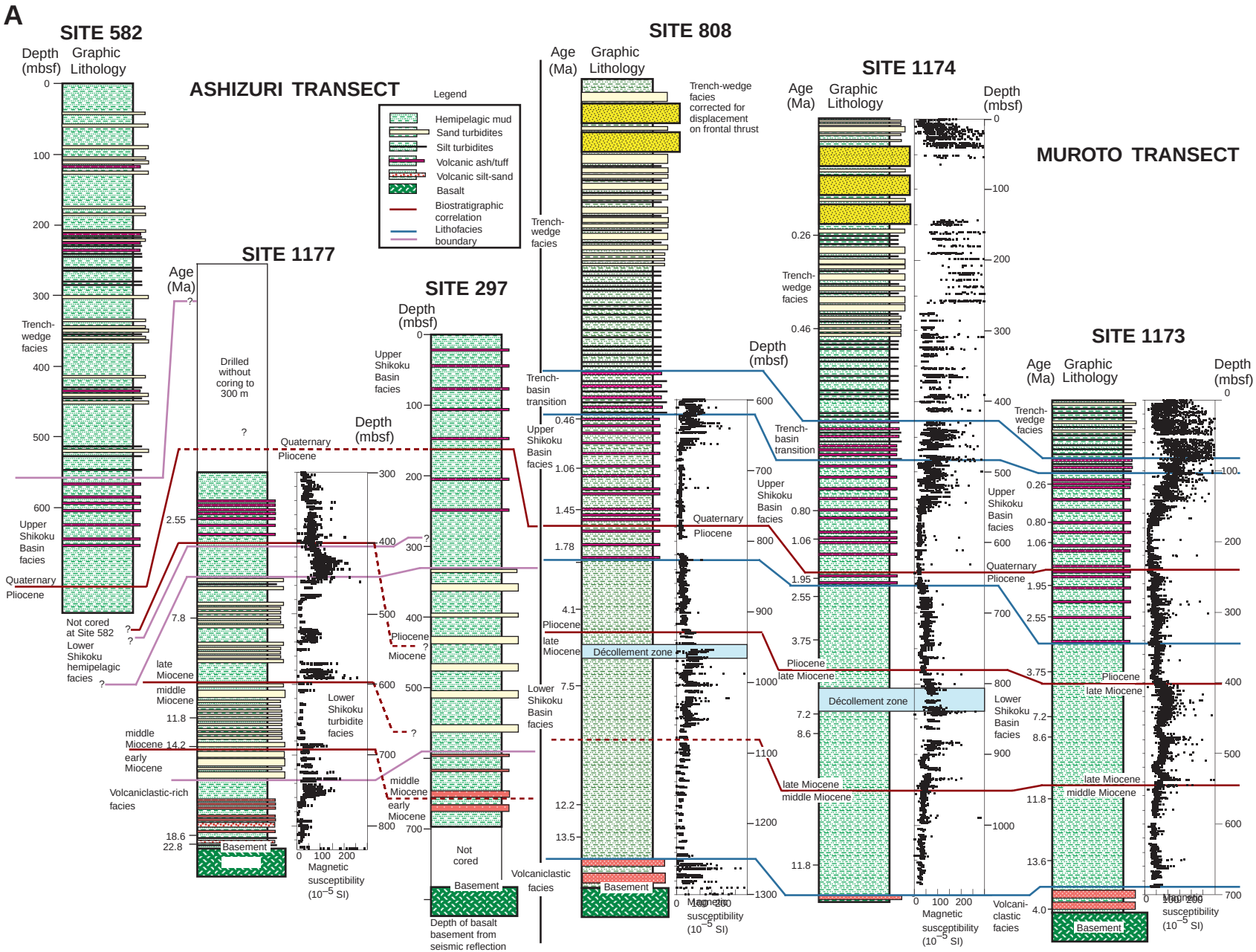
A
ASHIZURI TRANSECT
MUROTO TRANSECT
Legend
Hemipelagic mud
Sand turbidites
Silt turbidites
Volcanic ash/tuff
Volcanic silt-sand
Basalt
Biostratigraphic correlation
Lithofacies boundary
SITE 582
Depth (mbsf)
Graphic Lithology
Trench-wedge facies
Upper Shikoku Basin facies
Quaternary
Pliocene
Not cored at Site 582
Lower Shikoku hemipelagic facies
SITE 1177
Age (Ma)
Drilled without coring to 300 m
late Miocene
middle Miocene
middle Miocene
early Miocene
Volcaniclastic-rich facies
Basement
Lower Shikoku turbidite facies
Magnetic susceptibility (10^{-5} SI)
SITE 297
Depth (mbsf)
Upper Shikoku Basin facies
Quaternary
Pliocene
Pliocene
Miocene
middle Miocene
early Miocene
Not cored
Basement
Depth of basalt basement from seismic reflection
SITE 808
Age (Ma)
Graphic Lithology
Trench-wedge facies corrected for displacement on frontal thrust
Trench-wedge facies
Trench-basin transition
Upper Shikoku Basin facies
Quaternary
Pliocene
late Miocene
Décollement zone
Lower Shikoku Basin facies
Volcaniclastic facies
Basement
Magnetic susceptibility (10^{-5} SI)
SITE 1174
Age (Ma)
Graphic Lithology
Depth (mbsf)
Trench-wedge facies
Trench-basin transition
Upper Shikoku Basin facies
Quaternary
Pliocene
late Miocene
middle Miocene
Décollement zone
Lower Shikoku Basin facies
Volcaniclastic facies
Magnetic susceptibility (10^{-5} SI)
SITE 1173
Age (Ma)
Graphic Lithology
Depth (mbsf)
Trench-wedge facies
Upper Shikoku Basin facies
Quaternary
Pliocene
late Miocene
middle Miocene
Lower Shikoku Basin facies
Basement
Magnetic susceptibility (10^{-5} SI)

Figure 8A

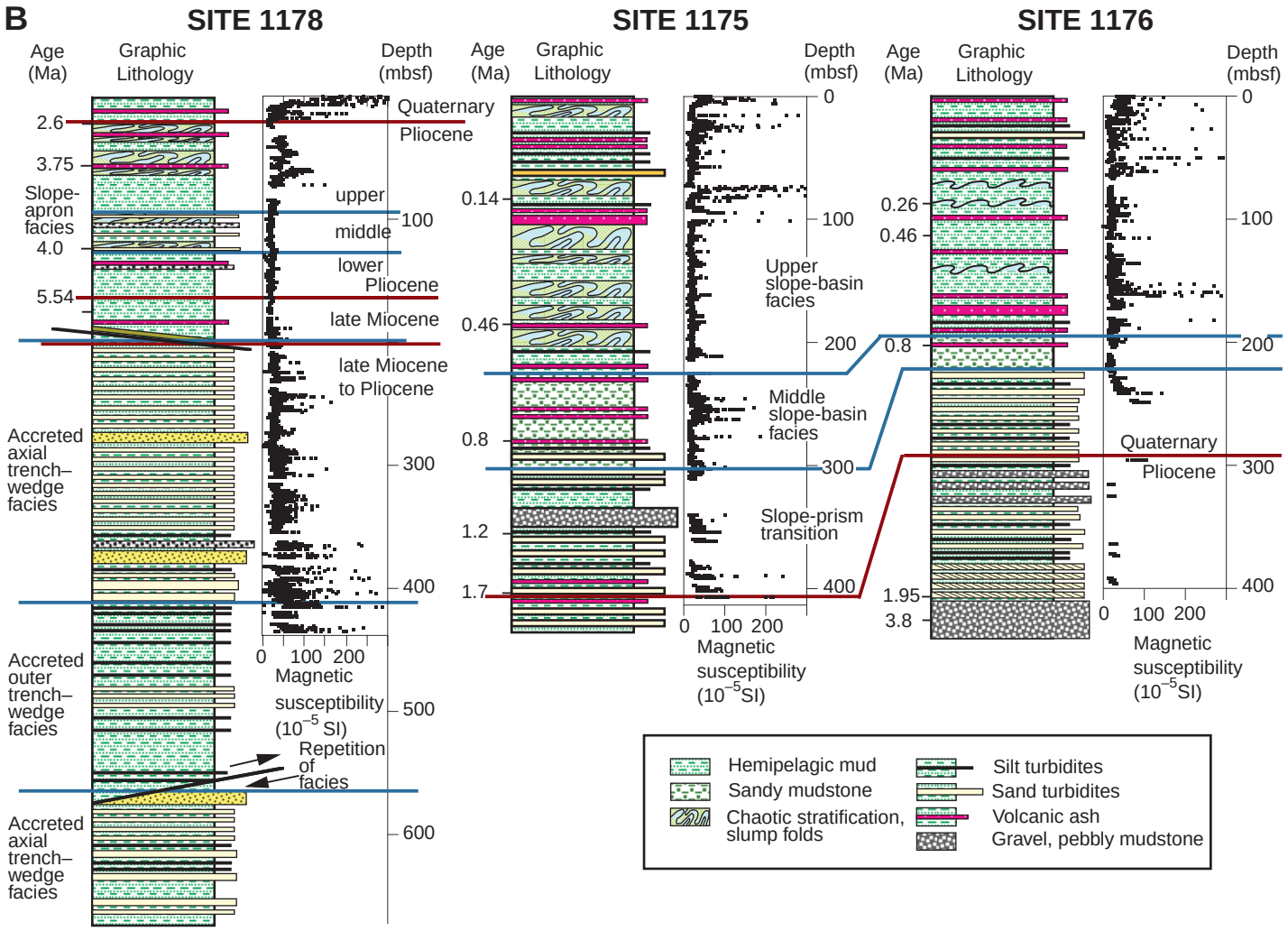
B
SITE 1178
SITE 1175
SITE 1176
Age (Ma)
Graphic Lithology
Depth (mbsf)
2.6
3.75
Slope-apron facies
4.0
5.54
Accreted axial trench–wedge facies
Accreted outer trench–wedge facies
Repetition of facies
Accreted axial trench–wedge facies
Quaternary
Pliocene
upper
middle
lower
Pliocene
late Miocene
late Miocene to Pliocene
0 100 200
Magnetic susceptibility (10^{-5} SI)
0.14
0.46
0.8
1.2
1.7
Upper slope-basin facies
Middle slope-basin facies
Slope-prism transition
0.26
0.46
0.8
1.95
3.8
Quaternary
Pliocene
0
100
200
300
400
500
600
Hemipelagic mud
Sandy mudstone
Chaotic stratification, slump folds
Silt turbidites
Sand turbidites
Volcanic ash
Gravel, pebbly mudstone

Figure 8B

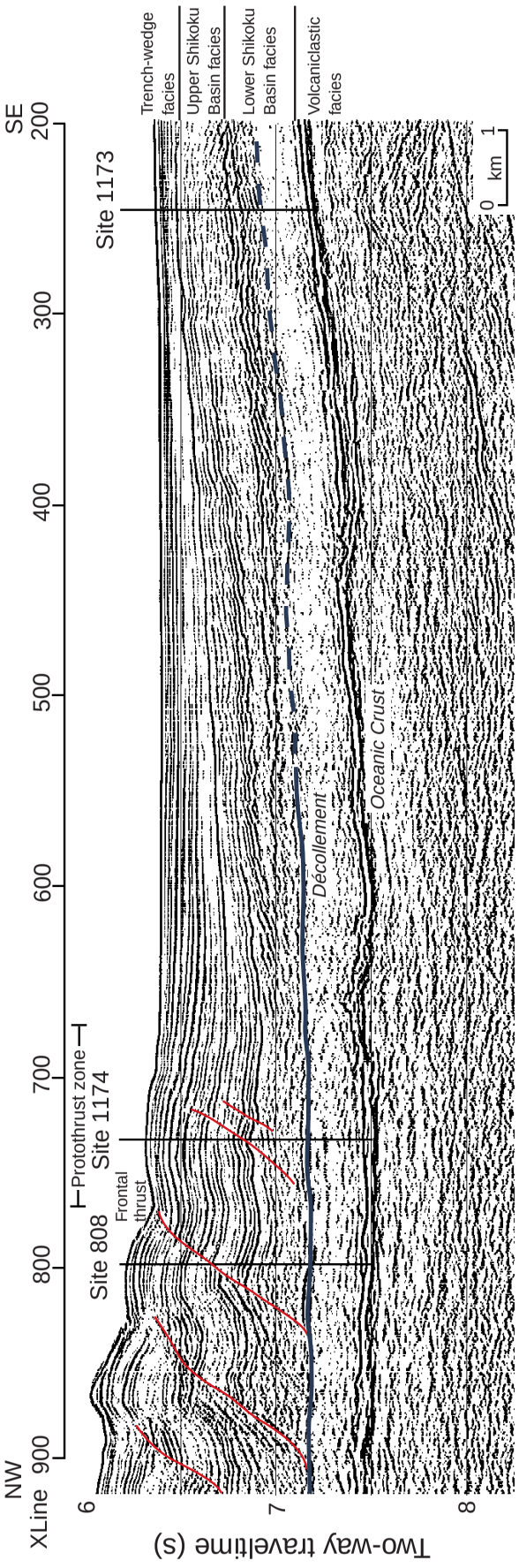
NW
SE
XLine 900
800
700
600
500
400
300
200
Site 808
Site 1174
Site 1173
Frontal thrust
Protothrust zone
Trench-wedge facies
Upper Shikoku Basin facies
Lower Shikoku Basin facies
Volcaniclastic facies
Décollement
Oceanic Crust
0 km 1
Two-way traveltime (s)
6
7
8

Figure 9

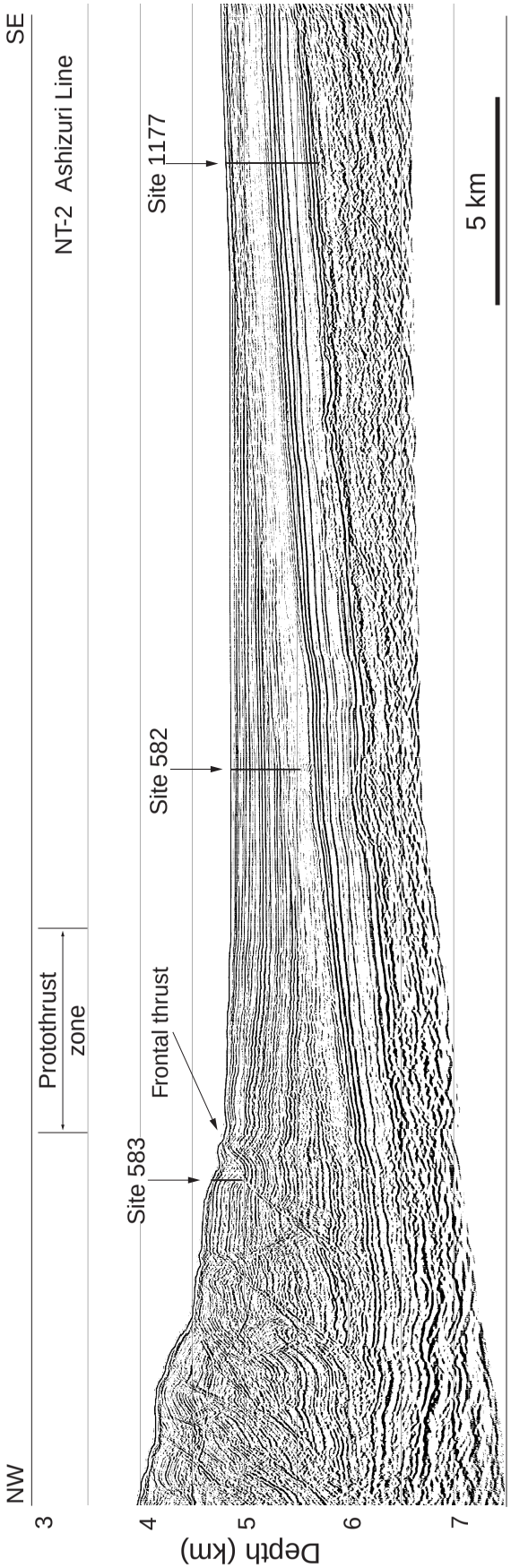
NW
SE
NT-2 Ashizuri Line
Protothrust zone
Frontal thrust
Site 583
Site 582
Site 1177
5 km
Depth (km)
3
4
5
6
7

Figure 10

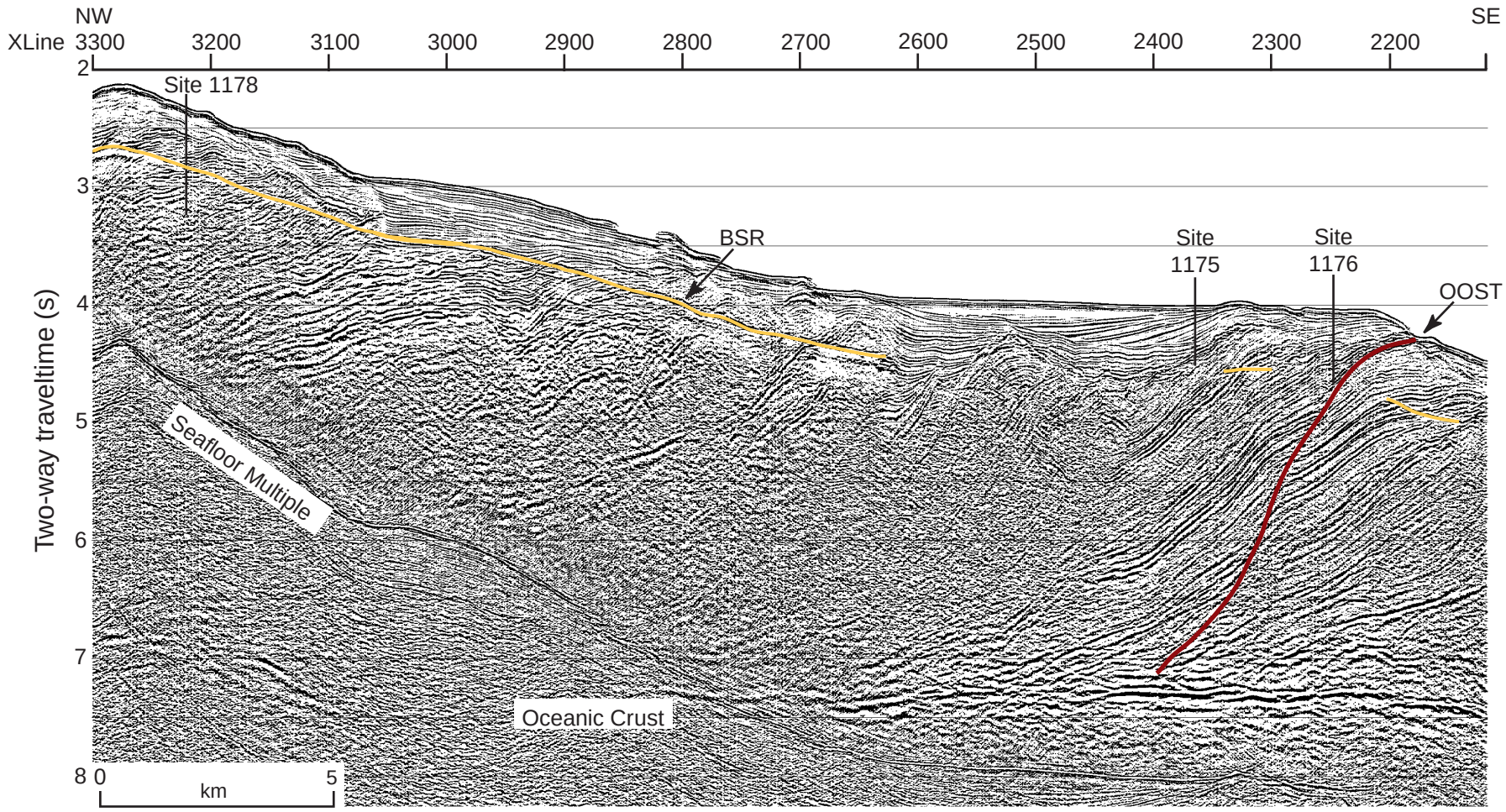
NW
SE
XLine
3300
3200
3100
3000
2900
2800
2700
2600
2500
2400
2300
2200
Site 1178
BSR
Site 1175
Site 1176
OOST
Seafloor Multiple
Oceanic Crust
Two-way traveltime (s)
2
3
4
5
6
7
8
0
km
5

Figure 11

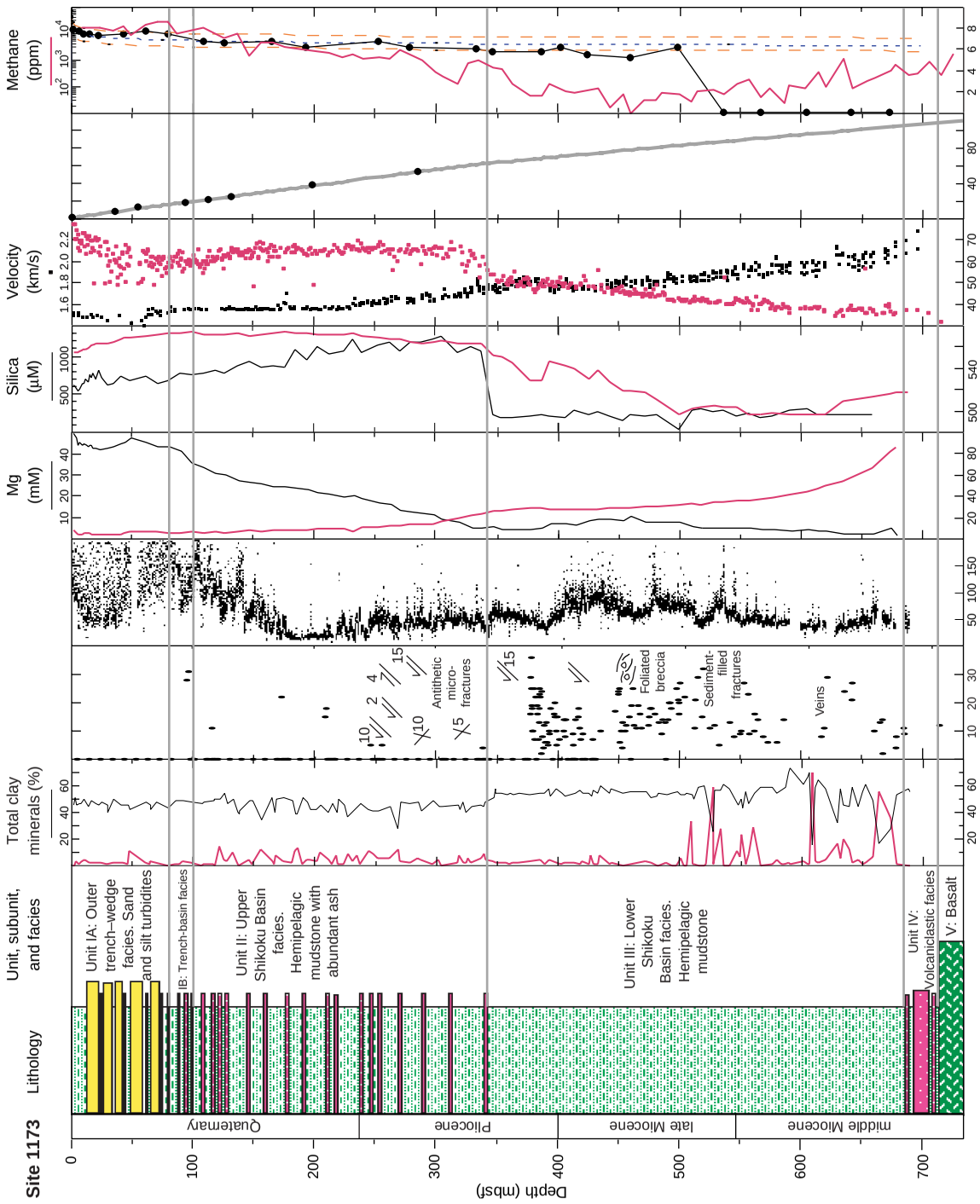
Site 1173
Lithology
Unit, subunit, and facies
Total clay minerals (%)
Bedding dip angle (°)
Magnetic susceptibility (10⁻⁵ SI)
Mg (mM)
Silica (µM)
Velocity (km/s)
Methane (ppm)
CaCO3 (wt%)
Ca+2 (mM)
Cl (mM)
Porosity (%)
Temperature (°C)
Total bacteria (log10 cells/cm3)
Depth (mbsf)
Quaternary
Pliocene
late Miocene
middle Miocene
Unit IA: Outer trench–wedge facies. Sand and silt turbidites
IB: Trench-basin facies
Unit II: Upper Shikoku Basin facies. Hemipelagic mudstone with abundant ash
Unit III: Lower Shikoku Basin facies. Hemipelagic mudstone
Unit IV: Volcaniclastic facies
V: Basalt
Antithetic micro-fractures
Foliated breccia
Sediment-filled fractures
Veins

Figure 12

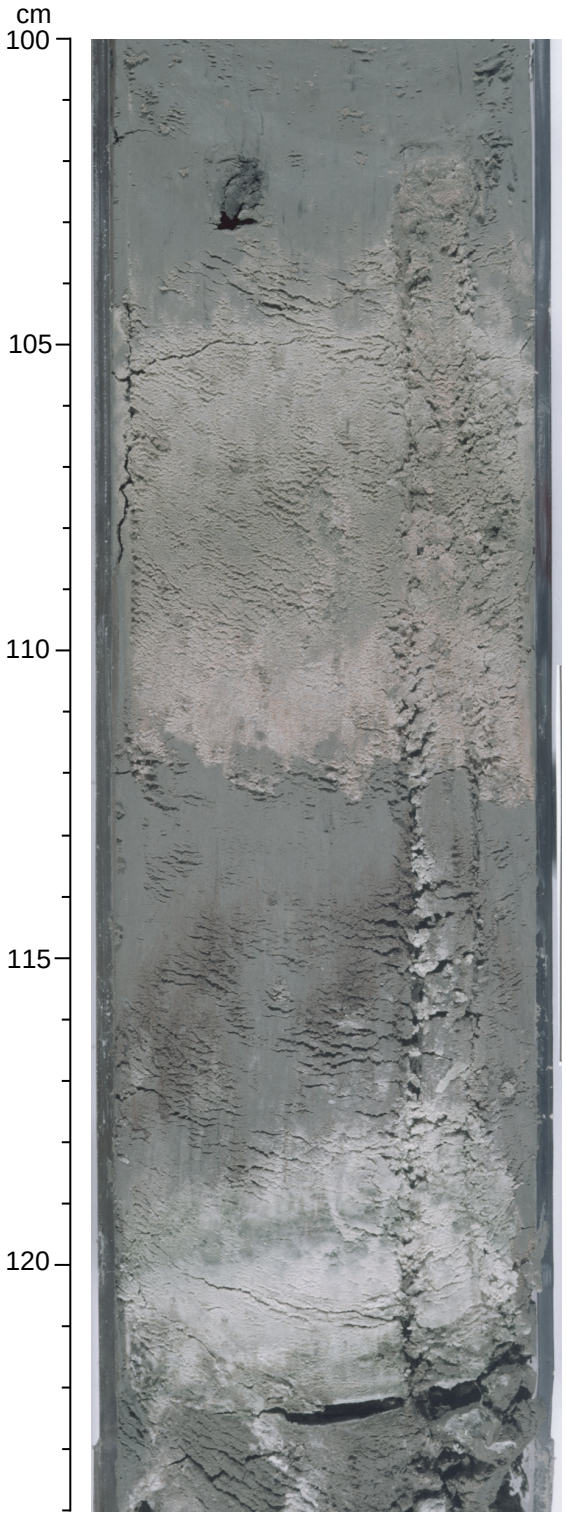

Figure 13

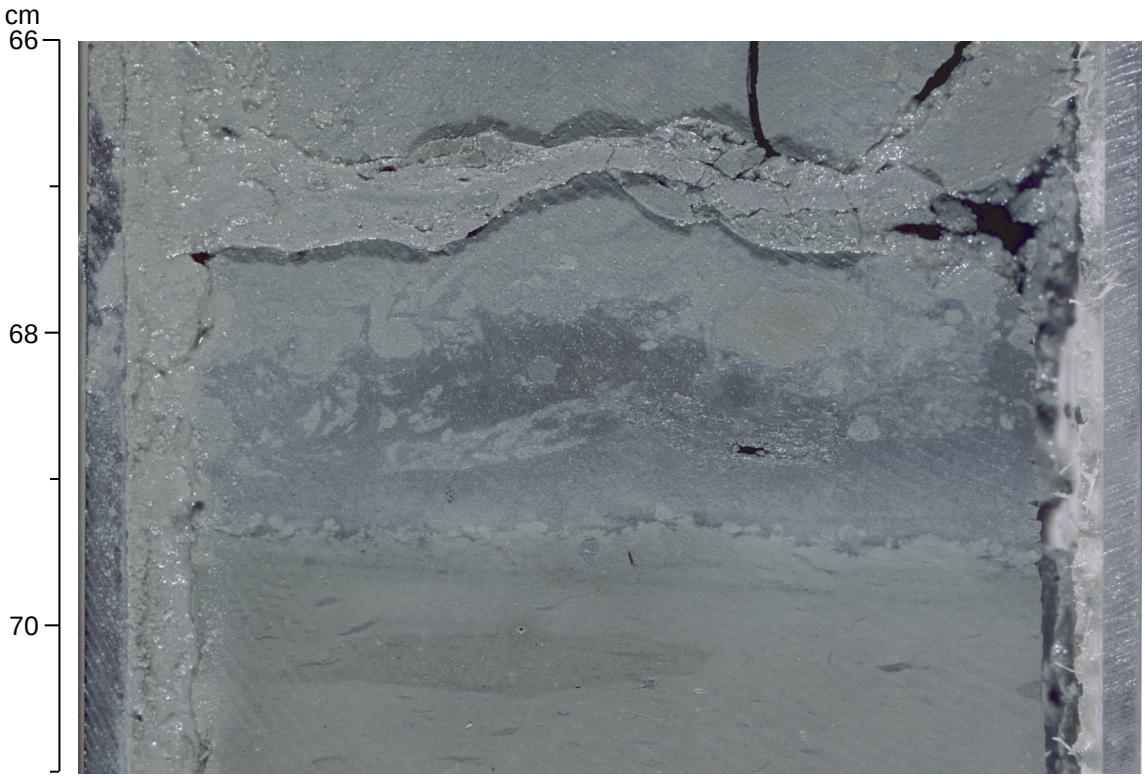

Figure 14

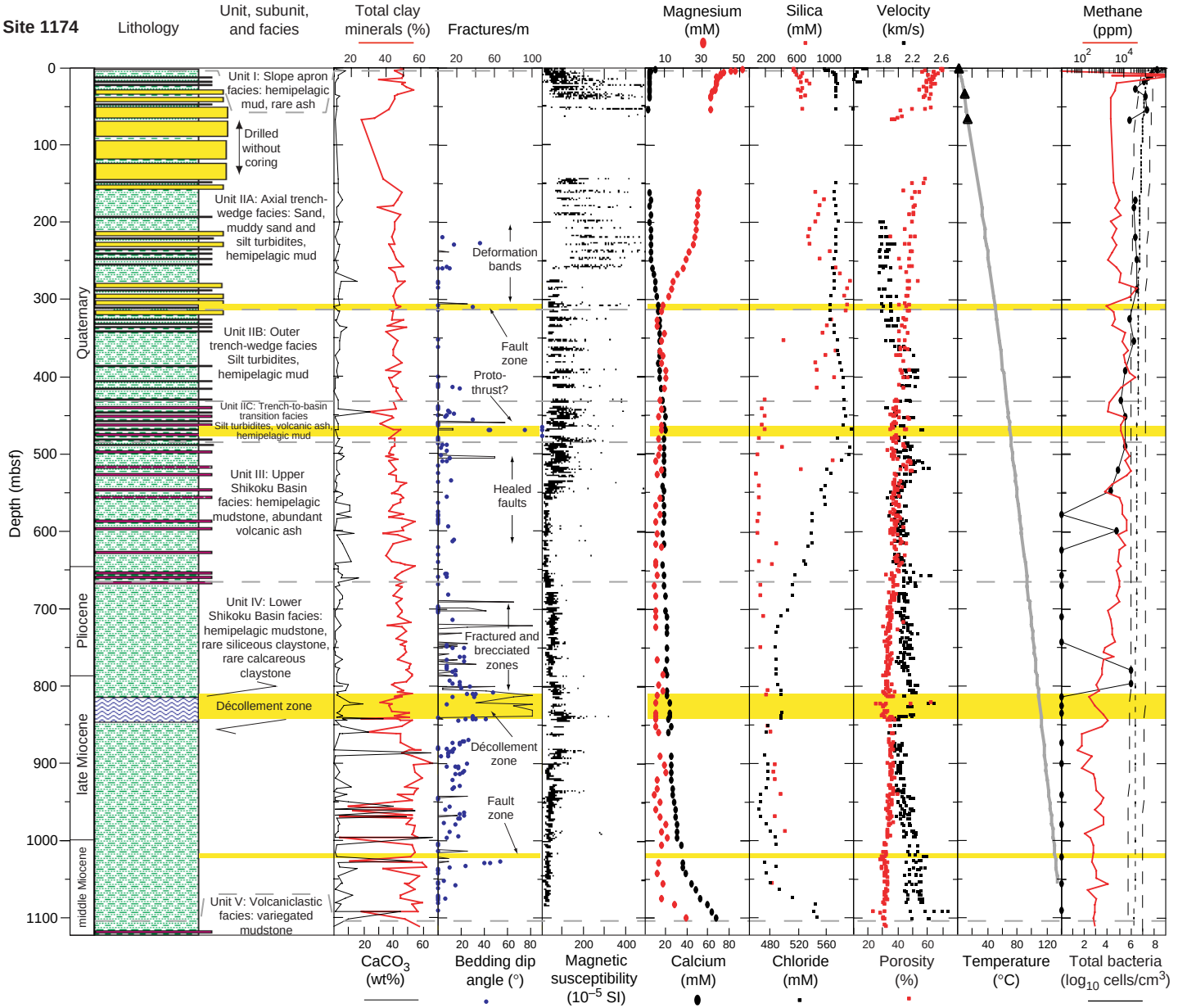
Site 1174
Lithology
Unit, subunit, and facies
Total clay minerals (%)
Fractures/m
Magnesium (mM)
Silica (mM)
Velocity (km/s)
Methane (ppm)
Depth (mbsf)
Quaternary
Pliocene
late Miocene
middle Miocene
Unit I: Slope apron facies: hemipelagic mud, rare ash
Drilled without coring
Unit IIA: Axial trench-wedge facies: Sand, muddy sand and silt turbidites, hemipelagic mud
Unit IIB: Outer trench-wedge facies Silt turbidites, hemipelagic mud
Unit IIC: Trench-to-basin transition facies Silt turbidites, volcanic ash, hemipelagic mud
Unit III: Upper Shikoku Basin facies: hemipelagic mudstone, abundant volcanic ash
Unit IV: Lower Shikoku Basin facies: hemipelagic mudstone, rare siliceous claystone, rare calcareous claystone
Décollement zone
Unit V: Volcaniclastic facies: variegated mudstone
Deformation bands
Fault zone
Proto-thrust?
Healed faults
Fractured and brecciated zones
Décollement zone
Fault zone
CaCO3 (wt%)
Bedding dip angle (°)
Magnetic susceptibility (10−5 SI)
Calcium (mM)
Chloride (mM)
Porosity (%)
Temperature (°C)
Total bacteria (log10 cells/cm3)

Figure 15

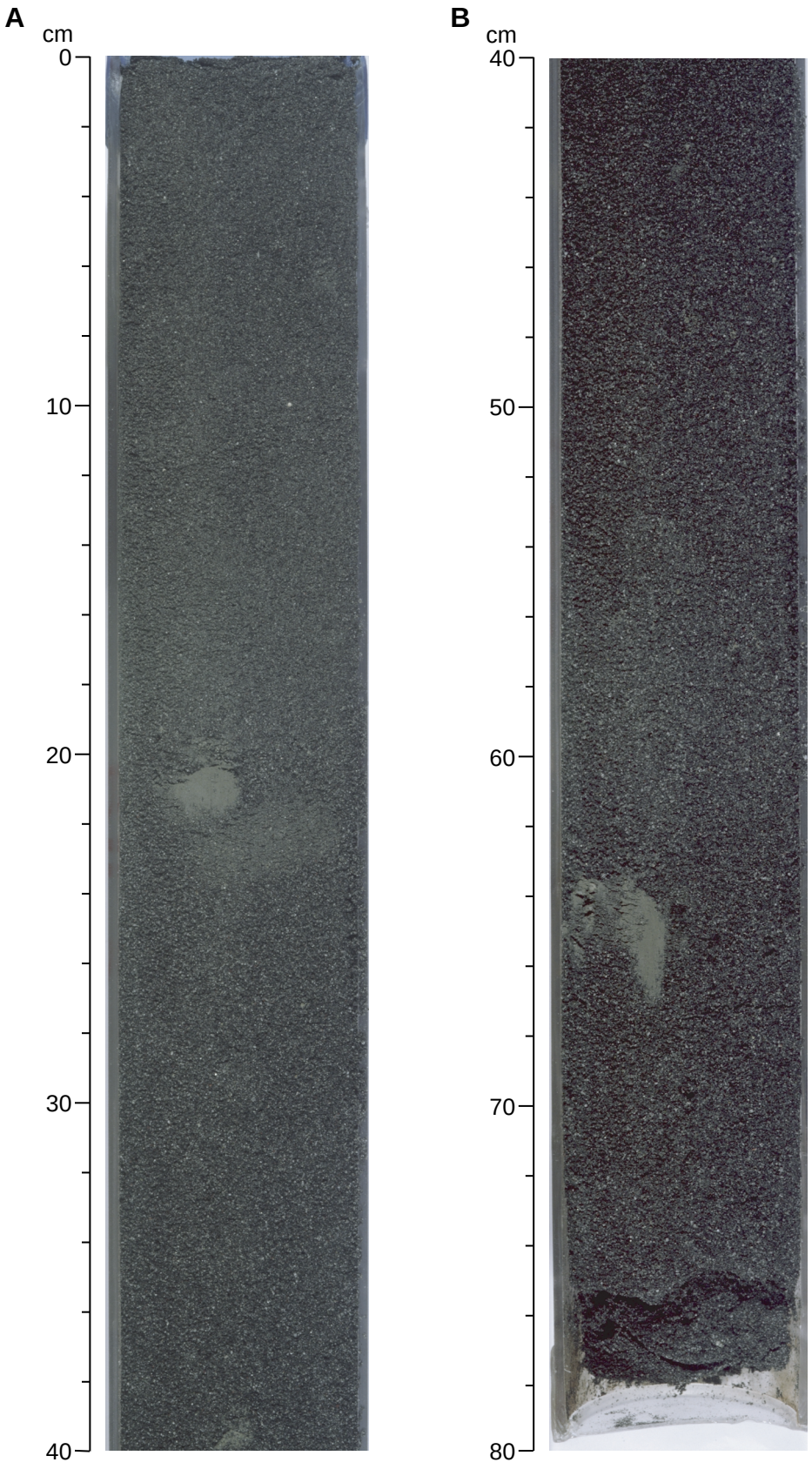

Figure 16

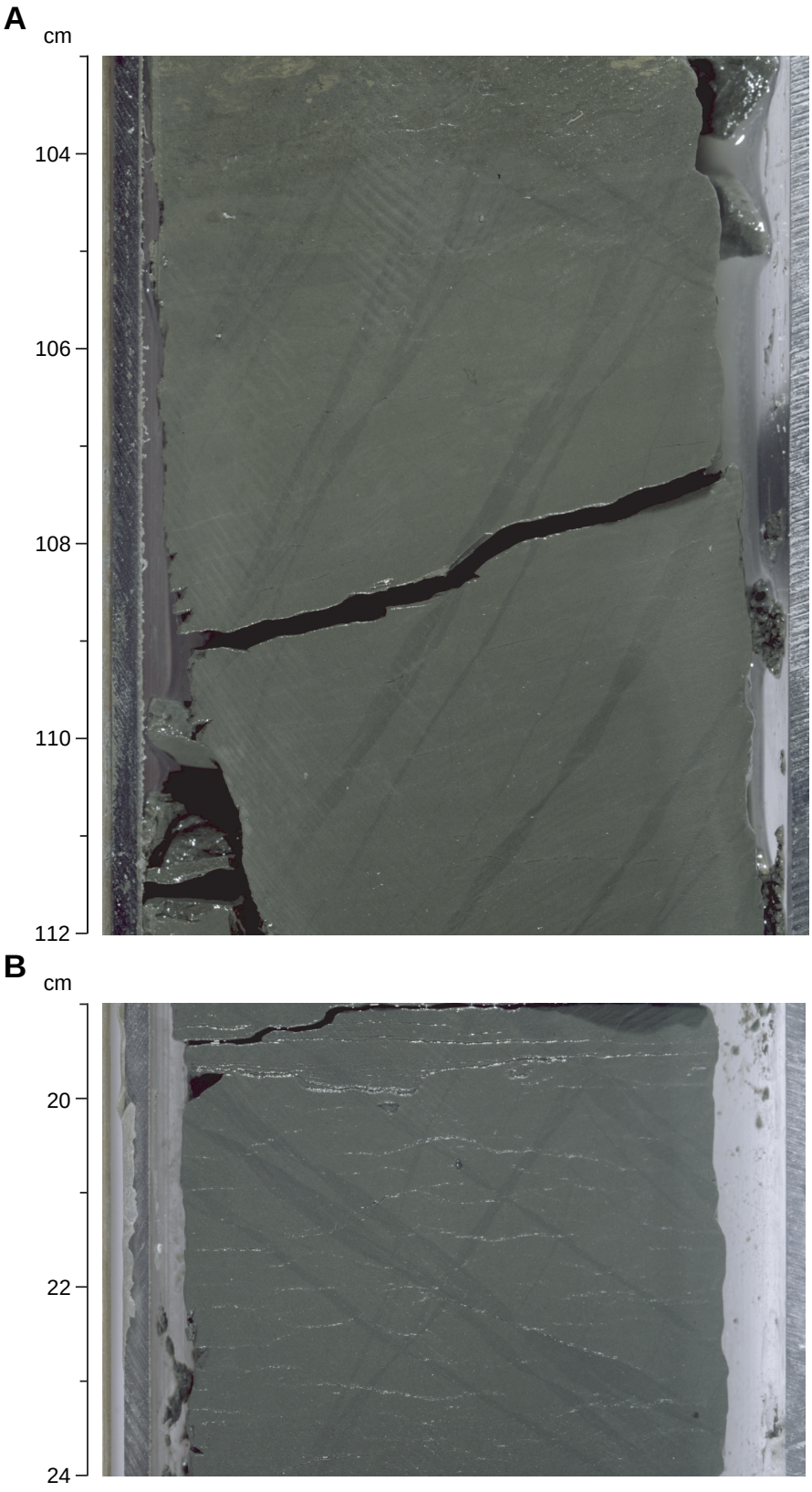

Figure 17

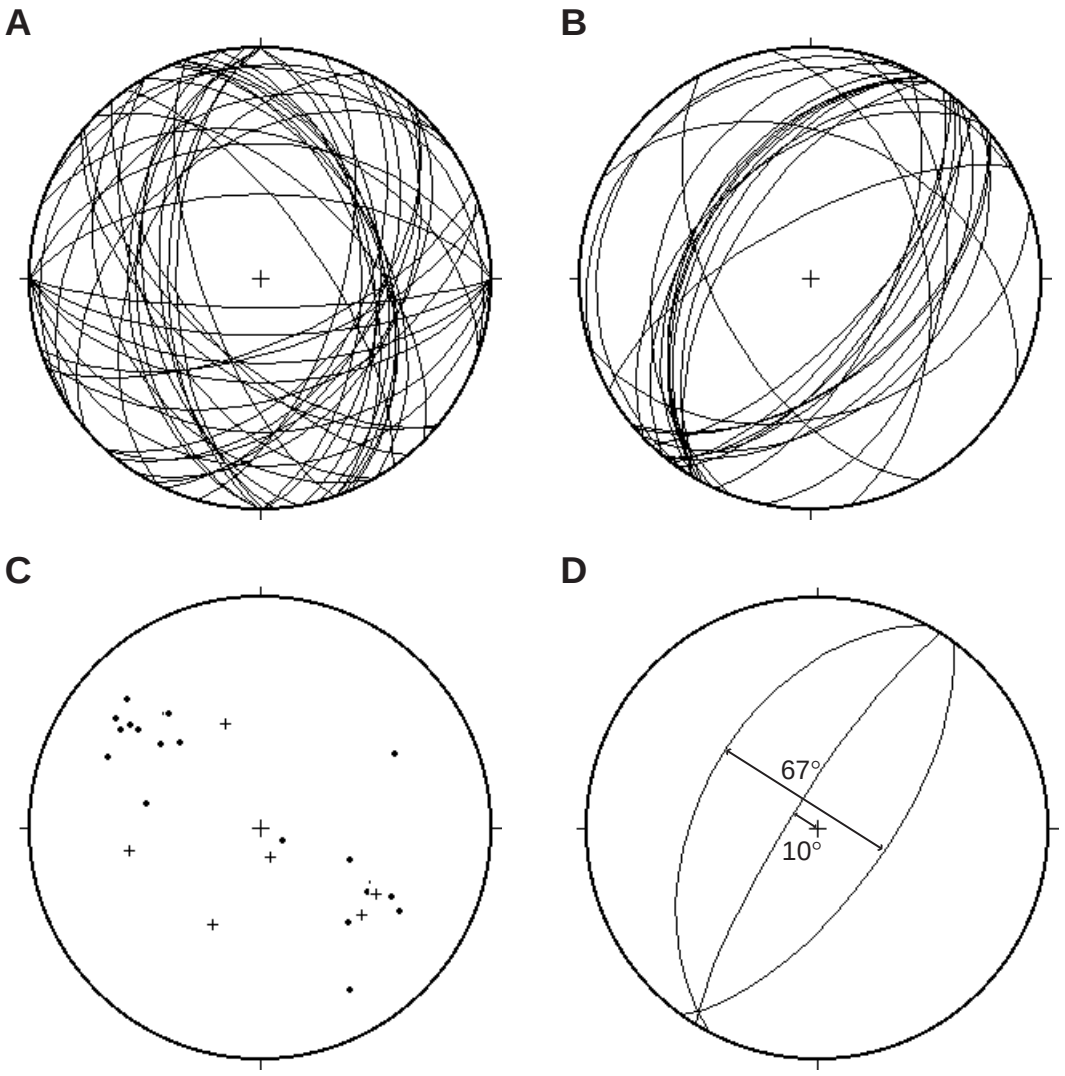

Figure 18

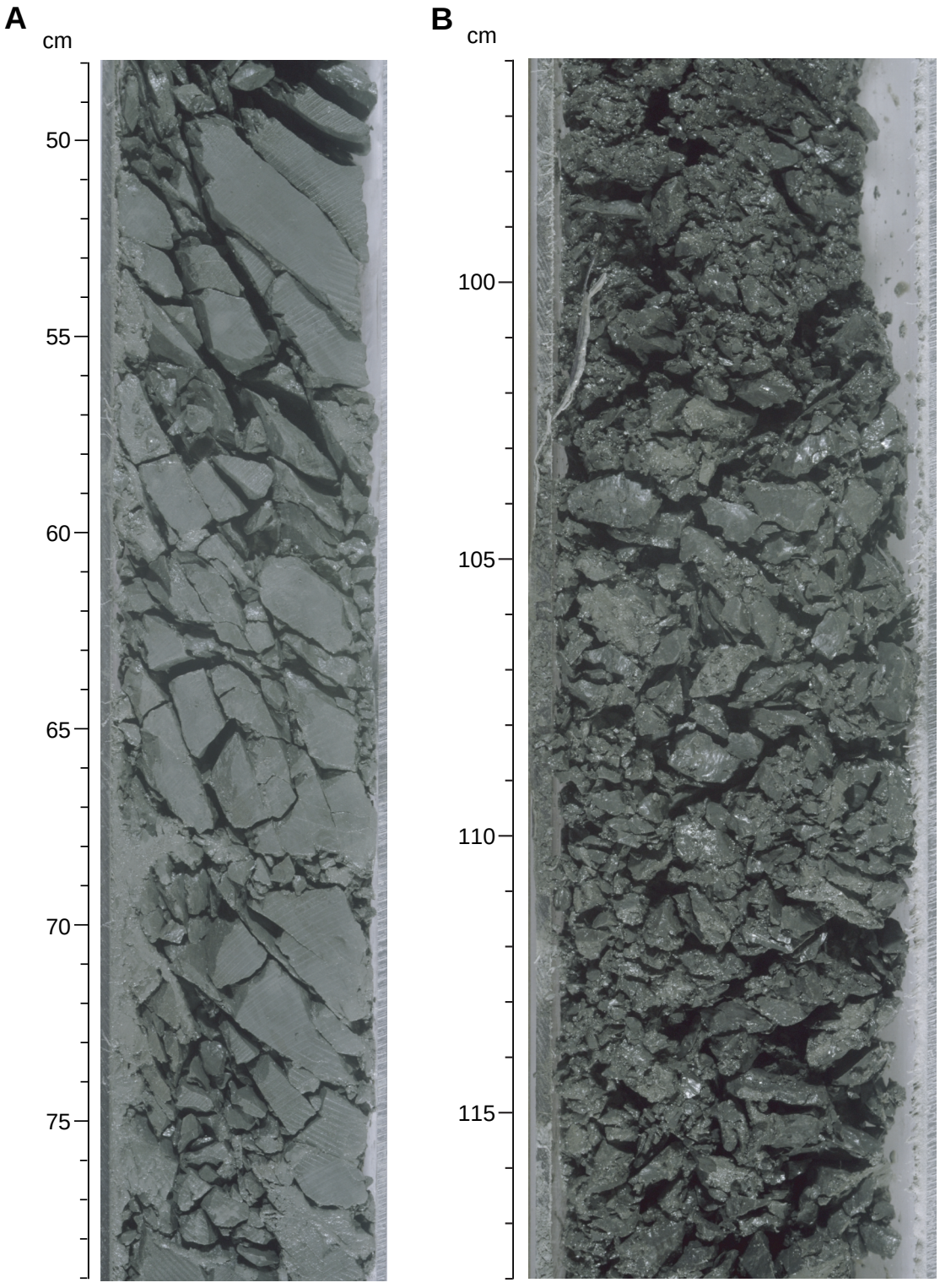

Figure 19

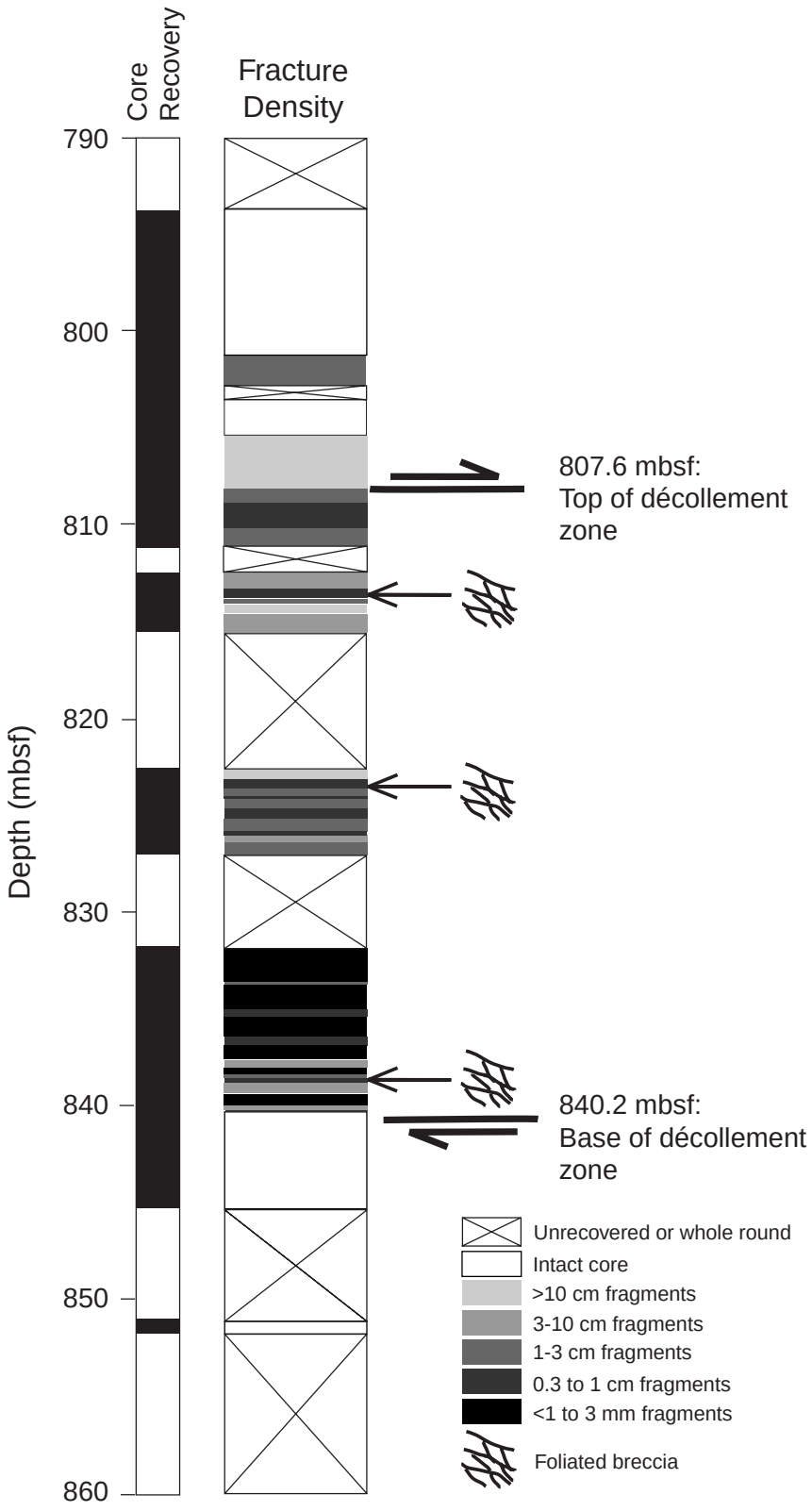
Core Recovery
Fracture Density
Depth (mbsf)
790
800
810
820
830
840
850
860
807.6 mbsf:
Top of décollement zone
840.2 mbsf:
Base of décollement zone
Unrecovered or whole round
Intact core
>10 cm fragments
3-10 cm fragments
1-3 cm fragments
0.3 to 1 cm fragments
<1 to 3 mm fragments
Foliated breccia

Figure 20

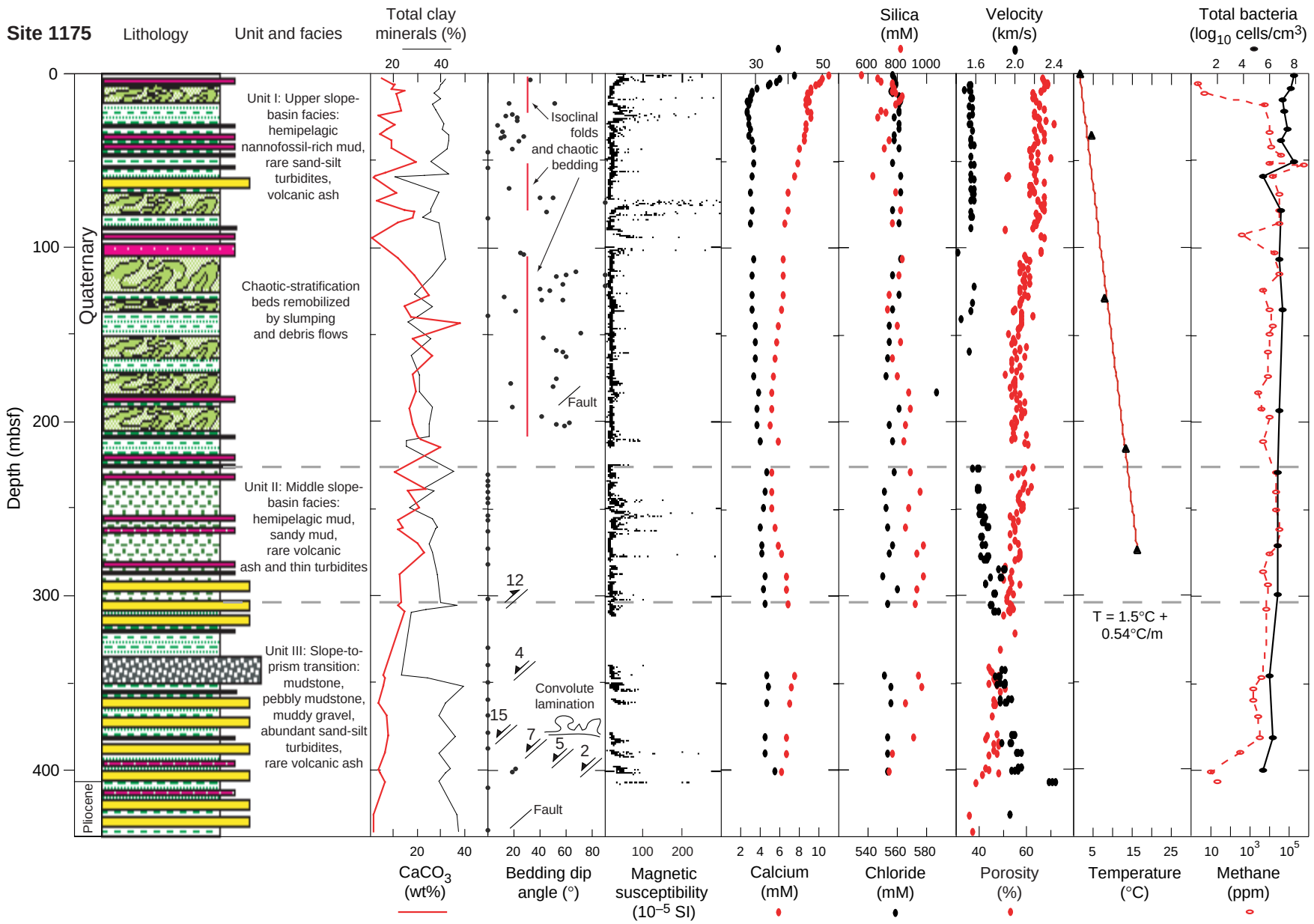
Site 1175
Lithology
Unit and facies
Total clay minerals (%)
Silica (mM)
Velocity (km/s)
Total bacteria (log10 cells/cm3)
Depth (mbsf)
Quaternary
Pliocene
Unit I: Upper slope-basin facies: hemipelagic nannofossil-rich mud, rare sand-silt turbidites, volcanic ash
Chaotic-stratification beds remobilized by slumping and debris flows
Unit II: Middle slope-basin facies: hemipelagic mud, sandy mud, rare volcanic ash and thin turbidites
Unit III: Slope-to-prism transition: mudstone, pebbly mudstone, muddy gravel, abundant sand-silt turbidites, rare volcanic ash
Isoclinal folds and chaotic bedding
Fault
Convolute lamination
Fault
T = 1.5°C + 0.54°C/m
CaCO3 (wt%)
Bedding dip angle (°)
Magnetic susceptibility (10−5 SI)
Calcium (mM)
Chloride (mM)
Porosity (%)
Temperature (°C)
Methane (ppm)

Figure 21

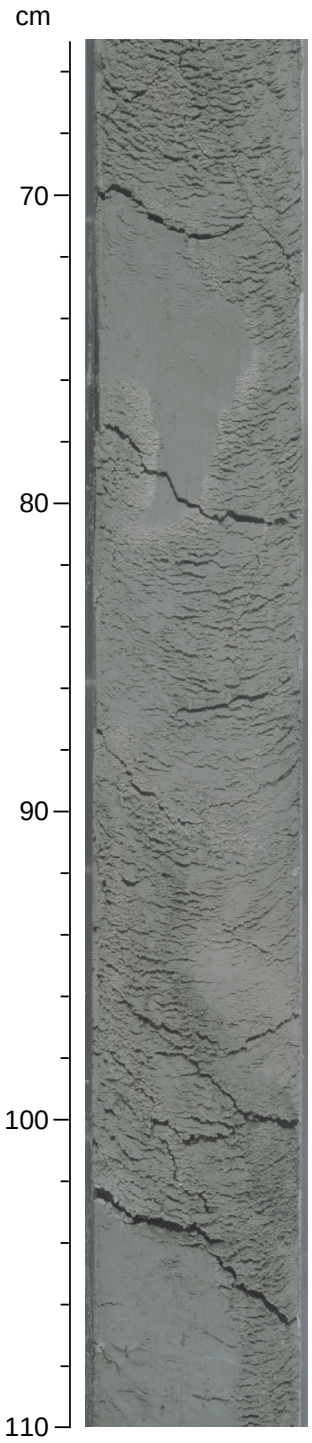

Figure 22

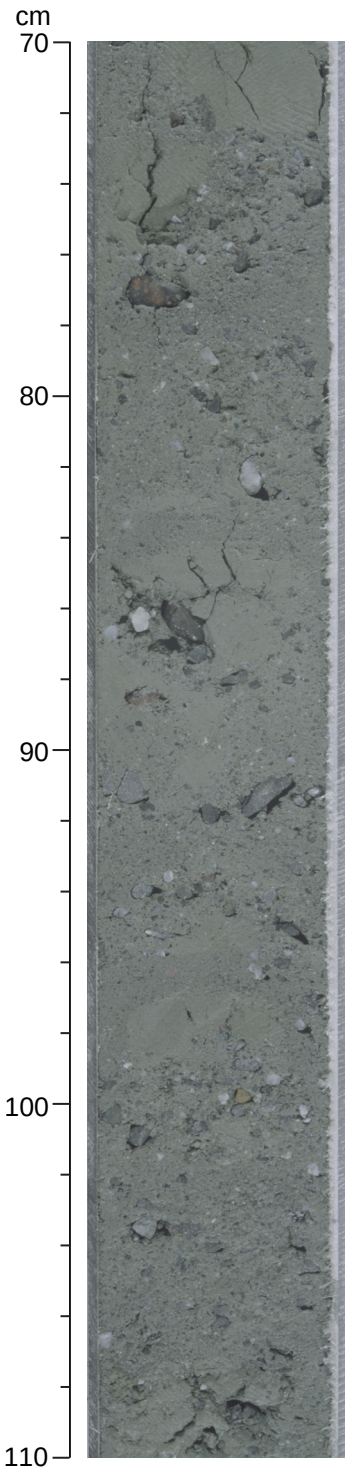

Figure 23

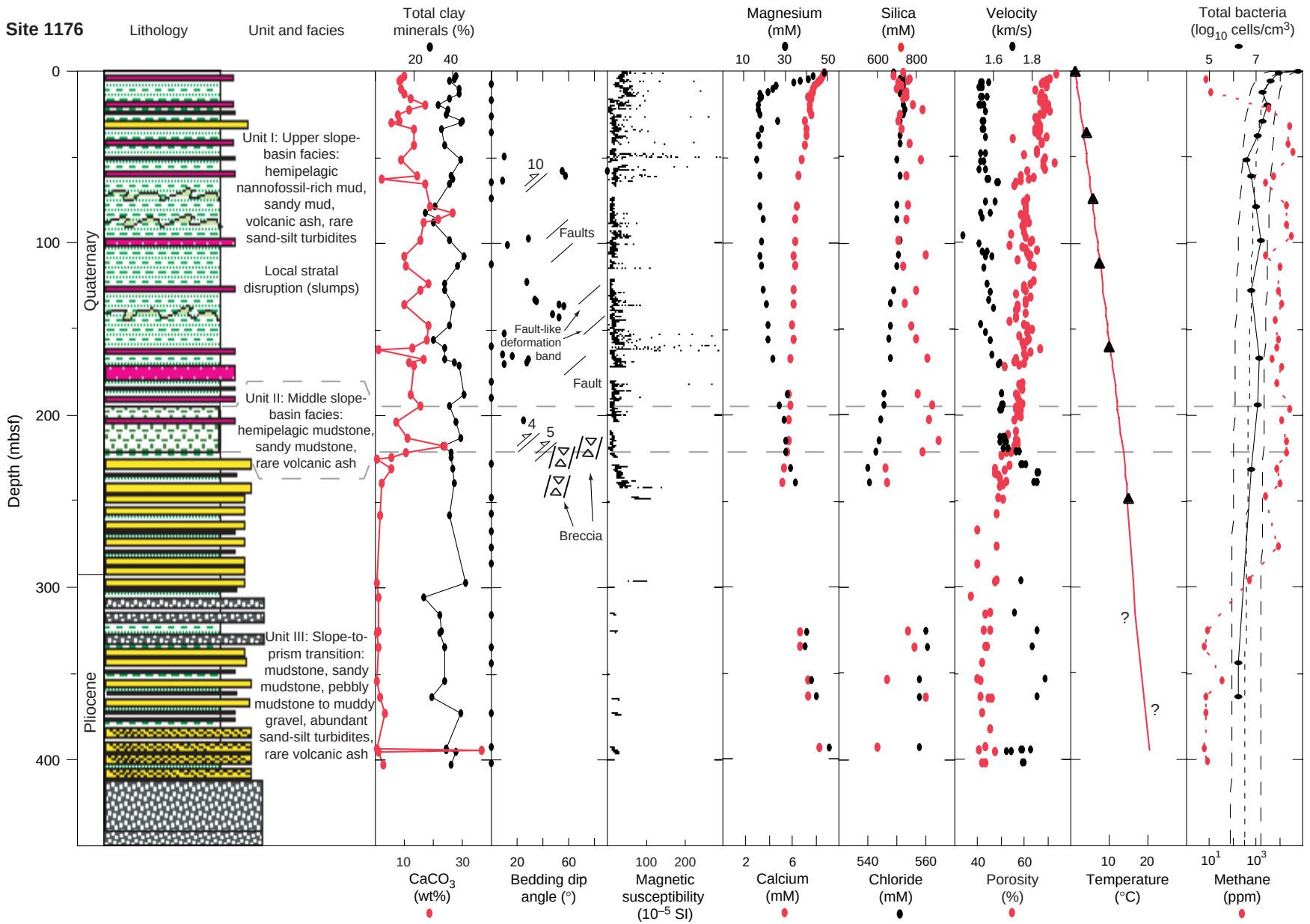
Site 1176
Lithology
Unit and facies
Total clay minerals (%)
Magnesium (mM)
Silica (mM)
Velocity (km/s)
Total bacteria (log10 cells/cm3)
Depth (mbsf)
Quaternary
Pliocene
Unit I: Upper slope-basin facies: hemipelagic nannofossil-rich mud, sandy mud, volcanic ash, rare sand-silt turbidites
Local stratal disruption (slumps)
Unit II: Middle slope-basin facies: hemipelagic mudstone, sandy mudstone, rare volcanic ash
Unit III: Slope-to-prism transition: mudstone, sandy mudstone, pebbly mudstone to muddy gravel, abundant sand-silt turbidites, rare volcanic ash
Faults
Fault-like deformation band
Fault
Breccia
CaCO3 (wt%)
Bedding dip angle (°)
Magnetic susceptibility (10−5 SI)
Calcium (mM)
Chloride (mM)
Porosity (%)
Temperature (°C)
Methane (ppm)

Figure 24

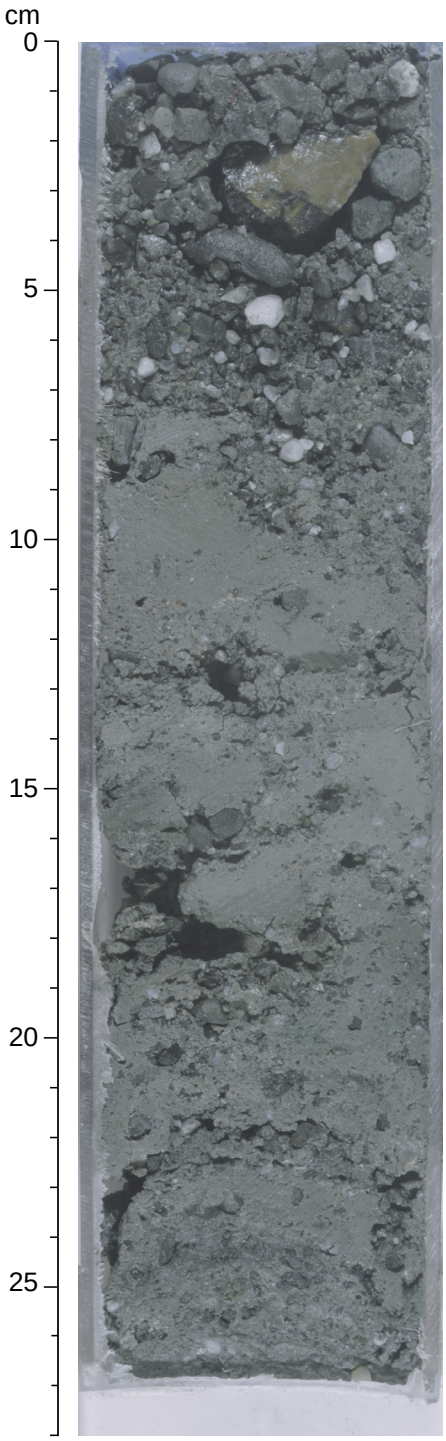

Figure 25

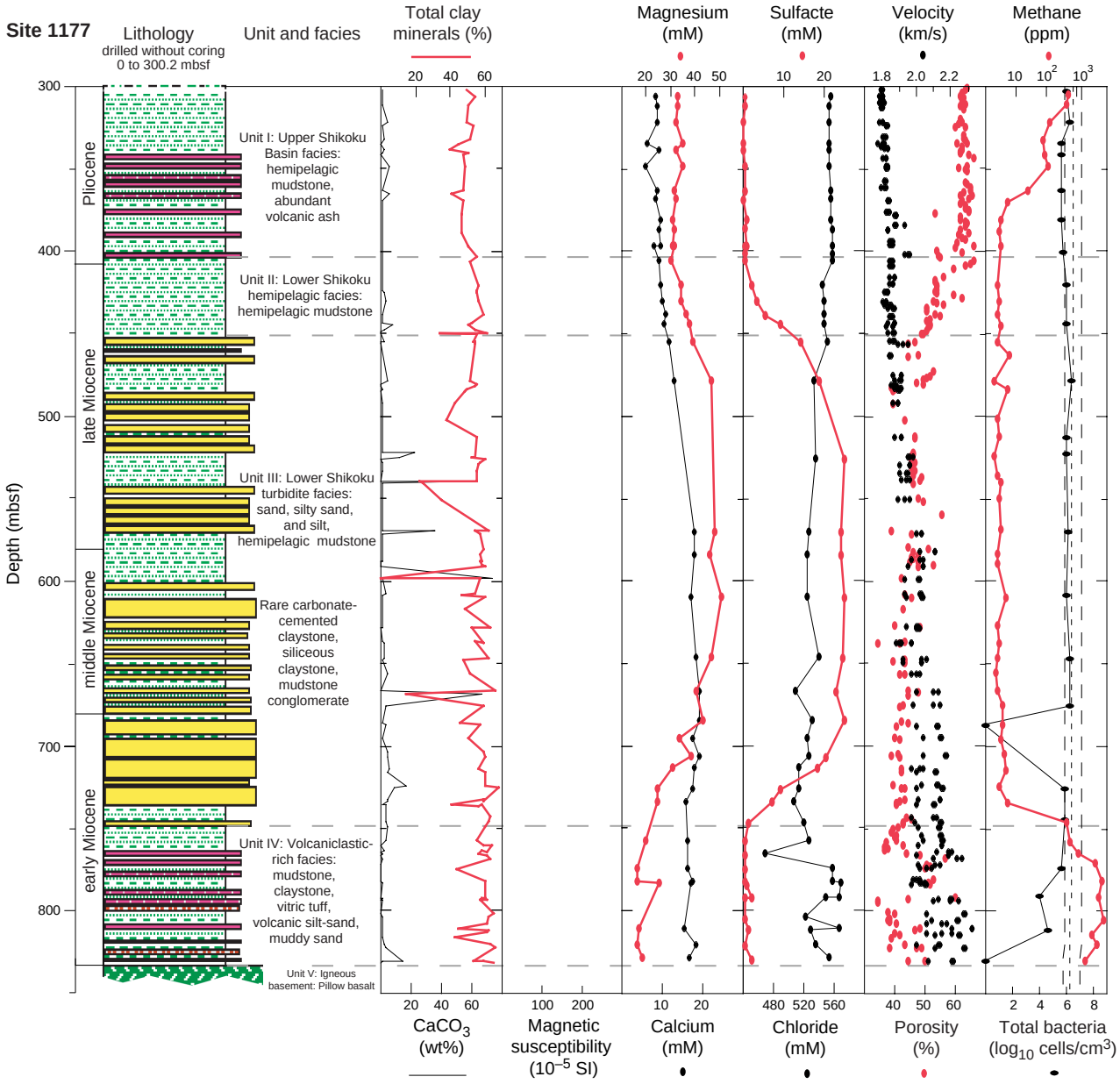
Site 1177
Lithology
drilled without coring
0 to 300.2 mbsf
Unit and facies
Total clay minerals (%)
Magnesium (mM)
Sulfacte (mM)
Velocity (km/s)
Methane (ppm)
Depth (mbsf)
Pliocene
late Miocene
middle Miocene
early Miocene
Unit I: Upper Shikoku Basin facies: hemipelagic mudstone, abundant volcanic ash
Unit II: Lower Shikoku hemipelagic facies: hemipelagic mudstone
Unit III: Lower Shikoku turbidite facies: sand, silty sand, and silt, hemipelagic mudstone
Rare carbonate-cemented claystone, siliceous claystone, mudstone conglomerate
Unit IV: Volcaniclastic-rich facies: mudstone, claystone, vitric tuff, volcanic silt-sand, muddy sand
Unit V: Igneous basement: Pillow basalt
CaCO3 (wt%)
Magnetic susceptibility (10−5 SI)
Calcium (mM)
Chloride (mM)
Porosity (%)
Total bacteria (log10 cells/cm3)

Figure 26

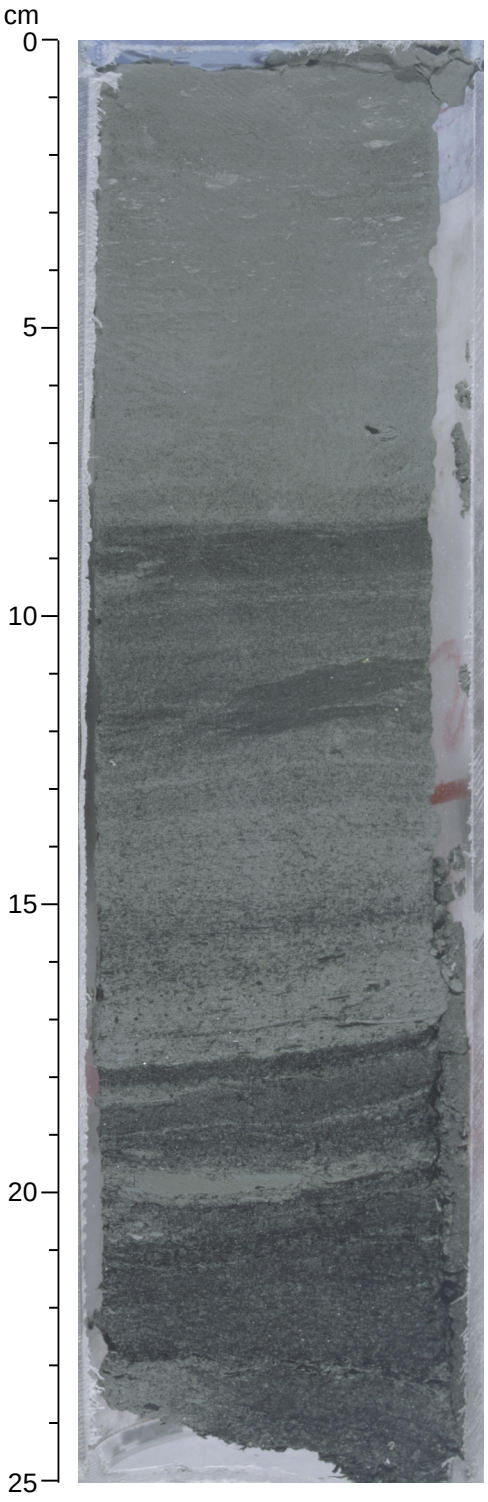

Figure 27

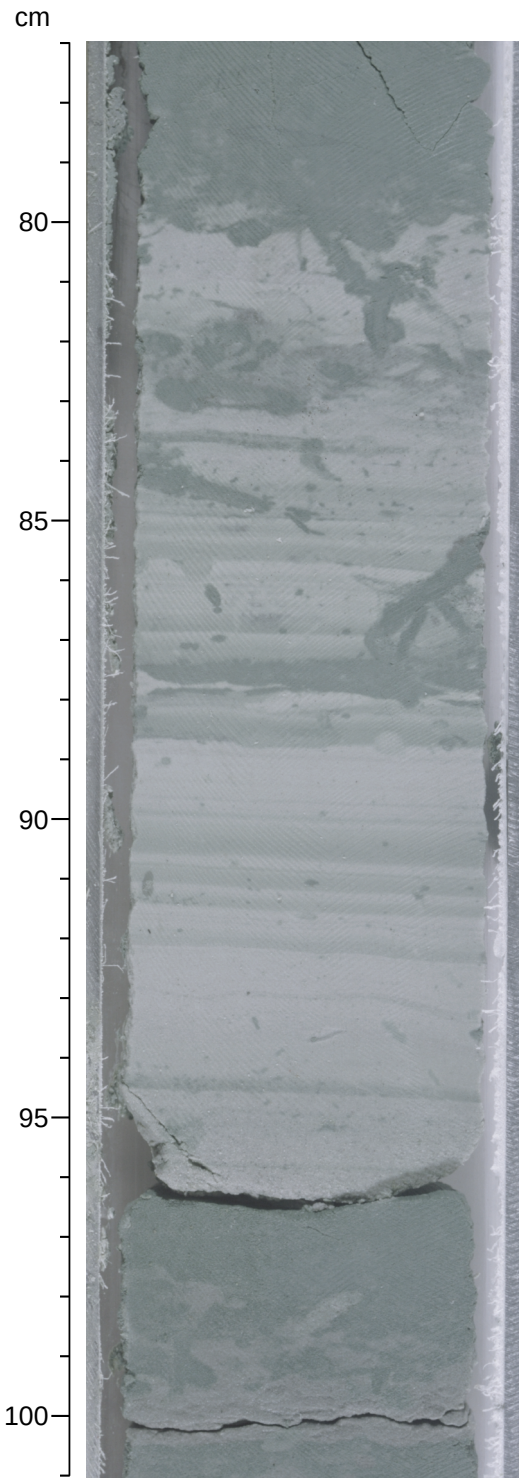

Figure 28

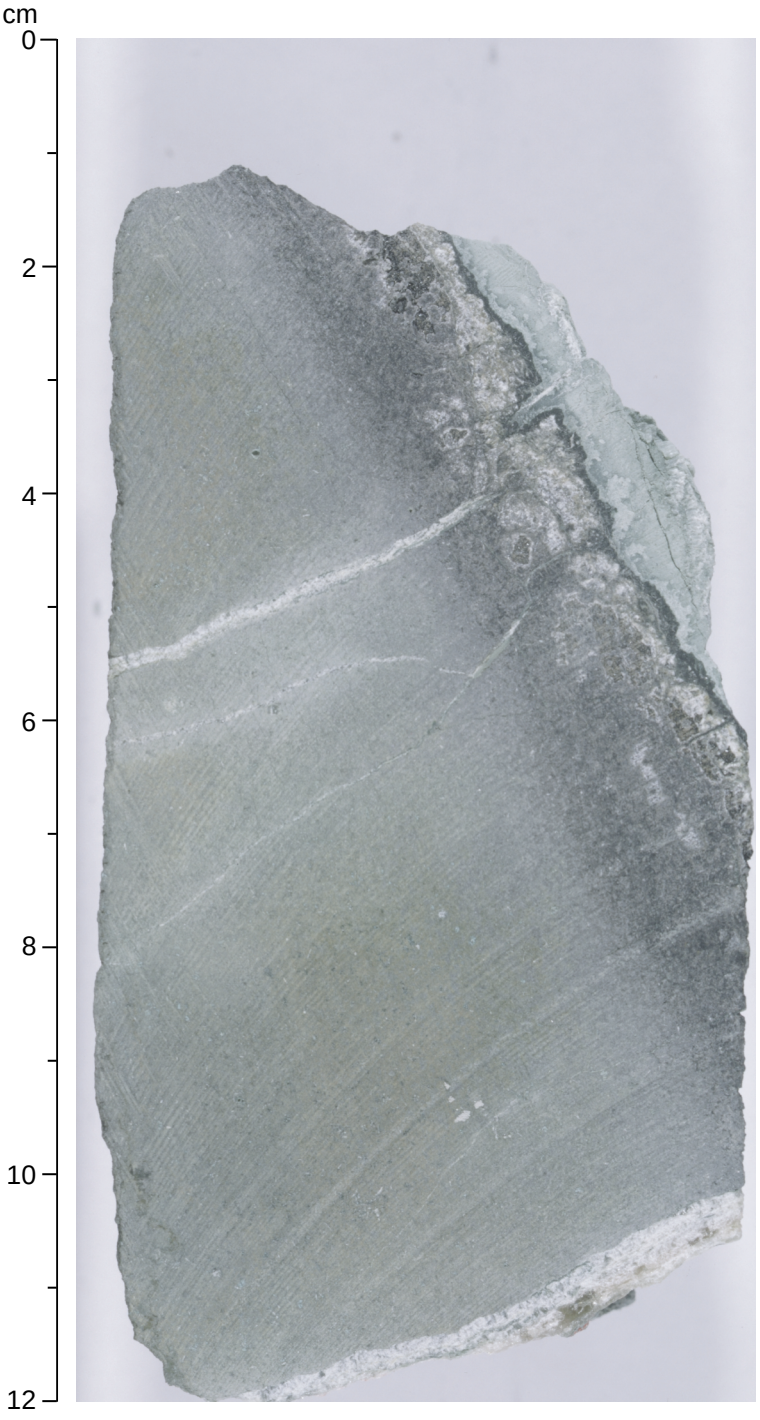

Figure 29

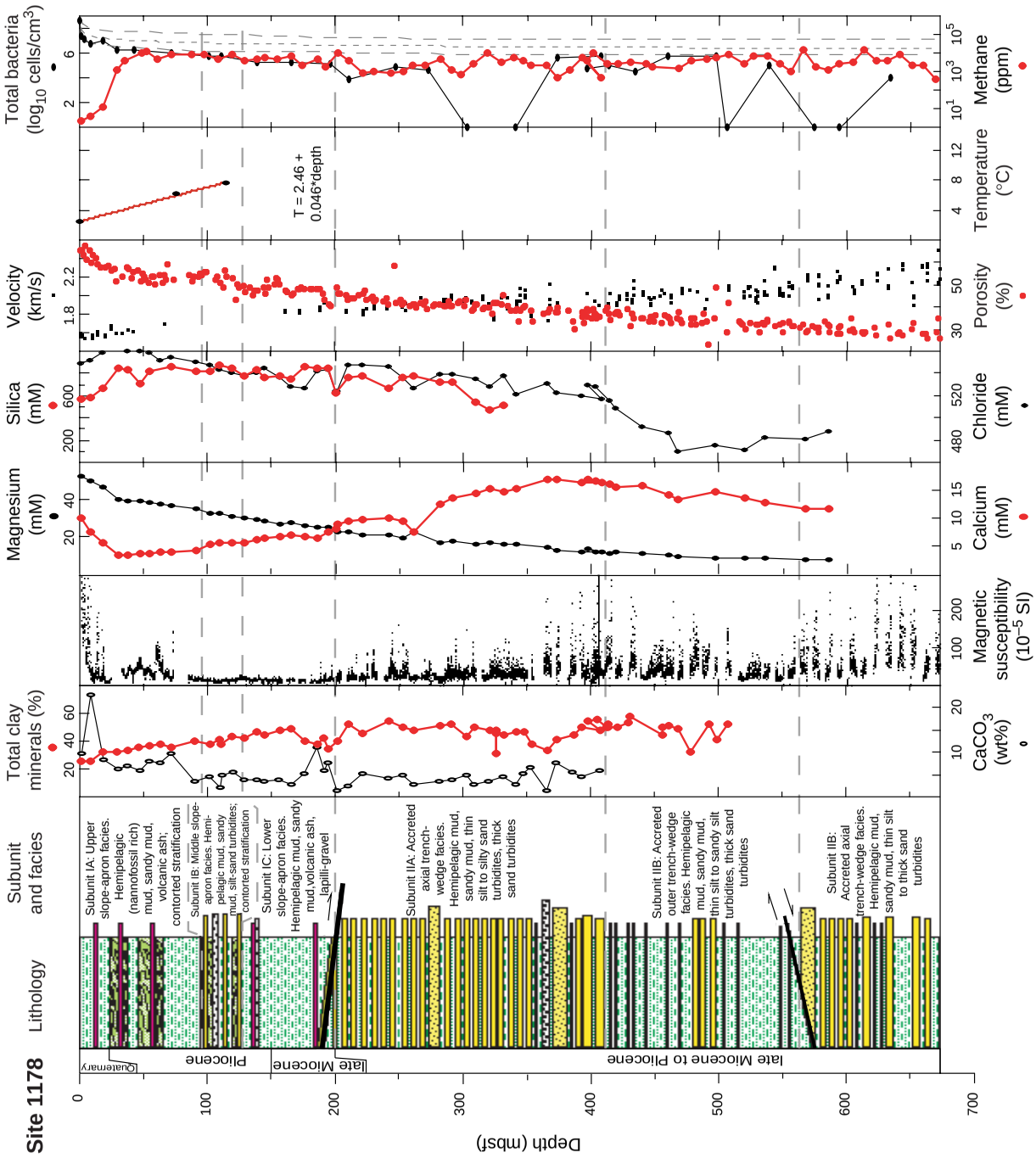
Site 1178
Lithology
Subunit and facies
Total clay minerals (%)
Magnesium (mM)
Silica (mM)
Velocity (km/s)
Total bacteria (log10 cells/cm3)
Magnetic susceptibility (10−5 SI)
Calcium (mM)
Chloride (mM)
Porosity (%)
Temperature (°C)
Methane (ppm)
CaCO3 (wt%)
T = 2.46 + 0.046*depth
Subunit IA: Upper slope-apron facies. Hemipelagic (nannofossil rich) mud, sandy mud, volcanic ash; contorted stratification
Subunit IB: Middle slope-apron facies. Hemipelagic mud, sandy mud, silt-sand turbidites; contorted stratification
Subunit IC: Lower slope-apron facies. Hemipelagic mud, sandy mud,volcanic ash, lapilli-gravel
Subunit IIA: Accreted axial trench-wedge facies. Hemipelagic mud, sandy mud, thin silt to silty sand turbidites, thick sand turbidites
Subunit IIB: Accreted outer trench-wedge facies. Hemipelagic mud, sandy mud, thin silt to sandy silt turbidites, thick sand turbidites
Subunit IIB: Accreted axial trench-wedge facies. Hemipelagic mud, sandy mud, thin silt to thick sand turbidites
Quaternary
Pliocene
late Miocene
late Miocene to Pliocene
Depth (mbsf)

Figure 30

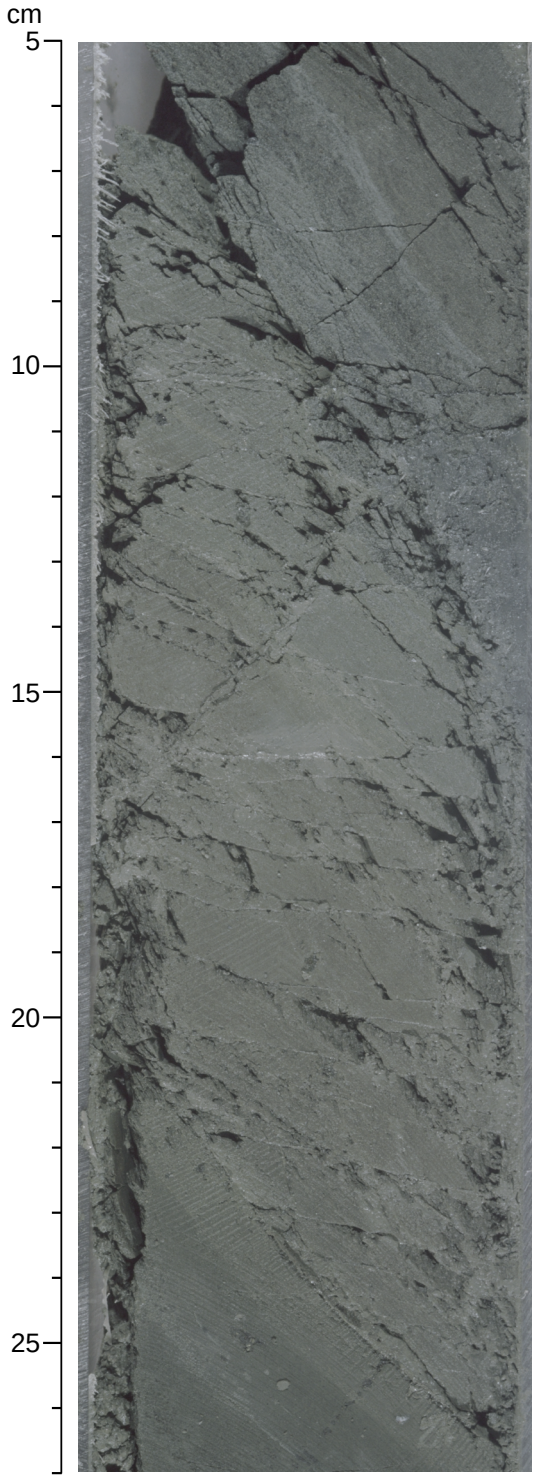

Figure 31

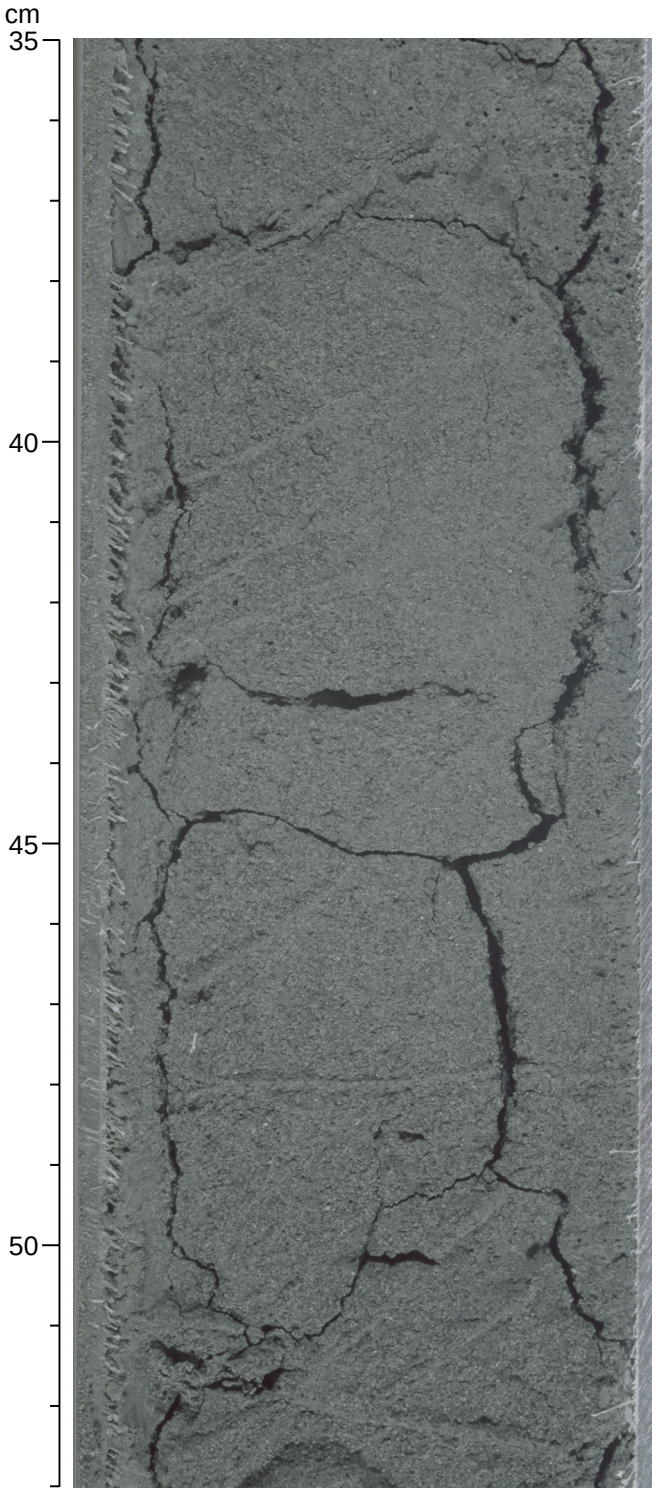

Figure 32

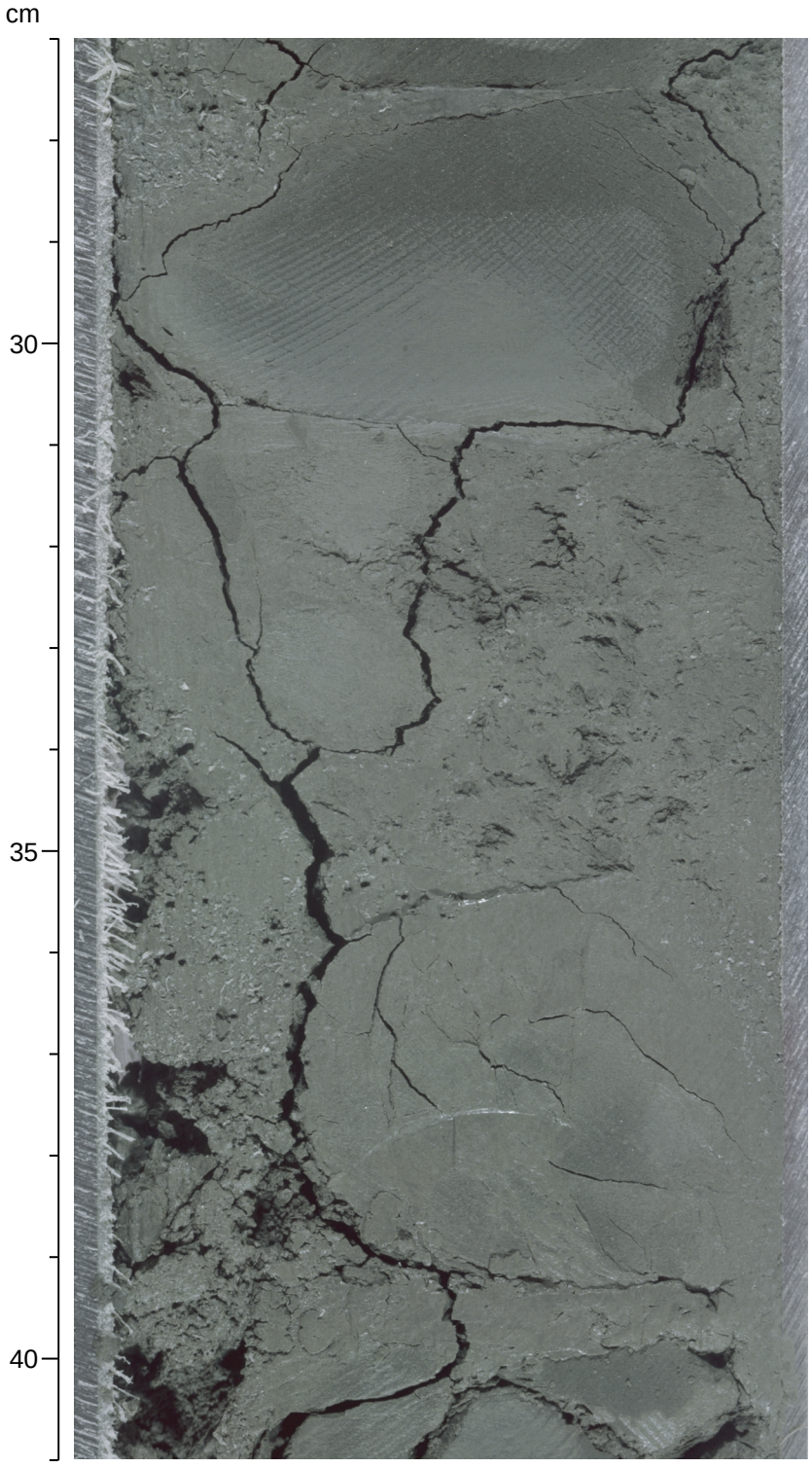

Figure 33

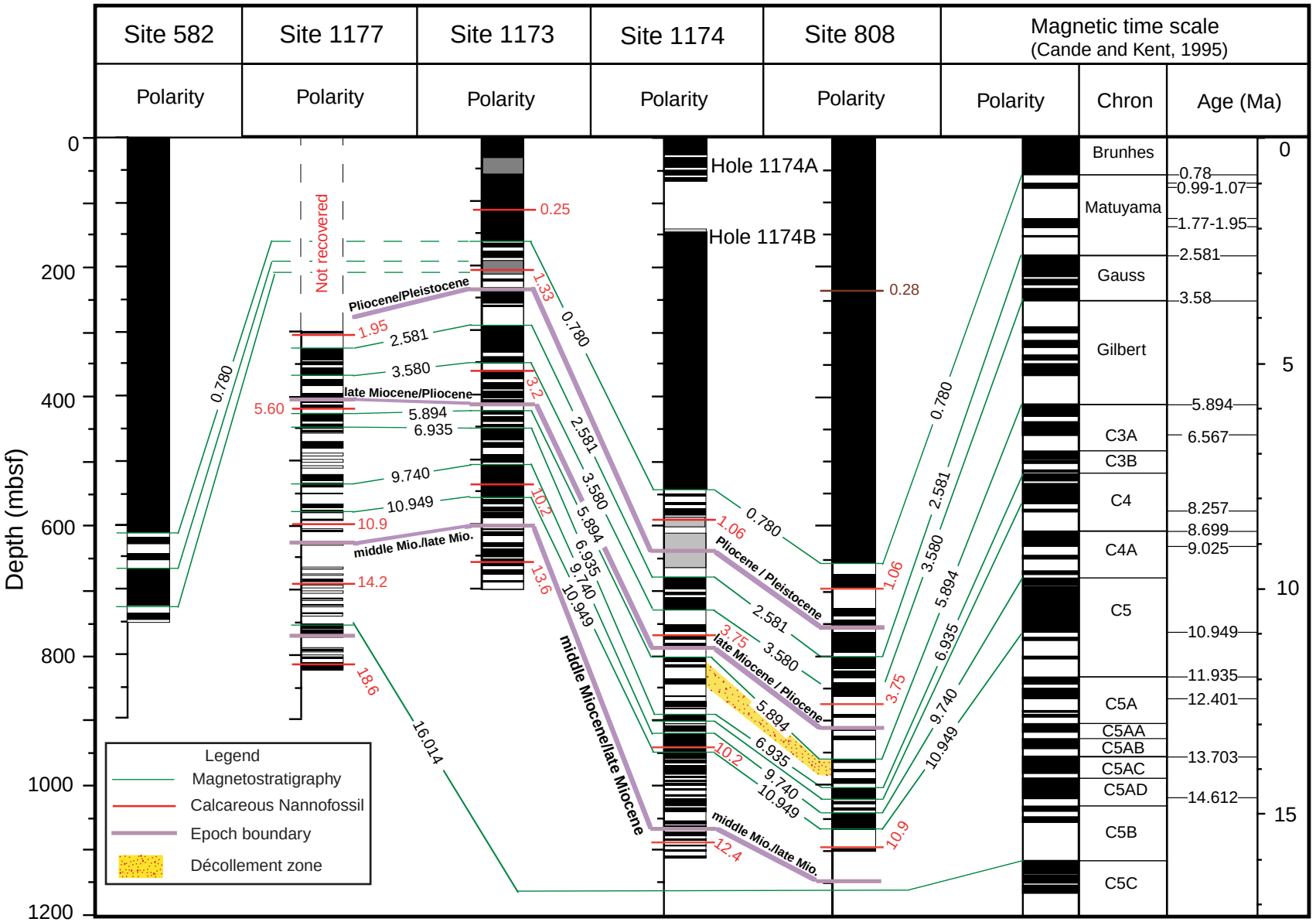
Site 582
Site 1177
Site 1173
Site 1174
Site 808
Magnetic time scale
(Cande and Kent, 1995)
Polarity
Chron
Age (Ma)
Depth (mbsf)
Hole 1174A
Hole 1174B
Not recovered
Pliocene/Pleistocene
late Miocene/Pliocene
middle Mio./late Mio.
Pliocene / Pleistocene
late Miocene / Pliocene
middle Miocene/late Miocene
middle Mio./late Mio.
Brunhes
Matuyama
Gauss
Gilbert
C3A
C3B
C4
C4A
C5
C5A
C5AA
C5AB
C5AC
C5AD
C5B
C5C
0.78
0.99-1.07
1.77-1.95
2.581
3.58
5.894
6.567
8.257
8.699
9.025
10.949
11.935
12.401
13.703
14.612
Legend
Magnetostratigraphy
Calcareous Nannofossil
Epoch boundary
Décollement zone

Figure 34

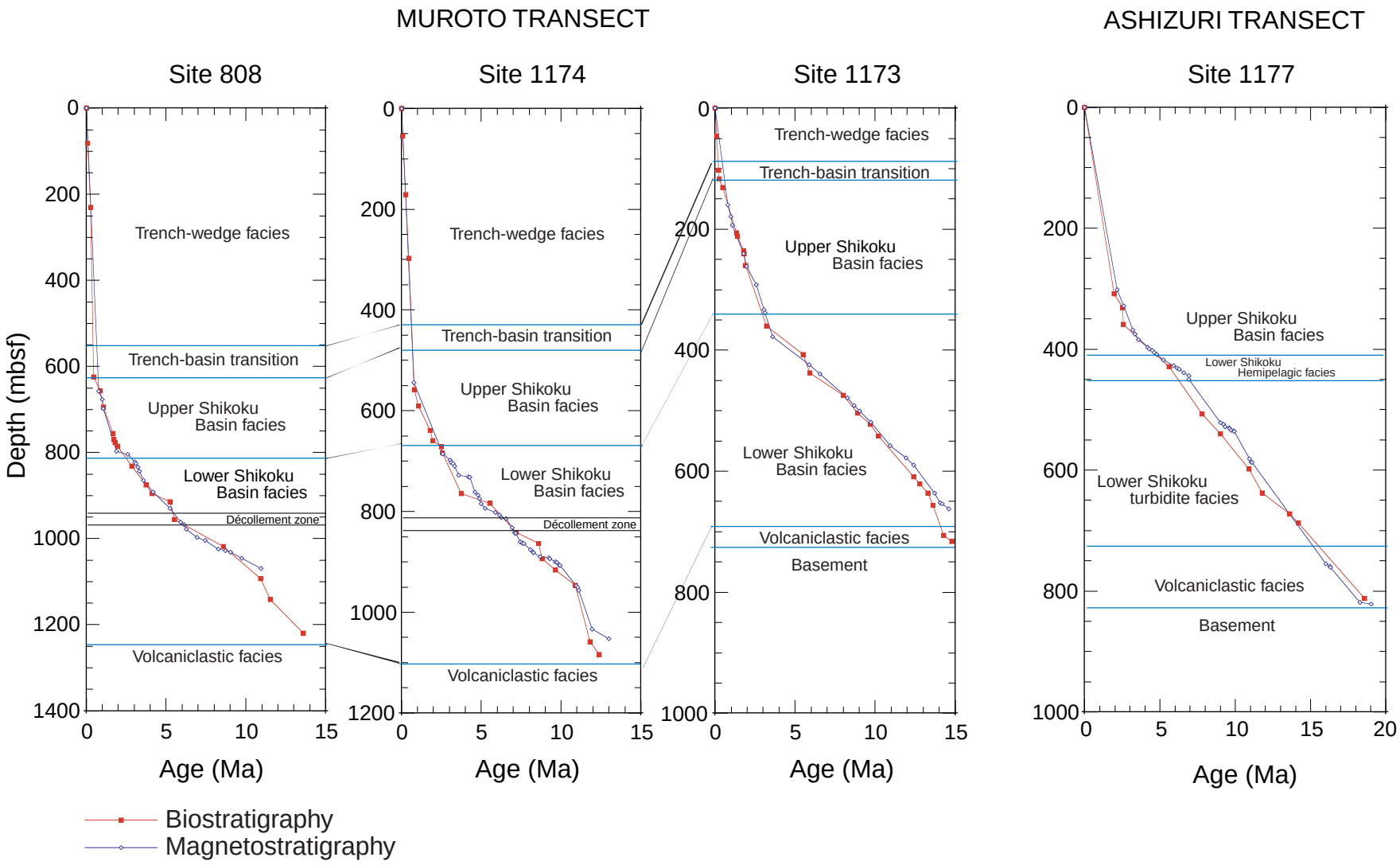
MUROTO TRANSECT
ASHIZURI TRANSECT
Site 808
Site 1174
Site 1173
Site 1177
Depth (mbsf)
Age (Ma)
Trench-wedge facies
Trench-basin transition
Upper Shikoku Basin facies
Lower Shikoku Basin facies
Décollement zone
Volcaniclastic facies
Basement
Lower Shikoku Hemipelagic facies
Lower Shikoku turbidite facies
Biostratigraphy
Magnetostratigraphy

Figure 35

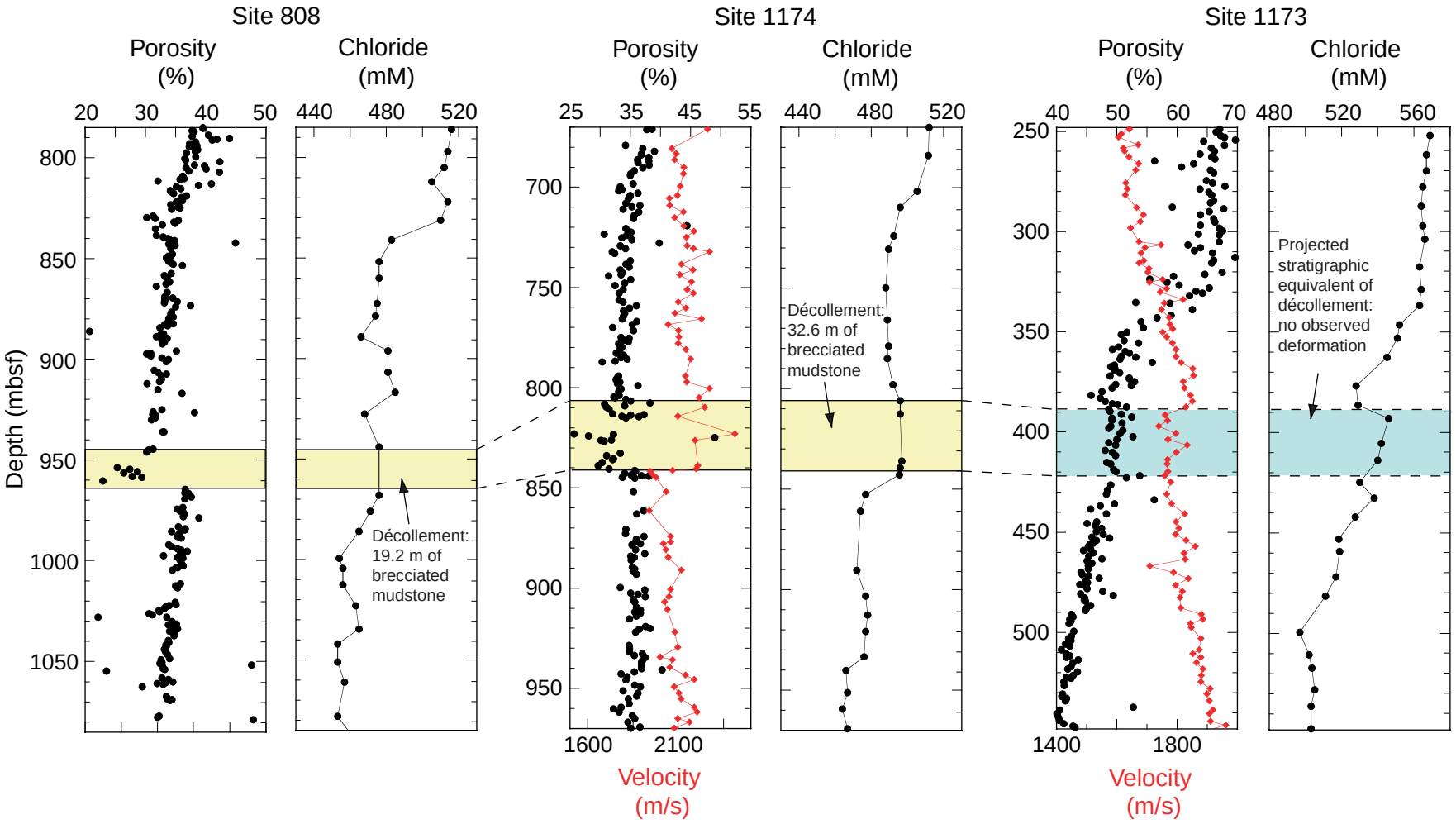
Site 808
Porosity (%)
Chloride (mM)
Depth (mbsf)
Décollement: 19.2 m of brecciated mudstone
Site 1174
Porosity (%)
Chloride (mM)
Décollement: 32.6 m of brecciated mudstone
Velocity (m/s)
Site 1173
Porosity (%)
Chloride (mM)
Projected stratigraphic equivalent of décollement: no observed deformation
Velocity (m/s)

Figure 36

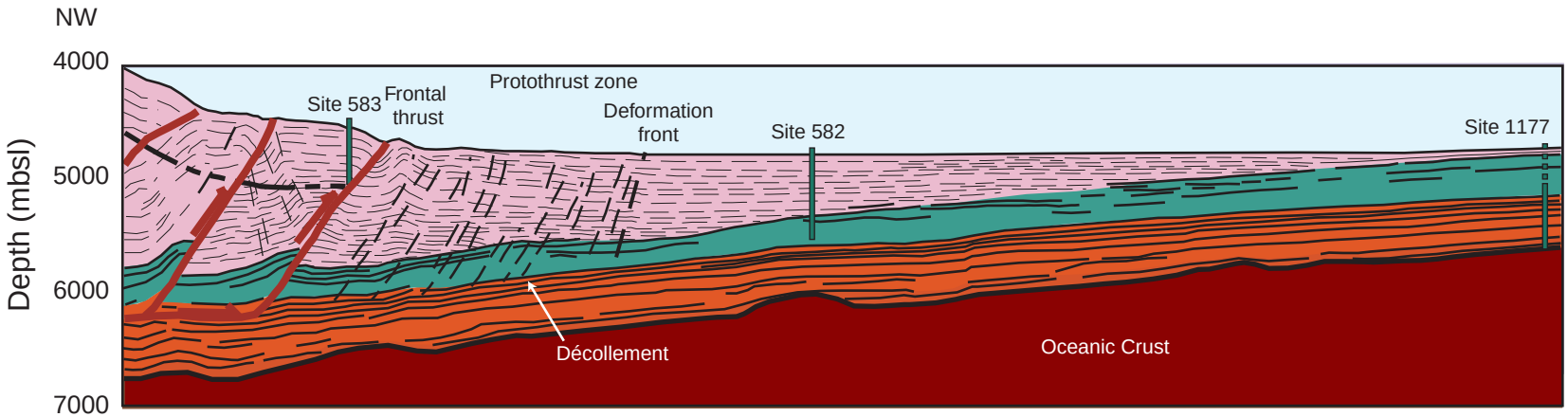
NW
SE
4000
5000
6000
7000
Depth (mbsl)
Site 583
Frontal thrust
Protothrust zone
Deformation front
Site 582
Site 1177
Décollement
Oceanic Crust

Figure 37

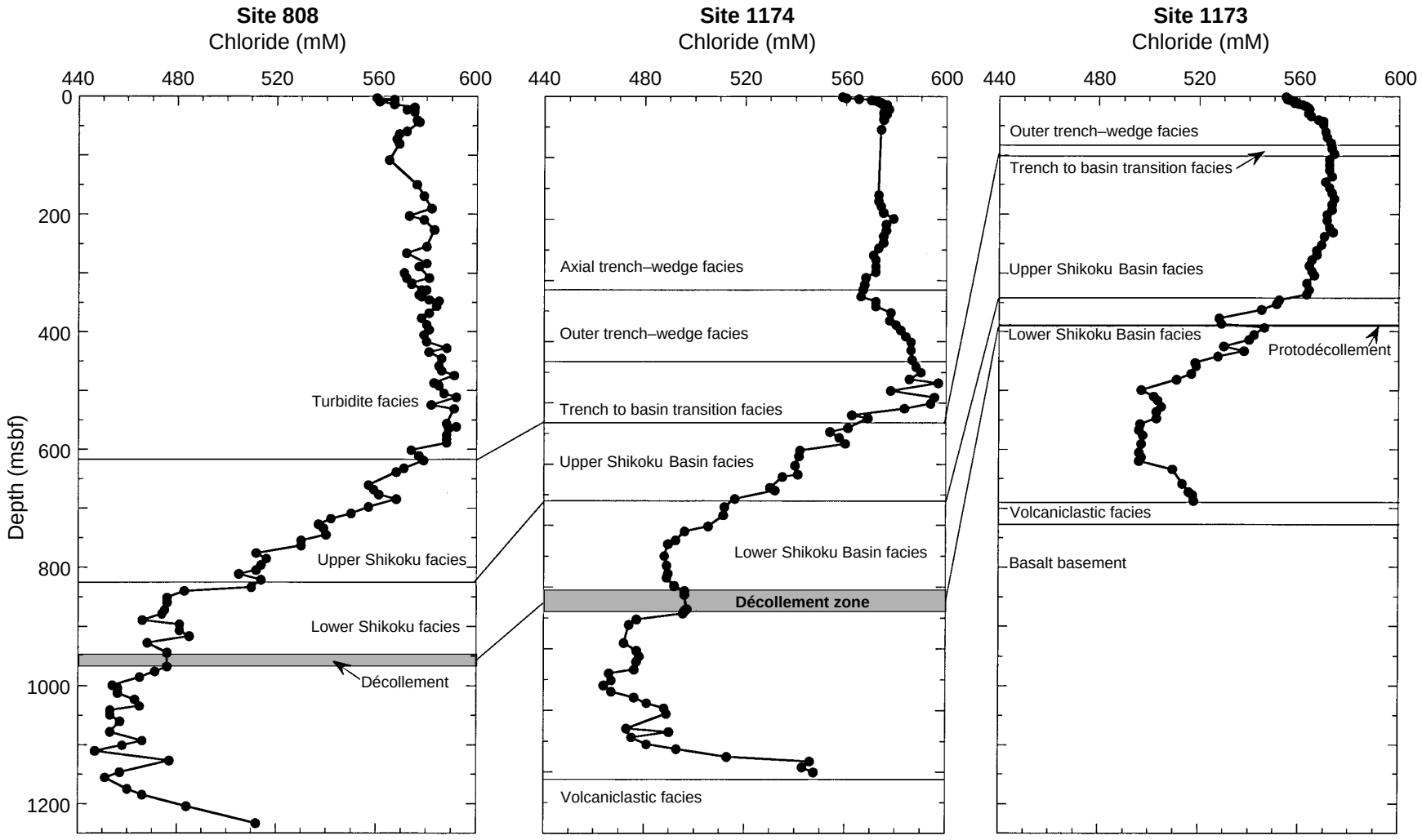
Site 808
Chloride (mM)
440
480
520
560
600
0
200
400
600
800
1000
1200
Depth (msbf)
Turbidite facies
Upper Shikoku facies
Lower Shikoku facies
Décollement
Site 1174
Chloride (mM)
Axial trench–wedge facies
Outer trench–wedge facies
Trench to basin transition facies
Upper Shikoku Basin facies
Lower Shikoku Basin facies
Décollement zone
Volcaniclastic facies
Site 1173
Chloride (mM)
Outer trench–wedge facies
Trench to basin transition facies
Upper Shikoku Basin facies
Lower Shikoku Basin facies
Protodécollement
Volcaniclastic facies
Basalt basement

Figure 38

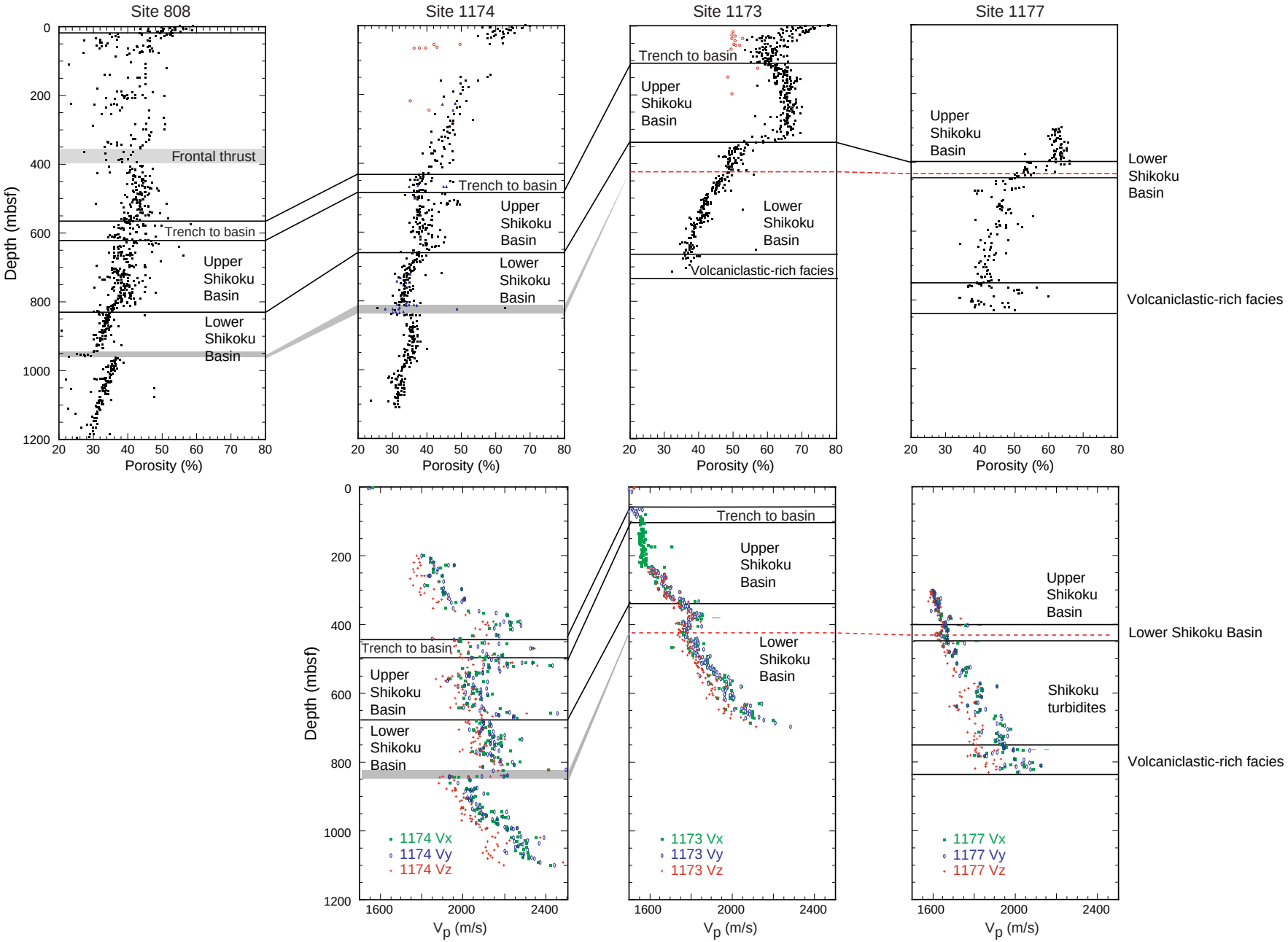
Site 808
Site 1174
Site 1173
Site 1177
Depth (mbsf)
Porosity (%)
Frontal thrust
Trench to basin
Upper Shikoku Basin
Lower Shikoku Basin
Volcaniclastic-rich facies
Lower Shikoku Basin
Shikoku turbidites
Vp (m/s)
1174 Vx
1174 Vy
1174 Vz
1173 Vx
1173 Vy
1173 Vz
1177 Vx
1177 Vy
1177 Vz

Figure 39

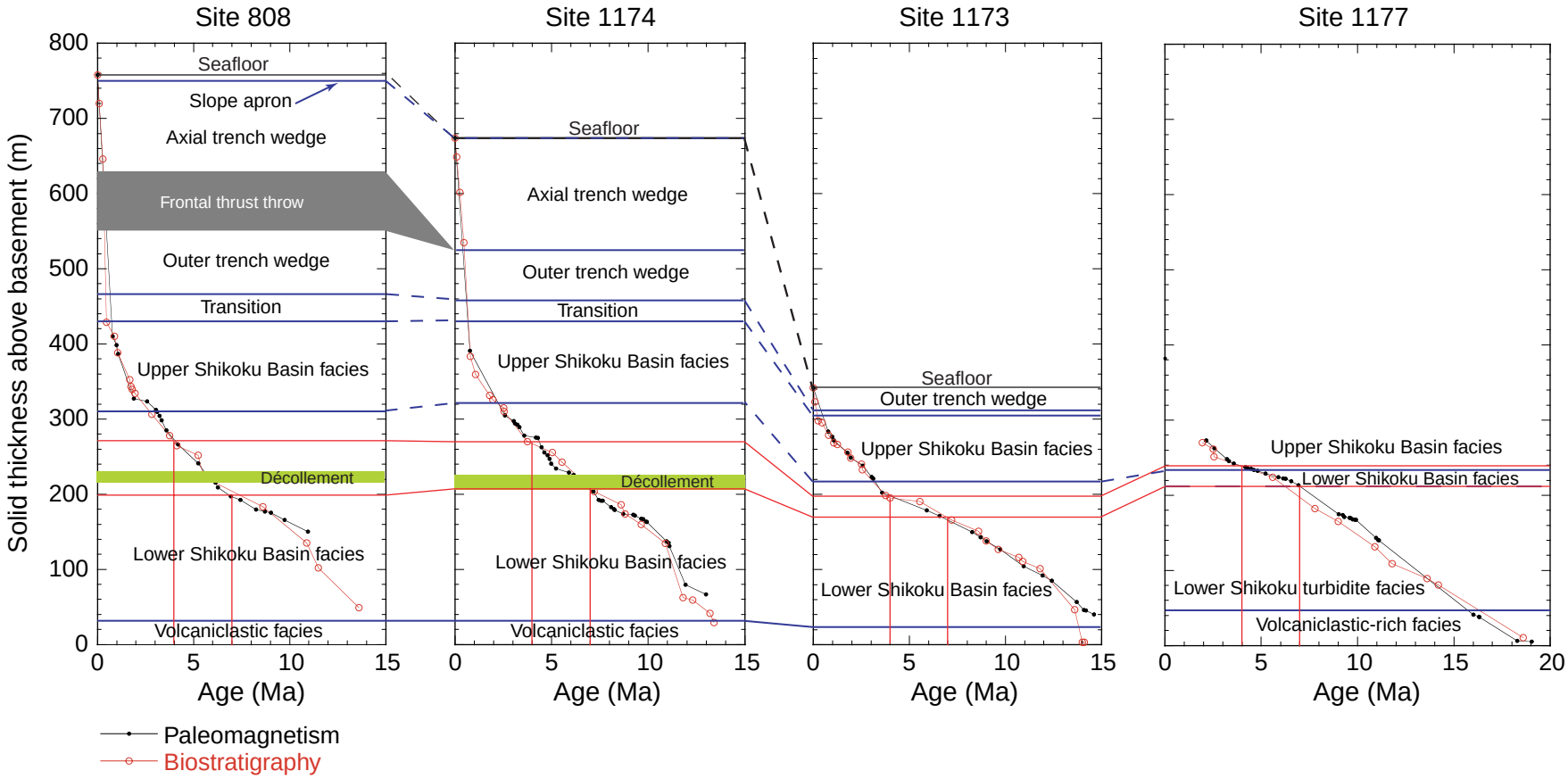
Site 808
Site 1174
Site 1173
Site 1177
Solid thickness above basement (m)
Age (Ma)
Seafloor
Slope apron
Axial trench wedge
Frontal thrust throw
Outer trench wedge
Transition
Upper Shikoku Basin facies
Décollement
Lower Shikoku Basin facies
Volcaniclastic facies
Lower Shikoku turbidite facies
Volcaniclastic-rich facies
Paleomagnetism
Biostratigraphy

Figure 40

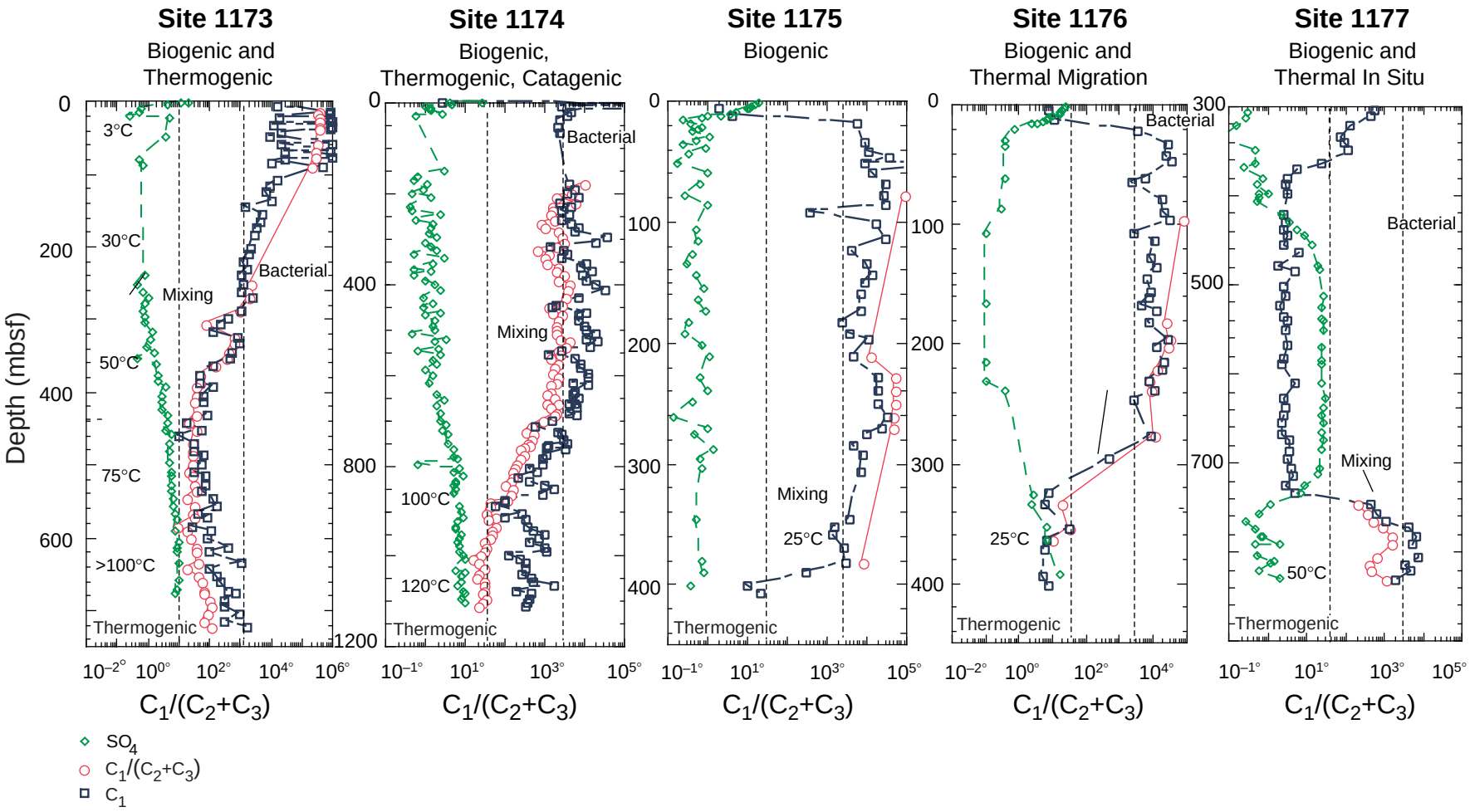
Site 1173
Biogenic and Thermogenic
Site 1174
Biogenic, Thermogenic, Catagenic
Site 1175
Biogenic
Site 1176
Biogenic and Thermal Migration
Site 1177
Biogenic and Thermal In Situ
Depth (mbsf)
3°C
30°C
50°C
75°C
>100°C
100°C
120°C
25°C
50°C
Bacterial
Mixing
Thermogenic
C1/(C2+C3)
SO4
C1/(C2+C3)
C1

Figure 41

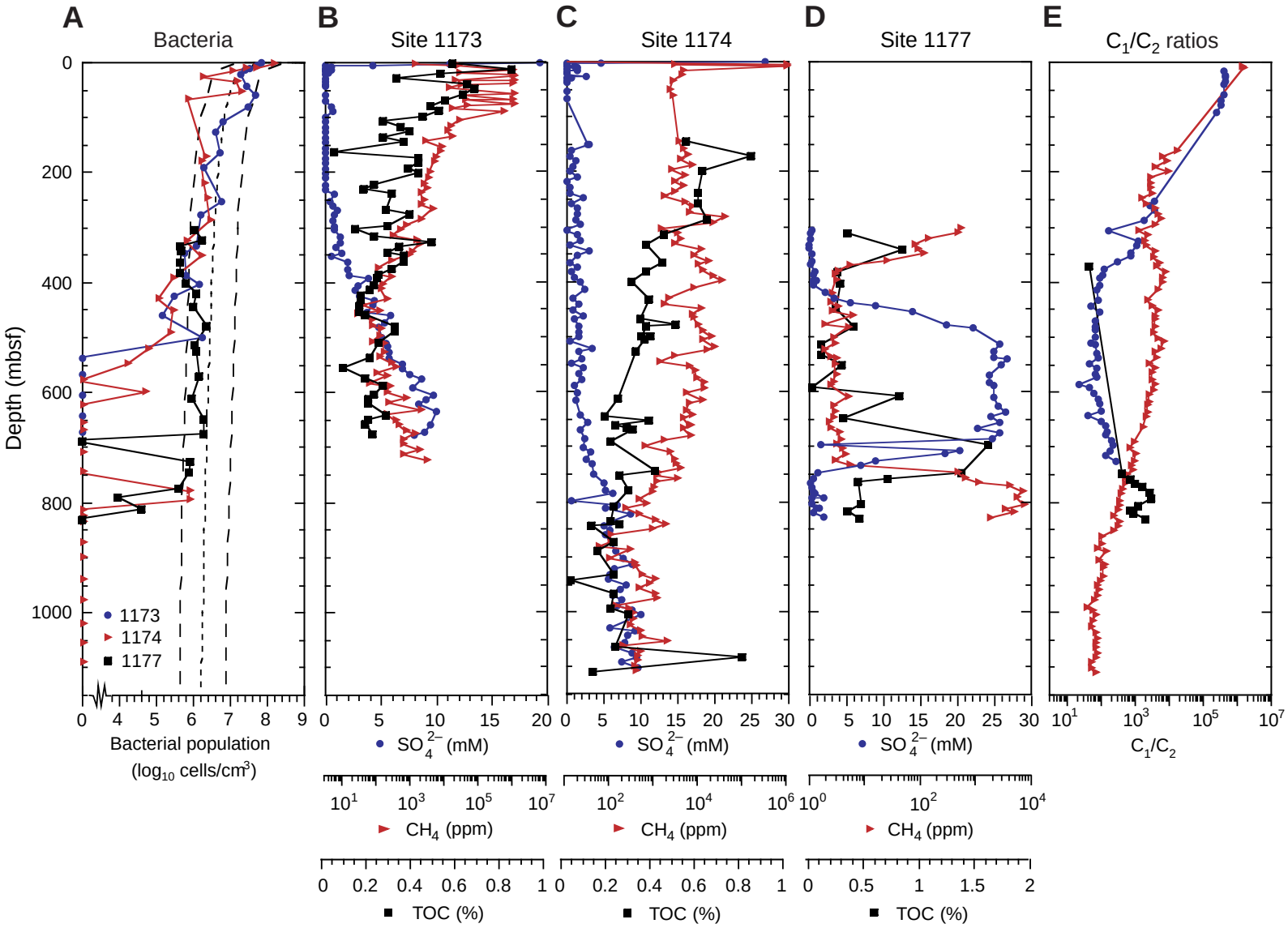
A
Bacteria
B
Site 1173
C
Site 1174
D
Site 1177
E
C1/C2 ratios
Depth (mbsf)
0
200
400
600
800
1000
1173
1174
1177
0 4 5 6 7 8 9
Bacterial population
(log10 cells/cm3)
0 5 10 15 20
SO4 2– (mM)
10^1 10^3 10^5 10^7
CH4 (ppm)
0 0.2 0.4 0.6 0.8 1
TOC (%)
0 5 10 15 20 25 30
SO4 2– (mM)
10^2 10^4 10^6
CH4 (ppm)
0 0.2 0.4 0.6 0.8 1
TOC (%)
0 5 10 15 20 25 30
SO4 2– (mM)
10^0 10^2 10^4
CH4 (ppm)
0 0.5 1 1.5 2
TOC (%)
10^1 10^3 10^5 10^7
C1/C2

Figure 42

OPERATIONS SYNOPSIS[1]

SITE 1173 (ENT-01A)

Transit from Guam to Site ENT-01A (1173)

The 1210-nmi transit from Guam to Site ENT-01A (1173) was accomplished at an average speed of 11.8 kt in 4.25 days. During the transit, the drilling and coring equipment were prepared. A variety of repairs to the accommodations were made during the transit, including replacement of some of the ceiling tiles in the hotel hallways, replacement of sinks and toilets, painting, and so forth. The clocks were turned back 1 hr at midnight on the night of 27 May so the ship would be on Japan local time.

When approaching Site ENT-01A (1173), the ship slowed from transit speed to ~5 nmi/hr to conduct a seismic reflection survey that covered 48 nmi and lasted 9.8 hr. Once the survey passed over Site ENT-01A (1173), the seismic gear was retrieved and the vessel moved to the Global Positioning System (GPS) coordinates of the site. Once over the GPS coordinates, a seafloor positioning beacon was dropped at 1202 hr on 28 May, establishing Site 1173.

Site 1173

After the hydrophones and thrusters were lowered and the vessel settled on location, the precision depth recorder (PDR) indicated a water depth of 4794.4 meters below rig floor (mbrf). An eight collar advanced hydraulic piston corer/extended core barrel (APC/XCB) bottom hole assembly (BHA) was made up with a $9^{7}/_{8}$-in polycrystalline diamond compact (PDC) bit, lockable float valve (LFV), seal bore drill collar, landing saver sub, top sub, head sub, nonmagnetic drill collar, five 8¼-in drill collars, one tapered drill collar (TDC), six joints of 5½-in drill pipe, and a crossover sub to 5-in drill pipe. Once the BHA was made up it was run down to the seafloor. Running the drill string to the seafloor took longer than usual because of the measuring and internal clearance inspection (strapping and rabbiting) that is routinely performed during the first deployment of the drill string during a leg. The pipe trip down to the seafloor was also interrupted for an hour while the active heave compensator (AHC) hydraulic umbilical sheath was repaired.

Once the bit was near the seafloor, at 4780 mbrf, and before we circulated any seawater through the drill string, the water-sampling temperature probe (WSTP) was deployed to obtain a water sample near the seafloor. Because the WSTP could not be pumped to bottom, ~3 hr was required to obtain the water sample.

---

[1] The Operations and Engineering personnel aboard *JOIDES Resolution* for Leg 190 were ODP Operations Manager Tom Pettigrew, ODP Operations Engineer Derryl Schroeder, and Schlumberger Engineer Steven Kittredge.

Hole 1173A

After successfully obtaining a seafloor water sample, seawater was circulated through the drill string and a "pig" pumped through it to clean the interior of the drill pipe. The bit was placed at 4778.8 meters below sea level (mbsl) (4790 mbrf) and an APC was shot but did not recover any sediment. The bit was lowered to 4788.34 mbsl (4799.54 mbrf), the APC was shot again, and Hole 1173A was spudded at 1125 hr 29 on May. Core 1H recovered 7.14 m of core, indicating that the seafloor depth as determined by drill-pipe measurement was 4790.7 mbsl (4801.9 mbrf). APC coring continued to 225.6 mbsf (5027.5 mbrf), recovering 222.35 m of core (99%). Once the APC pull-out force reached 60 klbs, we switched to coring with the XCB.

We cored with the XCB from 225.6 to 734.3 mbsf (5027.5 to 5536.2 mbrf). A total of 53 XCB cores were taken over the 508.7-m interval, recovering 436.01 m of core for an overall XCB recovery of 86%. Although the XCB recovery was very good, the last four XCB cores recovered only 1.79 m (5% recovery). In addition, while we cored the last 7 m of the hole, the rate of penetration dropped to <5 m/hr and high erratic torque was experienced. When we lifted the bit off bottom, there was virtually no torque and the XCB cutting shoe was recovered in good shape; therefore, it was presumed that the bit might have failed. At this point, we decided to stop coring and to log the hole. Subsequently, we found small pieces of basalt in the bottom of the last core, so we infer that the high and erratic torque may have been caused by rotating the bit on basaltic basement.

We circulated a 50-bbl pill of sepiolite mud to clean the hole of any cuttings and then filled it with sepiolite mud. The bit was raised to 95.12 mbsf (4897.0 mbrf), and the logging tools were rigged up. The triple combination tool (triple combo) was lowered in the hole but could not pass a bridge at 344.1 mbsf (5146 mbrf); therefore, we logged up from that point to the bit.

The logging tools were laid out, the drill string was lowered to 444.7 mbsf (5246.4 mbrf), and the drill string did not encounter any resistance when passing through the bridge. The bit was raised to 364.8 mbsf (5166.8 mbrf), and the logging tools were rigged up once more. The triple combo was lowered down the drill string, and after having some trouble getting through the bit it was able to reach 438.1 mbsf (5240.0 mbrf), where yet another bridge prevented the tool from passing any farther. Once again, the hole was logged from that point up to the bit. The logging tool had to be worked through the bit into the drill string. Once back inside the drill string, the logging tools were recovered and laid out.

The drill string was then lowered in an effort to clean out the hole. When the drill string was picked up off the slips, 70,000 lb of overpull was required to free the bit, which had become stuck in the hole. The drill string had to be worked with as much as 20,000 lb of overpull and set down weight to get to 637.1 mbsf (5439 mbrf), where the hole starting packing off. The drill string was then pulled to 628.1 mbsf (5430 mbrf), where 226 bbl of 10.5-ppg weighted mud was pumped to displace the hole. The drill string was then raised to 95 mbsf (4879 mbrf), and the logging tools were rigged up once more.

This final logging run included the sonic and Formation MicroScanner tools. This time the tools encountered a bridge 378 mbsf (5180 mbrf), and we logged up from there. After the

logging tools were recovered and laid out, we tripped the drill string back to the ship. Hole 1173A officially ended at 0445 hr on June 7 when the bit reached the rig floor.

SITE 1174 (ENT-03A)

Transit from Site 1173 to Site ENT-03A (1174)

The bit was pulled from Hole 1173A, clearing the seafloor at 1930 hr on 6 June. After the positioning beacon was released and recovered at 2100 hr, the vessel started moving to Site ENT-03A (1174) in dynamic positioning (DP) mode. The drill string was recovered during the transit and the bit cleared the rotary table at 0445 hr on 7 June, officially ending Hole 1173A. A positioning beacon was dropped at 0700 hr on 7 June, establishing Site 1174.

Site 1174

The PDR indicated a water depth of 4754.4 mbrf. An eight-drill collar APC/XCB BHA was made up with an 11-7/16-in roller cone bit, LFV, a seal bore drill collar, landing saver sub, top sub, head sub, nonmagnetic drill collar, five 8¼-in drill collars, one TDC, six joints of 5½-in drill pipe, and a crossover sub to 5-in drill pipe. The drill string was tripped to the seafloor, the bit was positioned at 4741.1 mbsl (4752.4 mbrf), and core was taken but did not recover any sediment. The bit was repositioned at 4746.1 mbsl (4757.4 mbrf) and Hole 1174A was successfully spudded at 1735 hr on 7 June. Core 1H recovered 4.4 m of sediment, establishing the drilling depth as 4751.2 mbsl (4762.5 mbrf).

Hole 1174A

Cores 1H to 8H were cored from 0 to 64.4 mbsf and recovered 47.04 m (73%). Fine-grained sand and silts likely caused the somewhat low core recovery. The force required to pull the APC barrel out of the formation increased until it had reached 70,000 lb on Core 7H. Core 8H resulted in a partial stroke with only 3 m of penetration, so the coring system was changed over to the XCB.

Core 9X was cut from 64.4 to 74.1 mbsf. When we tried to retrieve the core barrel, it could not be pulled free from the BHA. A 50-bbl sepiolite pill was pumped past the core barrel in an effort to clean any sands/silts that might be causing it to jam, but this did not help and the entire drill string had to be recovered. The bit cleared the rotary table at 0130 hr on 9 June, officially ending Hole 1174A.

When the BHA reached the rig floor, it was discovered that the core barrel was stuck inside the nonmagnetic outer drill collar. When the core barrel was finally dislodged, one of the XCB latching mechanisms (dogs) was found to have failed. A 1½-in long piece was missing from the middle of the latch dog. One of the remaining ends of the latch was still locked inside the XCB body and had rotated outward, pinning the core barrel in place. This is the first known occurrence of this type of failure, and the cause is as yet unknown.

Hole 1174B

The decision was made to set a drill-in-casing (DIC) system in Hole 1174B to case off the loose sands near the seafloor in preparation for an 1150-m-deep penetration through the protothrust and décollement zones. Eleven joints of 11¾-in casing (142.2 m) were made up with a new 14¾-in sawtooth casing bit welded on the end and hung off on the moonpool doors. A $9^{7}/_{8}$-in tri-cone bit was made up to the drilling assembly and was spaced out ~1 m ahead of the casing bit. Once the drilling assembly was attached to the casing assembly, a DIC reentry funnel was attached to the DIC drive bushing. The completed DIC assembly was then lowered to the seafloor.

While we assembled the DIC system, it was necessary to allow the ship to drift with the current. After the DIC assembly had reached the seafloor, another hour of maneuvering in DP mode was required to move the vessel back on location. Hole 1174B was spudded at 0943 hr on 10 June.

The DIC was first jetted into ~50 mbsf with the following maximum jetting parameters, 45 strokes per minute (spm), 400 psi, 5–10 klbs weight on bit (WOB). Then the DIC was drilled into 143.67 mbsf (4906.17 mbrf) with maximum drilling parameters of 80 spm, 1050 psi, 8–10 klbs WOB, 10 rpm, and 6000–9000 ft-lb of torque. Total time for emplacement was ~7.25 hr, and no problems were encountered.

The rotary shifting tool (RST) was then deployed on the wireline to unlatch the DIC. The weight of the DIC casing, ~22,000 lb, was slacked off in preparation for unlatching. The RST had to be worked through the DIC three times before a definite indication of the release sleeve shifting was observed. The drill string was then picked up, and the weight of the DIC system was lost, indicating that it had released properly.

We intended to have Hole 1174B penetrate a relatively thick section that might be unstable; therefore, the decision was made to round trip the drill string to remove the DIC drive sub and then reenter with a standard RCB BHA. Thus, the drill string was recovered.

The DIC BHA was broken out, and an RCB BHA was made up. The RCB was tripped to the seafloor and the vibration-isolated television (VIT) camera frame was lowered to the seafloor in preparation for reentry. The search for the DIC reentry funnel began at 1830 hr on 11 June, and the funnel was first sighted visually at ~2315 hr. At 2347 hr on 11 June, Hole 1174B was reentered and the VIT was recovered. The bit was lowered into the hole with moderate drag until the bit had reached 52.5 mbsf, where some resistance was encountered. The top drive was picked up, and the bit had to be worked down all the way through the cased section.

Hole 1174B was then cored from 143.7 to 265.8 mbsf (4906.2 to 5028.3 mbrf) with high erratic torque. At this depth the bit became stuck. The drill string was worked for 1 hr, and 120,000 lb of overpull was required to free the bit. The bit was raised up inside the casing with drag and high erratic torque all the way. The bit was eventually raised to 50 mbsf (4852 mbrf), where the high erratic torque finally disappeared.

The bit was lowered once again, encountering an obstruction at 52.5 mbsf (4854.5 mbrf). The bit was worked through this problem area inside the casing several times until it was thought

that the obstruction was no longer a threat to the coring operations. The bit was then lowered back down into the open hole, encountering fill at 172.5 mbsf (4935 mbrf). The hole was washed and reamed to bottom and coring resumed.

Some further insight into the mysterious high erratic torque previously observed while coring in Hole 1174B appeared in the top of Core 20R. A piece of chewed-up metal ~3 in long, 1½ in wide, and ¼ in thick was recovered. Additional pieces of metal were found in other succeeding cores. Unfortunately, the origin of the metal is still not clear.

While retrieving Core 40R from 524.3 mbsf (5286.8 mbrf), the forward core winch wireline parted at the crown with the core barrel at 3664 mbrf. The frayed end of the wireline caught in the oil saver on top of the swivel and T-bar clamps were used to pull the parted wireline up through the top drive. Preparations were then made to string the parted wireline back over the crown sheave and reattach it to the coring winch. However, when the derrick man reached the crown, he discovered that the outboard wireline crown sheave had failed.

Approximately one-third of the sheave rim on the outboard side had separated from the sheave body. A used sheave was located on board and was installed to replace the failed sheave. The parted wireline was strung over the replacement sheave and reattached to the core winch with cable clamps. The parted wireline was recovered along with the core barrel, which contained 9.21 m of core. The forward core winch was secured, and the aft core winch, which had 9600 m of new wireline on it, was placed into service. A total of 8.25 hr of down time was incurred as a result of the parted wireline and failed sheave.

Although rotation and circulation were maintained while we recovered the parted wireline and replaced the failed sheave, a wiper trip was carried out before we resumed coring operations. The bit was pulled to 128.43 mbsf (4890.93 mbrf), inside the DIC casing shoe. Once the bit was back inside the casing, an overdue maintenance of the drill line (slip and cut) was carried out. The bit was then lowered to 459.86 mbsf (5222.36 mbrf), where slight drag was encountered. The top drive was picked up and the hole was washed and reamed to 524.3 mbsf. Approximately 7 m of soft fill was encountered in the bottom of the hole. RCB coring then resumed, and Cores 41R to 102R were recovered from 533.9 to 1119.8 mbsf (5882.3 mbrf). After drilling in the DIC to 143.7 mbsf, Hole 1174B was continuously cored through 976.1 m of section. Recovery was 577.57 m (60%).

Because some gas was detected in the formation, the hole was displaced with 280 bbl of heavy mud. After the hole was displaced, the pipe was pulled out of the hole with no rotation or circulation. When the bit reached 398.2 mbsf (5160.3 mbrf), a tight spot was encountered and the pipe was worked without picking up the top drive. A 60,000-lb overpull was being applied to the drill string when the pipe came free. However, the drill string weight was ~70,000 lb lighter, indicating that the drill string had parted, and the pipe trip continued. The drill string had parted 467 m above the seafloor.

Once the drill pipe was clear of the seafloor, the two seafloor positioning beacons were given release commands. The primary beacon released and was recovered. However, the backup beacon failed to release and was not recovered. Once the beacon was on board and the end of the

pipe was near the rig floor, the thrusters and hydrophones were raised and the vessel began the 2-hr transit to Site ENT-05A (1175).

The end of the drill pipe cleared the rig floor at 2230 hr on 22 June. The pin connection on the bottom of drill pipe stand number 26 had failed. Lost in the hole were a 9^{7}a -in RCB bit, mechanical bit release, outer core barrel, top sub, head sub, seven 8¼-in drill collars, transition drill collar, six joints of 5½-in drill pipe, a crossover sub, and 75 joints of 5-in drill pipe.

SITE 1175 (ENT-07A)

A seafloor positioning beacon was dropped at 2230 hr on 22 June, establishing Site 1175. A new APC BHA consisting of a 9$^{7}/_{8}$-in PDC bit, a bit sub with a lockable float valve, a seal bore drill collar, landing saver sub, modified top sub, modified head sub, nonmagnetic drill collar, seven 8¼-in drill collars, a tapered drill collar, a crossover sub, six joints of 5½-in drill pipe, and a crossover sub to 5-in drill pipe was assembled and run in the hole. The PDR indicated a seafloor depth of 3024.4 mbrf. The bit was positioned at 3010 mbrf, and the WSTP was deployed to take a seafloor water sample prior to establishing any circulation. The WSTP was recovered with traces of sediment on it indicating that the water depth was shallower than anticipated.

Hole 1175A

After recovering the WSTP, the bit was positioned at 3006.7 mbrf and Core 1H was taken, recovering 7.12 m of core and establishing a seafloor depth of 3009.1 m. Hole 1175A was then APC cored from the mudline to 92.7 mbsf (3101.8 mbrf), where Core 11H resulted in a short stroke and recovered 2.32 m of loose sand. The bit was washed ahead without coring to 100.8 mbsf (3109.9 mbrf) in an attempt to get through the loose sand. Core 12H from 100.8 to 110.3 mbsf (3109.9–3119.4 mbrf) recovered 9.58 m of sediment. Normal APC coring operations continued without unusual overpull until Core 22H (195.8–205.3 mbsf; 3204.9–3214.4 mbrf), which could not be pulled out of the formation. The drill string space out was such that a short kelly was left after shooting the core; therefore, only 3 m of the core barrel could be drilled over. After drilling over these 3 m, the core barrel was pulled out with 120,000 lb overpull and heavy circulation.

Twenty-two APC cores were taken from Hole 1175A, recovering 197.68 m of sediment from 199.5 m of cored section (99% recovery); 5.8 m was drilled without coring. After recovering Core 22H, the XCB coring system was use to obtain Cores 23X through 47X (205.3–445.5 mbsf) and recovered 129.3 m of sediment (54%).

After terminating coring in Hole 1175A, the hole was displaced with 136 bbl of heavy mud. Because the formation contained a considerable amount of loose sand, the bit was pulled to 289.92 mbsf (3299.02 mbrf) with the top drive in place. The top drive was racked back, and the bit was pulled 153.7 m above the seafloor for the move to Site 1176. The bit cleared the seafloor

at 0500 hr on 26 June and the seafloor positioning beacon was released. The beacon was recovered at 0615 hr on 26 June, ending operations at Site 1175.

SITE 1176 (ENT-06A)

Transit from Site 1175 to Site ENT-06A (1176)

Once the seafloor positioning beacon was recovered, the ship made the 1.6-nmi transit to Site ENT-06A (1176) was made in dynamic positioning mode in 3 hr. During the transit, the instrumented load pins, which had been returned to the ship on the boat transfer earlier in the leg, were reinstalled in the block. A seafloor positioning beacon was deployed at 0915 hr on 26 June, establishing Site 1176.

Hole 1176A

The PDR indicated a seafloor depth of 3016.8 mbsl (3028.4 mbrf). Based on the correlation between the previous PDR measurements and the drilling depth as determined via drill-pipe measurement, the bit was lowered to 3018.4 mbsl (3030 mbrf). Hole 1176A was spudded at 1305 hr on 26 June. In Core 1H, 7.41 m of sediment was recovered, indicating a seafloor depth determined by drill-pipe measurement of 3020.5 mbsl (3032.1 mbrf). The hole was cored with the APC from the seafloor to 170.6 mbsf (3202.7 mbrf), where the overpull had increased to 60,000 lb while we retrieved Core 19H. A considerable amount of sand was encountered in the hole, and a 6.1-m section of sand (from 115.3 to 121.4 mbsf; 3147.4 to 3153.5 mbrf) was drilled ahead without coring. Nineteen APC cores were taken that penetrated 164.5 m of section and recovered 151.43 m of sediment (92%).

The XCB coring system was then used to core from 170.6 to 449.6 mbsf (3202.7 to 3481.7 mbrf). A total of 29 XCB cores were taken, coring 279.0 m and recovering 74.82 m (27%). Sand was encountered virtually throughout the entire borehole. The scientists decided to terminate the hole because the extensive sands prevented the primary objectives of the hole to be achieved.

The bit was pulled out of the hole and cleared the seafloor at 0745 hr on 29 June. The seafloor positioning beacon was released at 0845 hr and sighted on the surface at 0925 hr. At this time, however, the current was ~2.8 nmi/hr and there were also 15-kt winds, so the beacon was swept away from the ship before it could be recovered. The pipe trip continued and the bit cleared the rotary table at 1345 hr, ending Hole 1176A and operations at Site 1176. Once the bit was back on board, the ship began the transit to Site 1177 in dynamic positioning mode.

SITE 1177 (WNT-01B)

Transit from Site 1176 to Site WNT-01B (1177)

Before starting the transit to Site WNT-01B (1177), normal operations were interrupted for 3.25 hr so that the leaking AHC hydraulic umbilical could be inspected. A hole in one of the high-pressure supply lines was found but could not be repaired on board. The ship began the transit at 1700 hr on 29 June. During the transit, the ship stopped for another 2 hr (2000 to 2200 hr) to finish securing the AHC hydraulic umbilical in the derrick. The 70-nmi transit was made in 7 hr. A seafloor positioning beacon was deployed at 0222 hr on 30 June, initiating Site 1177.

Hole 1177A

The PDR indicated a drilling depth of 4851.4 mbrf. A standard RCB BHA was made up and run down to the seafloor. At 1500 hr on 30 June, the driller perceived the seafloor by a reduction in drill string weight at 4844.3 mbsl (4856 mbrf). Hole 1177A was then spudded and drilled to 300.2 mbsf (5156.2 mbrf). Davis-Villinger temperature probe measurements were taken at 50.5 mbsf (4906.5 mbrf) and 120 mbsf (4976.0 mbrf) but did not obtain good data. Hole 1177A was then cored from 300.2 to 833.9 mbsf (Cores 1R to 56R) and recovered 282.74 m (53%).

Coring was stopped after basalt was recovered in Core 56R. The bit was then tripped out of the hole. Once the bit had cleared the seafloor, the drill line was slipped and cut. The seafloor positioning beacon was released and recovered at 0910 hr on 5 July. The bit cleared the rig floor at 1730 hr on 5 July, ending operations at Site 1177, and the transit to Site 1178 began at 1930 hr on 5 July.

Transit from Site 1177 to Site ENT-10A

Once the bit arrived on deck, the transit to Site ENT-10A began at 1930 hr on 5 July. Typhoon Kirogi was approaching our location from the south and was predicted to pass close to the drill site. Although the weather in the vicinity of the vessel was good, a heavy swell was coming out of the south, causing excessive vessel pitch and roll. Because of the deep water depth at Site ENT-10A (~4554 mbsl) we decided not to deploy the drill string and to suspend operations until the weather would allow safe operations. While the vessel was on standby, 20 stands of 5-in drill pipe were removed from the riser hold, made up, and placed in the middle bay of the pipe racker. The leaking AHC hydraulic umbilical was removed and placed on pallets on main deck, and the coaxial cable was removed from the VIT winch in preparation for installation of the new cable during the Yokohama port call after the leg.

At 1045 hr on 7 July, we decided to move the vessel out of the path of typhoon Kirogi and maintain at least a 250-nmi distance from it. The vessel was moved ~98 nmi to the west and then looped around behind the typhoon. Because of the loss in operations time as a result of the typhoon, all of the Site ENT-10A objectives could not be accomplished. Therefore, we decided to core at alternate Site ENT-09A (1178) instead.

SITE 1178 (ENT-09A)

The vessel reached Site ENT-09A (1178) at 0730 hr on 8 July, and preparations for making up the BHA began. Considerable current was observed, so the vessel was offset upcurrent 200 m from the location to drop the beacon. The beacon was dropped at 0845 hr on 8 July, establishing Site 1178. Once the hydrophones and thrusters were lowered and the ship settled out over the site in DP mode, it was determined that the beacon had come to rest on the seafloor 180 m downcurrent of the location.

Hole 1178A

Because of the strong current, the ship had to be offset upcurrent from the location and allowed to drift back to enable the drill collars to be made up. A BHA consisting of a $9^{7}/_{8}$-in PDC bit, bit sub, seal bore drill collar, landing saver sub, modified top sub, modified head sub, nonmagnetic drill collar, seven 8¼-in drill collars, a tapered drill collar, and crossover sub was assembled.

A PDR measurement was taken that indicated a drilling depth of 1716.5 mbsl (1728.4 mbrf). The bit was lowered to 1710 mbrf where a bottom-water sample was collected using the WSTP. The bit was then lowered to 1728 mbrf; core was taken but no sediment was recovered. The bit was lowered to 1725.6 mbsl (1737.5 mbrf), and another core was taken, with no sediment recovered. The bit was once again lowered 9.5 m to 1735.1 mbsl (1747 mbrf), and Hole 1178A was spudded at 1855 hr on 8 July. Core 1H recovered 2.9 m of sediment, establishing the seafloor depth as 1741.7 mbsl (1753.6 mbrf).

Cores 1H to 44X were taken from 0 to 410.8 mbsf (1753.6–2164.4 mbrf), recovering 340.19 m of core (83%). The penetration rate had decreased to <6 m/hr, when the decision was made to terminate XCB coring and switch to RCB coring. Hole 1178A was filled with 122 bbl of heavy mud, and then the pipe was tripped out of the hole. The bit cleared the rig floor at 1430 hr on 11 July, officially ending Hole 1178A. Because Hole 1178A was the last deployment of the APC/XCB BHA for Leg 190, it was disassembled.

Hole 1178B

The ship was offset 20 m to the east as an RCB BHA was being assembled. The BHA consisted of a new $9^{7}/_{8}$-in CC-3 roller cone bit, a bit sub, 8¼-in drill collar, modified top sub, modified head sub, seven 8¼-in drill collars, a tapered drill collar, six joints of 5½-in drill pipe, and a crossover sub to 5-in drill pipe. The bit was tripped to the seafloor, and Hole 1178B was spudded at 2015 hr on 11 July.

Hole 1178B was first drilled to 395 mbsf (1753.6–2148.6 mbrf). RCB coring then commenced, and Cores 2R through 31R were taken from 395.0 to 679.2 mbsf (2148.6–2432.8 mbrf), recovering 165.96 m of core (58%).

During operations at Site 1178, the current generally averaged between 2.5 and 3.5 nmi/hr. However, on several occasions it was believed that the current was over 5 nmi/hr. The bridge

speed log indicated 4.8 nmi/hr during those times, and 100 turns on both screws were required to maintain station. Severe vibrations in the drill string were observed. The vibrations were transmitted up to the top drive and associated traveling equipment. The electrical supervisor reported that the hydrophones were vibrating severely within their wells. The aft side of the upper guide horn was too hot to touch with a bare hand because of the drill string rubbing against it.

Even though the ship was able to maintain position during the peak current times, we thought that the safe operational limits had been reached for two reasons. First, the automatic station keeping (ASK) system was already operating at its maximum output available from the main screws. Any increase in the 10–12 nmi/hr head winds would have exceeded the ASK systems ability to maintain station. Second, and perhaps more importantly, the severe vibration in the drill string and traveling equipment was of great concern. Fatiguing of drill-pipe connections as well as possible damage to compensator rods and seals was a distinct possibility. There were also concerns about any loose objects that might fall out of the derrick. Had the current increased above the perceived 5 nmi/hr, operations would have had to be shut down.

At 1515 hr on 12 July, three thrusters (T-2, T-4, and T-5) automatically tripped off line. Fortunately the ASK system was able to compensate for the lost thrusters and maintain ship position. With a 3+ nmi/hr current running at the time, the decision was made to raise the bit from the current total depth of the hole (419.3 mbsf) to 32.7 mbsf until the ASK system problem could be resolved. The problem was traced to a faulty transformer in the forward thyrig room. This transformer supplied power to the thruster controller cards and was giving a faulty signal. The transformer was bypassed, and the ASK system performance immediately returned to normal. Operations were resumed after losing 4.5 hr.

Coring was stopped in Hole 1178B when the allotted coring time for Leg 190 expired at 0600 hr on 15 July. The hole was filled with heavy mud and the bit was tripped out. The bit cleared the seafloor at 0845 hr, and the positioning beacon was released and recovered at 1045 hr. The bit cleared the rig floor at 1250 hr on 15 July, officially ending Hole 1178B and operations at Site 1178.

Transit from Site 1178 to Yokohama

The ship began the transit to Yokohama at 1400 hr on 15 July. The first line was ashore at 1600 hr on 16 July at Daikoku Wharf, Yokohama, Japan, officially ending Leg 190.